EVENT-BY-EVENT CORRELATIONS BETWEEN LAMBDA HYPERON AND THE CHIRAL MAGNETIC EFFECT OBSERVABLES IN AU+AU COLLISIONS AT 27 GEV FROM STAR

by

Yicheng Feng

A Dissertation

Submitted to the Faculty of Purdue University

In Partial Fulfillment of the Requirements for the degree of

Doctor of Philosophy

Department of Physics and Astronomy

West Lafayette, Indiana

May 2022

THE PURDUE UNIVERSITY GRADUATE SCHOOL
STATEMENT OF COMMITTEE APPROVAL

Dr. Fuqiang Wang, Chair

Department of Physics and Astronomy

Dr. Wei Xie

Department of Physics and Astronomy

Dr. Denes Molnar

Department of Physics and Astronomy

Dr. Martin Kruczenski

Department of Physics and Astronomy

Approved by:

Dr. Gabor Csathy

ACKNOWLEDGMENTS

In my PhD project, I have received many helps from others, without which the accomplishment of my thesis could not be possible.

First of all, I would like to thank my family. They are very supportive to my academic pursuit. It is really a challenge for me to be so far away from home for so many years. However, every time I have a video call with my family, I would feel like that I had never been one step away from them. Emotionally, it is just like one kind of quantum coupling, across the spacetime. I think their kind care and support is the main reason why I could maintain my mental health.

Then, I wish to express my gratitude to my advisor, Prof. Fuqiang Wang. He guided me to this field, high energy nuclear physics (HENP), which is one of the frontiers of physcis research. He provided me many encouragements and oppotunities to gain improvements. I have learned from him, not only physics, but also how to be a real physicist. The physicists need to keep honest all the time, and respect the reality (experimental results) even if they are not satisfactory at all. The physicists should have the courage to explore the difficult topics/methods, even if there is always no guaranteed payback. I believe that those great qualities are always inspiring and beneficial to my academic pursuit.

I would like to show my appreciations to all my thesis committee members, Prof. Fuqiang Wang, Prof. Wei Xie, Prof. Denes Molnar, and Prof. Martin Kruczenski. Prof. Xie is the organizer of our weekly group meeting, where we can present our results, get comments, and have discussions with each others. From the group meetings, I have got many valuable comments from him and other group members. Prof. Molnar taught me the course, computational physics, where I learned algorithms to model the physical systems and coding techniques for data analysis. The computational view towards physics is very useful in my daily research work. Prof. Kruczenski taught me the courses, quantum physics and quantum field theory, where I learned the beautiful physics theories as the foundstone of my research field. The theoretical view towards physics serves as the torchlight guiding our analysis to sail on the unknown sea of HENP.

Besides my advisory committee, I want to also thank all my colleagues in our group, Jie Zhao, Haojie Xu, Hanlin Li, Rui Xiao, An Gu, Liang Zhang, Liang He, Milan Stojanovic, Terrence Edmonds, Hao Qiu, Jian Sun, Charles Robertson, Soumik Chandra, *et al.* I got a lot of helps and trainings from Jie Zhao, the former postdoc in our group. His great skill and high-quality analysis are very impressive to me. I really appreciate his patience and generosity in sharing his academic experience with me. I learned to drive from Haojie Xu, the former visit scholar in our group. Thanks to him, I finally got my driver's license...Too many memories overwhelm me at this moment. I cannot go through every piece here, but all of those memories shared with them are the precious gifts to my life.

Finally, I would like to thank the STAR Collaboration for the great STAR detector and the great community of HENP. The dataset used in this analysis is collected by the STAR detector. For this study, I want to show my especial appreciation to Prof. Evan Finch and his group. Their interesting theory paper is the motivation of this study, and their valuable comments really contribute to this analysis. We had many helpful discussions in the FCV meetings and the CME-focus meetings in STAR.

TABLE OF CONTENTS

LIST OF TABLES

LIST OF FIGURES

LIST OF SYMBOLS

$\sqrt{s_{\rm NN}}$	nucleon-nucleon center-of-mass energy
ϕ	azimuthal angle
η	pseudorapidity
p_T	transverse momentum
$\Psi_{\rm RP}$	azimuthal angle of reaction plane
Ψ_n	$n^{\rm th}$-order event plane (in this study Ψ_1 and Ψ_2 are used)
Λ	Λ hyperon
$\bar{\Lambda}$	anti-Λ hyperon (anti-particle of Λ)
$\vec{p}^{*}_{p}$	decay daughter proton momentum in the parent Λ rest frame
$\vec{p}^{*}_{\bar{p}}$	decay daughter anti-proton momentum in the parent $\bar{\Lambda}$ rest frame
ϕ^{*}_{p}	azimuthal angle of $\vec{p}^{*}_{p}$
$\phi^{*}_{\bar{p}}$	azimuthal angle of $\vec{p}^{*}_{\bar{p}}$
P_{Λ}	global polarization of Λ
$P_{\bar{\Lambda}}$	global polarization of $\bar{\Lambda}$
ΔP	$\Delta P = P_{\Lambda} - P_{\bar{\Lambda}}$
N_L	number of left-handed particles (particles could be Λ, $\bar{\Lambda}$ or their sum)
N_R	number of right-handed particles (particles could be Λ, $\bar{\Lambda}$ or their sum)
ΔN	difference in the numbers of left/right-handed particles, $\Delta N = N_L - N_R$
Δn	normalized ΔN, $\Delta n = \Delta N / \langle N_L + N_R \rangle$
$X^{\rm obs}$	observed quantity, X can be N, ΔN, Δn, ...
a_1^+	CME coefficient of positive charges $\langle \sin(\phi^+ - \Psi_{\rm RP}) \rangle$
a_1^-	CME coefficient of negative charges $\langle \sin(\phi^- - \Psi_{\rm RP}) \rangle$
Δa_1	$\Delta a_1 = a_1^+ - a_1^-$
$\gamma_{\rm OS}$	azimuthal correlator of opposite-sign (OS) charge pairs $\gamma_{\rm OS} = \langle \cos(\phi^{\pm}_{\alpha} + \phi^{\mp}_{\beta} - 2\Psi_{\rm RP}) \rangle$
$\gamma_{\rm SS}$	azimuthal correlator of same-sign (SS) charge pairs $\gamma_{\rm SS} = \langle \cos(\phi^{\pm}_{\alpha} + \phi^{\pm}_{\beta} - 2\Psi_{\rm RP}) \rangle$
$\Delta\gamma$	$\Delta\gamma = \gamma_{\rm OS} - \gamma_{\rm SS}$

v_2 the "true" elliptical flow, ideally without nonflow contamination

v_2^* the inclusive elliptical flow measurement $v_2^{*2} \equiv \langle \cos 2(\phi_\alpha - \phi_\beta) \rangle$ (* means nonflow included)

$C_{3,\mathrm{OS}}$ $C_{3,\mathrm{OS}} = \langle \cos(\phi_\alpha^\pm + \phi_\beta^\mp - 2\phi_c) \rangle$

$C_{3,\mathrm{SS}}$ $C_{3,\mathrm{SS}} = \langle \cos(\phi_\alpha^\pm + \phi_\beta^\pm - 2\phi_c) \rangle$

C_3 $C_3 = C_{3,\mathrm{OS}} - C_{3,\mathrm{SS}}$, it contains nonflow, and can give the $\Delta\gamma$ w.r.t. event plane $\Delta\gamma^* = C_3/v_2^*$ (* means nonflow included)

ϵ_{nf} $\epsilon_{\mathrm{nf}} = U/v_2^2$ nonflow component in v_2^2 (square of the true elliptic flow)

ϵ_2 2-particle nonflow coupled with elliptical flow v_2, like resonance decays

ϵ_3 3-particle nonflow like jet correlations

ABBREVIATIONS

QCD	Quantum Chromodynamics
QGP	Quark Gluon Plasma
CME	Chiral Magnetic Effect
RHIC	Relativistic Heavy Ion Collider
LHC	Large Hadron Collider
STAR	Solenoid Tracker At RHIC
TPC	Time Projection Chamber
TOF	Time of Flight detector
VPD	Vertex Position Detecotr
ZDC	Zero Degree Calorimeter
EPD	Event Plane Detector
QA	Quality Assurance
Cov	covariance
PV	Primary Vertex where the two nuclei collide
RP	Reaction Plane
EP	Event Plane
PP	Participant Plane
SP	Spectator Plane
POI	particle of interest
RefMult	reference multiplicity (measured with $\|\eta\| < 0.5$)
TofMatch	number of particles with TPC and TOF matched
dca	distance of closest approach
gDca	distance of the closest approach to PV for global tracks
nHitsFit	the number of hits used to fit a track
nHitsMax	a soft upper limit for nHitsFit
dl	decay length

ABSTRACT

Spin-orbit interactions cause a global polarization (P) of Λ ($\bar{\Lambda}$) with the vorticity (or total angular momentum) in the participant collision zone. The strong magnetic field mainly created by the spectator protons would split the Λ and $\bar{\Lambda}$ global polarization ($\Delta P = P_\Lambda - P_{\bar{\Lambda}} < 0$). Quantum chromodynamics (QCD) predicts topological charge fluctuation in vacuum, resulting in a chirality imbalance, or parity violation in a local domain. This would give rise to an imbalanced left- and right-handed Λ ($\bar{\Lambda}$), $\Delta n = \frac{N_{\rm L} - N_{\rm R}}{\langle N_{\rm L} + N_{\rm R} \rangle} \neq 0$, as well as a charge separation along the magnetic field, referred to as the chiral magnetic effect (CME). The latter can be characterized by the parity-even $\Delta\gamma$ and parity-odd Δa_1 observables. While measurements of the individual ΔP [1, 2], $\Delta\gamma$, and Δa_1 have not led to affirmative conclusions on the CME or the magnetic field, correlations among these observables may reveal new insights [3, 4]. We report exploratory measurements of event-by-event correlations between ΔP and $\Delta\gamma$, and between Δn and Δa_1, by the STAR experiment in Au+Au collisions at $\sqrt{s_{\rm NN}} = 27$ GeV. No correlations have been observed beyond statistical fluctuations. Future endeavor would be to extract an upper limit from the data as well as to apply the correlation analysis to other data samples.

1. INTRODUCTION

1.1 Standard Model of Particle Physics

Much of our present day knowledge about nature is encapsulated by the standard model of particle physics, which describes the electroweak and strong interactions with their corresponding elementary particles. The elementary particles are those that cannot be decomposed into other particles. Some of them are the building blocks of matter, and others are the propagators of the interactions.

For the components shown in Fig. 1.1 (anti-particles not listed) [5], Quantum Electrodynamics (QED), including the weak interaction, describes the leptons (e, μ, τ), neutrinos (ν_e, ν_μ, ν_τ), and gauge bosons (γ, Z, W). Quantum Chromodynamics (QCD) describes the gluons (g) and quarks (u, d, c, s, t, b as 6 flavors), where the u, d light quarks make the

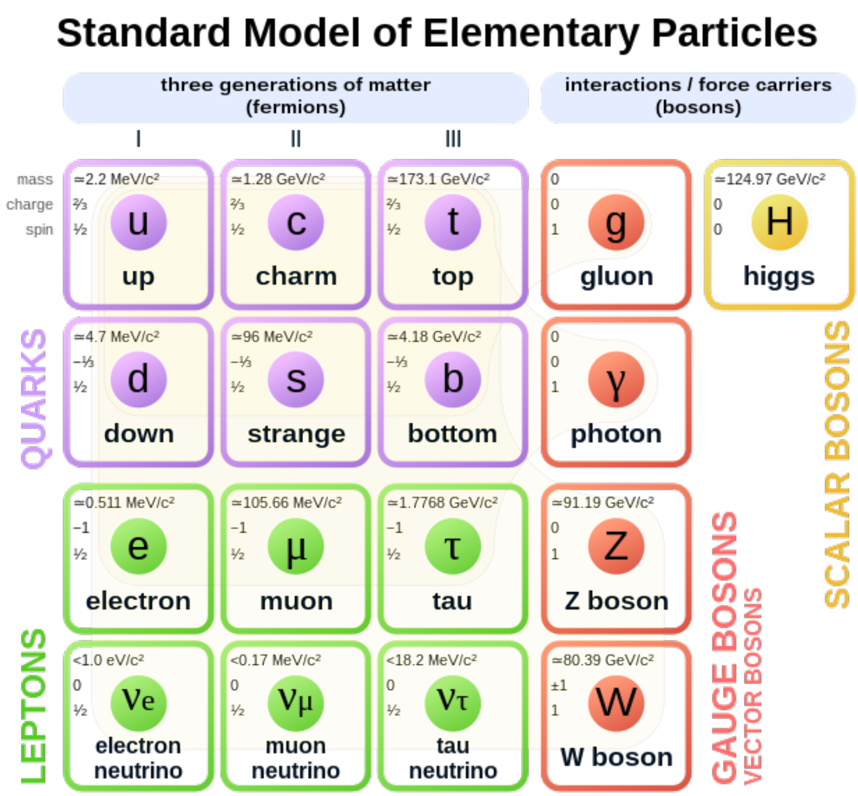

Figure 1.1. Standard model of elementary particles (from Wikipedia [5]).

nucleons, s is called strangeness quark, and other quarks are called heavy flavors. The latest experimental update to the standard model is the Higgs scalar boson (H) [6, 7].

1.2 Quantum Chromodynamics (QCD) and Vacuum Fluctuations

A main component of the standard model of particle physics is the quantum chromodynamics (QCD), a theory describing the strong interactions among quarks mediated by gluons. This theory has the symmetry group $SU(3)$ [8] (3×3 unitary matrix with determinant constrained to $+1$), where the 3 dimensions correspond to 3 "colors"–red, blue, green for quarks or anti-red, anti-blue, anti-green for anit-quarks. The $SU(3)$ group has 8 non-trivial ($\neq$ identity I) elements, which can be understood as follows: $3 \times 3 = 9$ complex numbers have $9 \times 2 = 18$ degrees of freedom (real part + imaginary part), while unitary provides 9 constraints and det $= 1$ provides 1 constraint, so totally $18 - 9 - 1 = 8$ degrees of freedom left. In other words, any irreducible isomorphic representation of $SU(3)$ (e.g., Gell-Mann matrices) has the size 8 (or order 9 including identity element). Each of the 8 element corresponds to one of the 8 "gluon color types". As confirmed by all experiments, QCD has a property called color confinement [9]–any stable strongly interacting particles must be "colorless", though there is no analytic proof to date. Here, "colorless" means that one color coupled with its anti-color (meson), or 3 different (anti-)colors grouped together (baryon), or the combinations of those two cases (exotic hadrons).

Unlike the electroweak interaction or gravity, the strong interaction becomes weaker as the length scale decreases. This phenomenon is called asymptotic freedom [10, 11], a unique property of QCD.

The topological charge is defined by the gluon field and could fluctuate in vacuum, which effectively makes the quarks have a chirality preference in a local domain (Fig. 1.2 left panel). This chiral anomaly [12, 13, 14] is another property of QCD. Heavy ion collisions were proposed to look for this basic physics of QCD.

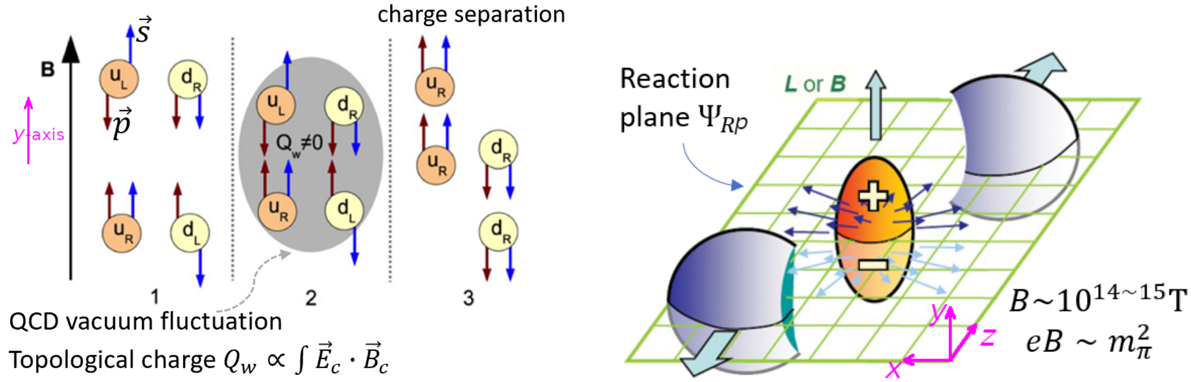

Figure 1.2. Schematic diagrams illustrating the CME physics. The left diagram is taken from Ref. [21], and the right diagram is taken from Ref. [22].

1.3 Heavy Ion Collisions

Heavy ions mean the nuclei of heavy elements (e.g., Au, Pb). Large scientific facilities like RHIC (Relativisitc Heavy Ion Collider) [15, 16, 17, 18], and the LHC (Large Hadron Collider) [19, 20] can accelerate the heavy ions close to the speed of light and then make them collide with each other (e.g., Au+Au with energy up to 200 GeV per nucleon-nucleon pair at RHIC, Pb+Pb with energy up to 5.5 TeV per nucleon-nucleon pair at the LHC).

In those heavy ion collisions, due to finite impact parameter, only a fraction of nucleons participate in the collision, called participants, while the others are out of the collision zone, called spectators. The spectator protons can create, at the first instant of the collision, a very strong magnetic field in the collision zone (Fig. 1.2 right panel). Therefore, the spin of particles (quarks) would be locked either parallel or anti-parallel to the magnetic field direction depending on their charges.

1.4 Chiral Magnetic Effect (CME)

The QCD topological charge fluctuations cause chirality preference in a local domain. The strong magnetic field created by the spectator protons in heavy ion collisons lock the spins of positive and negative charge quarks to have opposite directions. Thus, the positive and negative charge quarks of the same handedness would have opposite momentum directions along that magnetic field. This charge separation phenomenon is called the Chiral Magnetic

Effect (CME) [21, 22]. Many observables are proposed to measure the CME, like Δa_1 [21] (parity-odd)

$$\begin{aligned} a_1^+ =& \langle \sin(\phi^+ - \Psi_{\mathrm{RP}}) \rangle, \\ a_1^- =& \langle \sin(\phi^- - \Psi_{\mathrm{RP}}) \rangle, \\ \Delta a_1 =& a_1^+ - a_1^-, \end{aligned} \tag{1.1}$$

and $\Delta\gamma$ [23] (parity-even)

$$\begin{aligned} \gamma_{\mathrm{OS}} =& \langle \cos(\phi_\alpha^\pm + \phi_\beta^\mp - 2\Psi_{\mathrm{RP}}) \rangle, \\ \gamma_{\mathrm{SS}} =& \langle \cos(\phi_\alpha^\pm + \phi_\beta^\pm - 2\Psi_{\mathrm{RP}}) \rangle, \\ \Delta\gamma =& \gamma_{\mathrm{OS}} - \gamma_{\mathrm{SS}}. \end{aligned} \tag{1.2}$$

Here, ϕ means the azimuthal angle of particles; the superscripts $+$, $-$ indicate the charge sign; the subscripts α, β mean two difference particles in the same event, and OS, SS stand for “opposite-sign” and ”same-sign” pairs. The reaction plane (RP) is spanned by the beam direction and the impact parameter, whose azimuthal angle is denote as Ψ_{RP}.

For now, no affirmative conclusion on the CME has been reached by the measurements of individual parity-even observable $\Delta\gamma$ (RHIC: Au+Au [24, 25, 26, 27] and d+Au [28]; the LHC: Pb+Pb [29, 30, 31, 32, 33, 34] and p+Pb [31, 32]), mainly because of the background contaminations coupled with elliptical flow [23, 35, 36, 37, 38, 39, 40]. Many methods have been proposed to reduce or remove the backgrounds [30, 32, 33, 41, 42, 43, 44], with limited success. As for the parity-odd observable Δa_1, it vanishes in event average because of the random fluctuations of topological charges from event to event.

1.5 Λ Hyperon Properties

The Λ hyperon is neutral and contains 3 quarks u, d, s. Its anti-particle $\bar{\Lambda}$ contains $\bar{u}$, $\bar{d}$, $\bar{s}$. The main strong decay channels of Λ ($\bar{\Lambda}$) are $\Lambda \to p\pi^-$ ($\bar{\Lambda} \to \bar{p}\pi^+$) with 63.9% branching ratio and $\Lambda \to n\pi^0$ ($\bar{\Lambda} \to n\pi^0$) with 35.8% [45]. We are interested in the first channel, because the second channel has neutral decay daughters, which are not detected in most of the detectors.

Unlike charged hadrons whose handedness measurement has to rely on magnetic field induced charge separation, the Λ ($\bar{\Lambda}$) handedness can actually be measured by their decay topology. As mentioned before, chirality preference of quarks in the collision zone can be inherited by Λ ($\bar{\Lambda}$) hyperons. This kind of fluctuation may be characterized in each event, if we measure the normalized number difference (Δn) between left-handed (subscript L) and right-handed (subscript R) Λ (or $\bar{\Lambda}$):

$$\Delta n = \frac{N_{\rm L} - N_{\rm R}}{\langle N_{\rm L} + N_{\rm R} \rangle} \neq 0\,, \tag{1.3}$$

where N_L and N_R are the numbers of left and right-handed particles (Λ or $\bar{\Lambda}$ or their sum) in each event, and the denominator is the average among events. Similar to Δa_1, Δn is a parity-odd observable, whose event average is also by definition 0 if measured with ideal efficiency. Although parity-odd observables vanish trivially in their event averages, Δa_1 and Δn both come from the same chirality anomaly in each event, so the event-by-event correlation between Δa_1 and Δn could be non-trivial [4].

The magnetic field can have another consequence, namely difference in the Λ and $\bar{\Lambda}$ polarization. The participants contribute to the nonzero total angular momentum. The global angular momentum and magnetic field should roughly align with each other. The vorticity can cause global polarization preference with respect to the impact parameter [1, 2], equally on Λ and $\bar{\Lambda}$. Meanwhile, the magnetic field can enhance the polarization of $\bar{\Lambda}$ and reduce that of Λ. As a result, it was proposed to probe the magnetic field by measuring the polarization difference between Λ (P_Λ) and $\bar{\Lambda}$ ($P_{\bar{\Lambda}}$), ($\Delta P = P_\Lambda - P_{\bar{\Lambda}}$), which, similar to $\Delta\gamma$, is also a parity-even observable. However, statistical precision does not allow a firm conclusion for the current measurements of individual ΔP so far [2]. In order to probe the magnetic field, one may study correlation between polarization difference ΔP and $\Delta\gamma$, which are both related to magnetic field.

1.6 Event-by-Event Correlations

To take one step further in search for the CME, we correlate the observables (Δa_1 vs. Δn, ΔP vs. $\Delta\gamma$) event by event to gain possible new insights [3, 4]. The flow chart below (Fig. 1.3) delineates the physics sources of those quantities in the same event. If there is any signal, Δa_1 and Δn are expected to be negatively correlated, and $\Delta\gamma$ and ΔP are expected to be also negatively correlated. This analysis uses covariance to quantify the correlations, where the uncorrelated backgrounds automatically drop.

In this study, We report exploratory measurements of event-by-event covariance between Δn and Δa_1 and between ΔP and $\Delta\gamma$ by the STAR experiment in Au+Au collisions at 27 GeV.

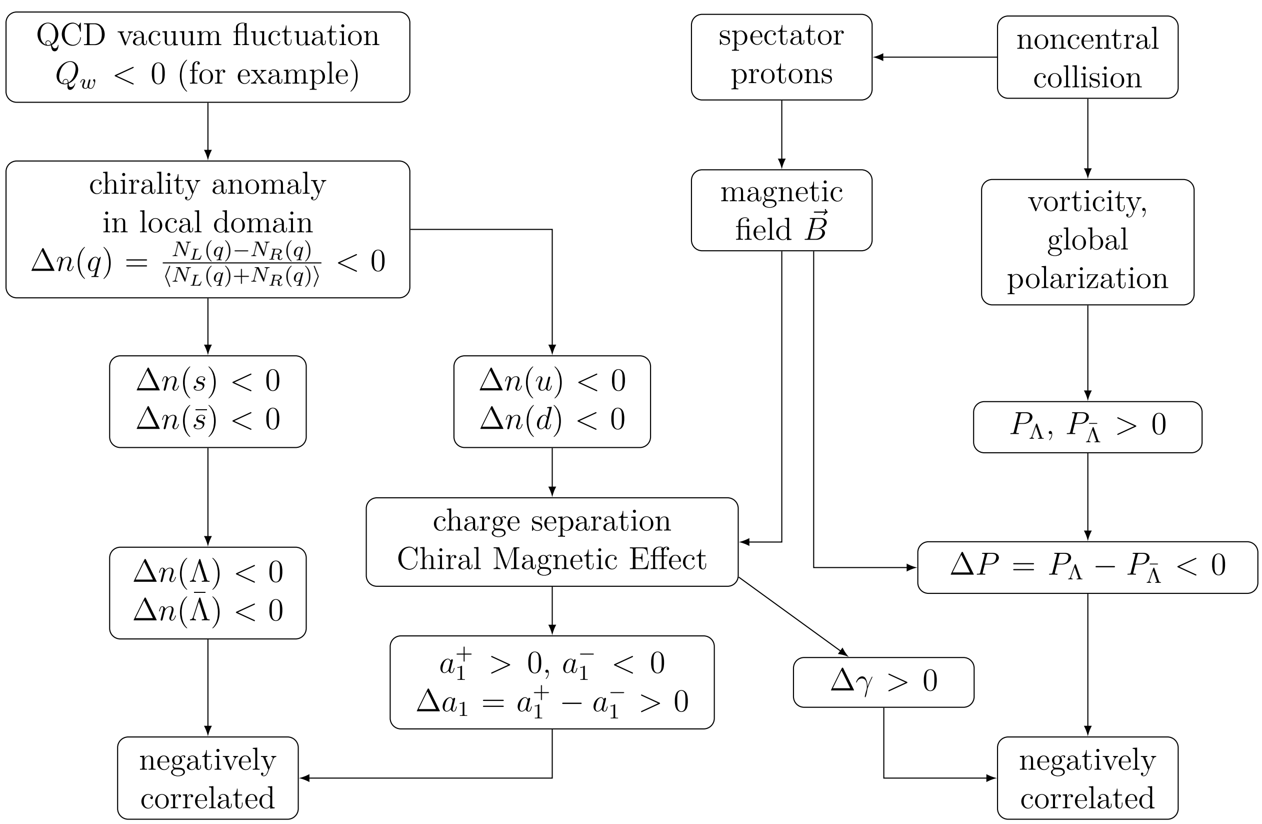

Figure 1.3. The physics sources of the observables Δn, Δa_1, $\Delta\gamma$, ΔP, and how those observables are correlated.

2. EXPERIMENTAL APPARATUS

The Relativistic Heavy Ion Collider (RHIC) [46, 47, 48] is located at the Brookhaven National Laboratory (BNL), which can accelerate protons up to 99.999296% of the speed of light and gold nuclei up to 99.995598% of the speed of light. In a more commonly used language, the energy of the proton pair in $p + p$ collisions is up to 500 GeV in the center of mass frame of that pair, and the energy per nucleon-nucleon pair in Au + Au collisions is up to 200 GeV in the center of mass frame of that pair, where the energy per nucleon-nucleon pair is denoted by $\sqrt{s_{\rm NN}}$ in the center of mass frame. The most of the collision systems in RHIC are symmetric, whose center of mass frame therefore coincides with the lab frame.

The detail information of RHIC is well recorded in the references [47, 46], and here I just give a very brief review. The main body of RHIC is a circular tunnel of $\sim$ 3.8 km in circumference, inside which there are two quasi-circular concentric accelerator/storage rings–clockwise "Blue Ring" and counter-clockwise "Yellow Ring". The particle beams can

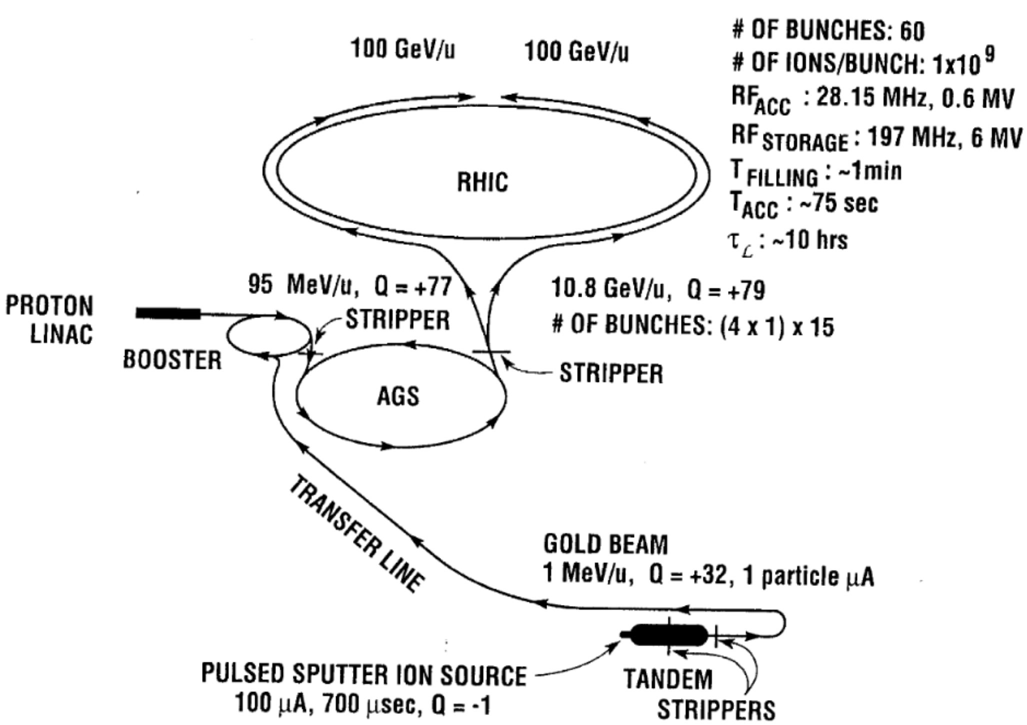

Figure 2.1. The RHIC accelerator complex [46].

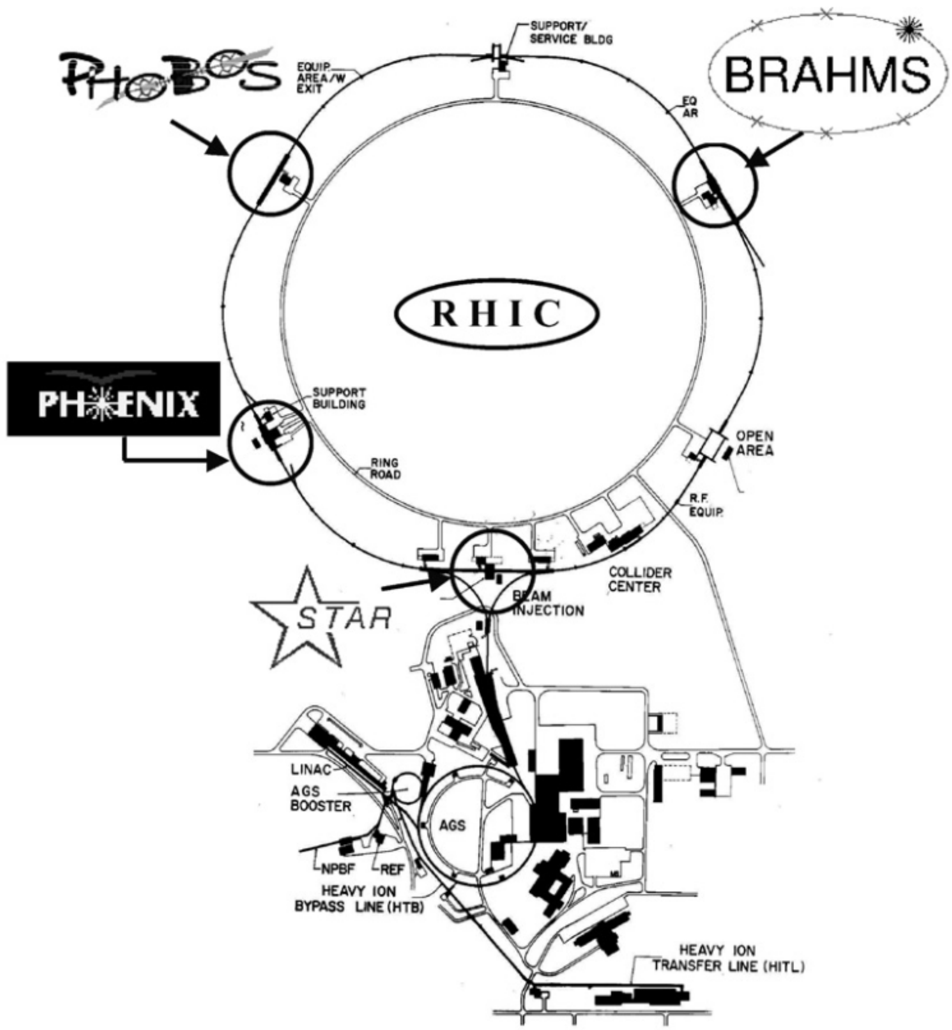

Figure 2.2. RHIC detectors [46].

be controlled inside those rings by many dipole, quadrupole, and sextupole superconductive magnets. The particle accelerating and electron stripping take several steps (Fig. 2.1). The heavy ions are prepared by Tandem Van de Graaffs with residual electrons. After a charge selection, they are transferred to Booster Synchrotron and accelerated. Then, they are injected into the Alternating Gradient Synchrotron (AGS) and accelerated. Finally, they are injected from AGS to RHIC and further accelerated in RHIC. During the exit of each node above, the heavy ions have some of their electrons stripped. When injected into RHIC, there are only nuclei left. For protons, there is a Linac (linear accelerator) directly injecting them into the Booster Synchrotron.

At the beginning (about 20 years ago), there were four detectors on RHIC (Fig. 2.2): STAR (the Soleniod Tracker At RHIC) [15], PHENIX (the Pioneering High Energy Nuclear Interaction eXperiment) [16], BRAHMS (Broad RAnge Hadron Magnetic Spectrometers) [17], and PHOBOS [18]. Nowadays (2022), STAR is the only active detector on RHIC, and this study is based on the data from the STAR detector. In the full name of STAR, Solenoid refers to the cylindrical geometry of the STAR magnet [49]. In the following sections of this chapter, some components of STAR will be introduced, especially those used in this analysis.

2.1 Time Projection Chamber (TPC)

The detailed information of the Time Projection Chamber (TPC) of STAR can be found in the references [50, 51]. Briefly speaking, TPC is a cylinder surrounding the beam pipe, whose outer diameter is 4 m, inner diameter 1 m, and length 4.2 m (Fig. 2.3, 2.4).

TPC can measure the "hit" positions of charged particles, which are used to reconstruct their tracks (trajectories, see Fig. 2.3). When a charged particle passes through the volumn of TPC, it ionizes the P10 gas (10% methane, 90% argon), with which TPC is filled. The ionization electrons drift towards the endcaps of the TPC under the influence of the electric field along the cylindrical axis of the TPC, created by high voltage applied to the Central

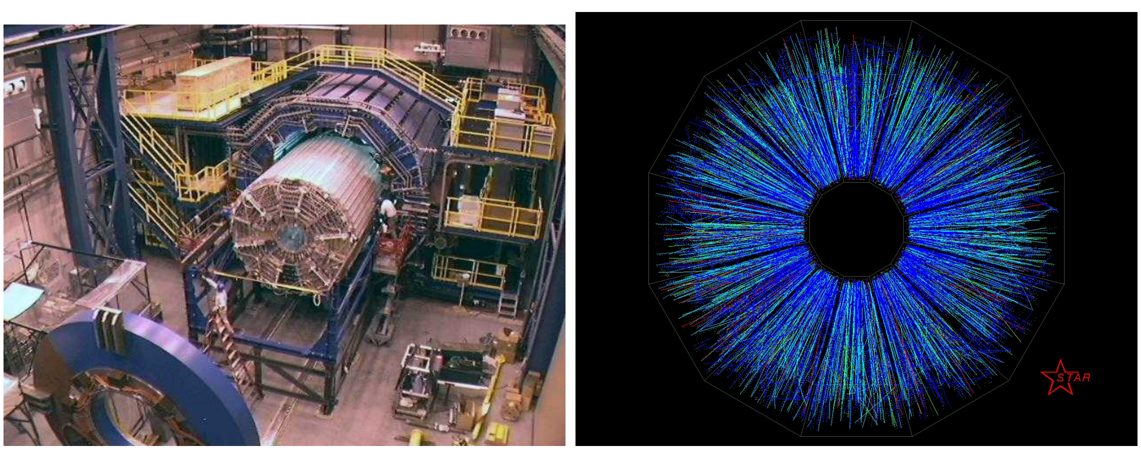

Figure 2.3. The insertion of STAR TPC (left). The STAR Event No. 12 - STAR Burst (right). The edges show the shape of TPC sectors on one side. (https://www.star.bnl.gov/public/tpc/tpc.html)

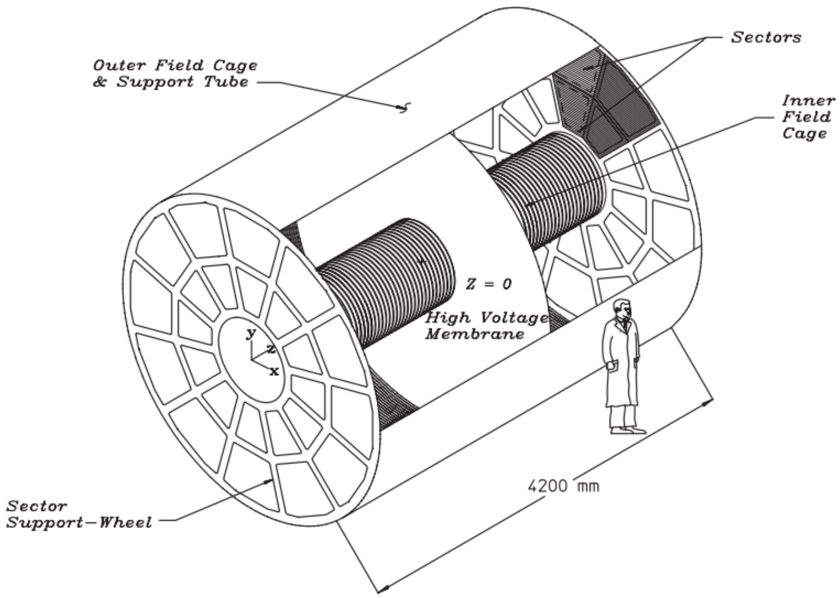

Figure 2.4. The STAR TPC schematic drawing [51].

Membrane (CM). Near the high-voltage anode wires as the TPC endcaps, the drifting electrons avalanche, and the signal is therefore amplified. The induced positive charges give signal to the readout pads adjacent to the wires. In this way, the x-y position of the particle can be measured. Meanwhile, the time information of the readout pad, multiplied with the known drift velocity of the electrons, gives the z position measurement of that particle.

The measured trajectories from TPC can provide some further information. Since there is a magnetic field (~ 0.5 T) along the z direction, the charge particles are bended. The bending direction can tell its charge sign. The radius of curvature of each point on that track can tell the momentum of that charged particle at that point.

Due to the interaction with the gas in TPC, the charged particle loses energy during its traveling inside TPC, which can be estimated by the momentum change along the track. Thus, the energy loss per unit length $\mathrm{d}E/\mathrm{d}x$ can be used to identify the particle type (Fig. 5.2).

There was an upgrade to inner TPC [52], but this dataset was taken before that, so this dataset still uses the old TPC.

2.2 Event Plane Detector (EPD)

Event Plane Detector (EPD) is a newly installed detector at STAR in 2018, whose details are available in the reference [53]. The dataset analyzed in this study uses EPD to measure the event planes.

For symmetric systems, EPD can cover the range $0.7° < \theta < 13.5°$ or $2.14 < |\eta| < 5.09$ with $\eta \equiv -\ln[\tan(\theta/2)]$. EPD has two wheels, one on each side of STAR. Each wheel has 12 "supersectors". Each supersector (yellow color in Fig. 2.5) covers 30° azimuth and has 31 tiles. Each tiles has one optical fiber transporting its light signal to a silicon photomultiplier (SiPM) out of the wheel. The 31 optical fibers of one supersector are bundled and placed along the angle bisector as shown in Fig. 2.5.

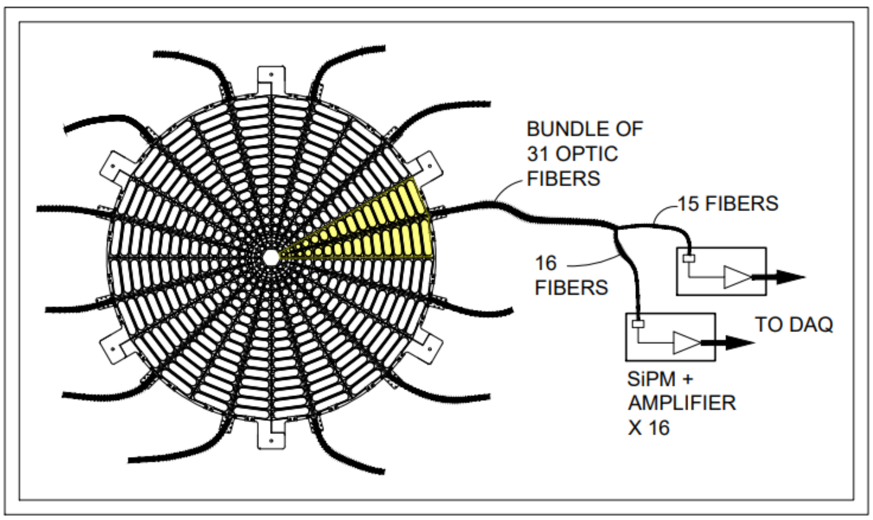

Figure 2.5. A sketch of the EPD system. One of two EPD wheels is shown. The 31 tiles from each of 12 supersectors are connected via optical fiber bundles to silicon photomultipliers and amplification electronics. [53]

2.3 Vertex Position Detector (VPD) and Time of Flight (TOF)

Both the initial Pseudo Vertex Position Detector (pVPD) and Time of Flight detector Patch (TOFp) in STAR are described in the reference [54]. This section provides a brief review to those detectors. For convenience, we just call them VPD and TOF in this study.

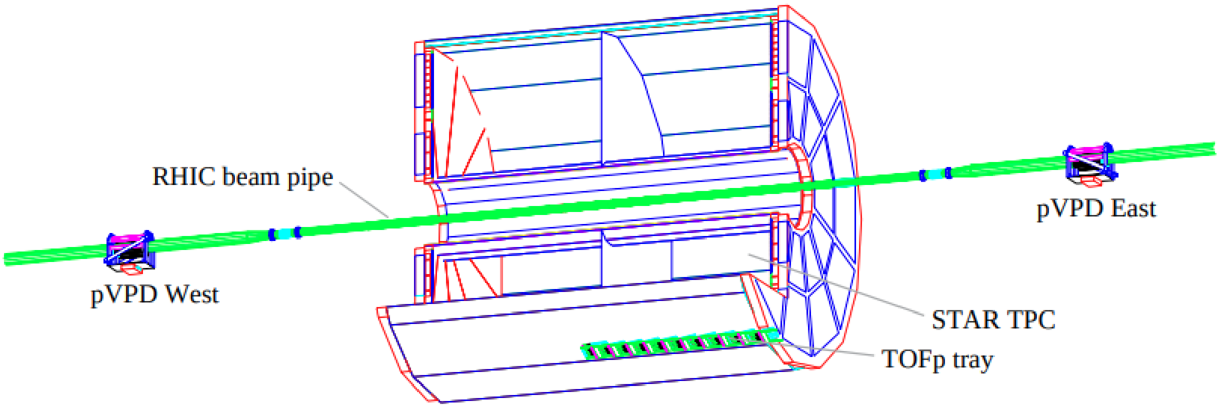

Figure 2.6. A scale drawing of the locations of pVPD and TOFp detectors in relation to the STAR TPC and the RHIC beam pipe. For clarity, the TPC is cut away, while the STAR magnet and other subsystems are not drawn. [54]

In RHIC, heavy ion collisions can produce a number of very forward, very high energy photons (bremsstrahlung) from the collision vertex. VPD has two identical assemblies (VPD West and VPD East) placed on each side of STAR with equal distance to the center. They can measure the photon pulses from the collision vertex in two opposite directions. For the same collision, the vertex deviation from the center can make the two assemblies see the pulse at slightly different times. One can therefore calculate the vertex position on the beam direction (z-direction) from that time difference. This timing information is used online to trigger on collisions within the central region of the TPC. The collision vertex can be reconstructed more accurately offline by the primordial tracks measured by the TPC.

The average time of VPD West and East measurements can be regarded as the "start" time of the tracks, while TOF measures the "stop" time for the arrival of tracks right outside the TPC. If a track is measured and matched by TPC and TOF, then both the track length (from TPC) and duration (from TOF - VPD) are known, which can therefore give the speed of this charged particle (β). Since TPC measures the momentum ($\vec{p}$), the particle mass (m) can therefore be calculated (Fig. 5.3).

3. DATASET AND REDUCTION

The dataset used in this analysis is the STAR Run18 Au+Au collisions at $\sqrt{s_{\mathrm{NN}}} = 27$ GeV, whose production tag is `P19ib` with `27GeV_production_2018`, stream name `st_physics` [55]. The Minibias (MB) triggered data is used. The trigger numbers are `610001`, `610011`, `610021`, `610031`, `610041`, `610051` [56]. The event level cuts (primary vertex, triggers, ...) are listed in this chapter. We conduct run-by-run quality assurance (QA) on this dataset to identify bad runs to be excluded from this analysis. As a quantitative estimate of how much two nuclei overlap in the collision, the centrality is defined by the STAR standard package `StRefMultCorr`, which also removes pileup events.

The raw dataset contains about 1.6 billion events in total. After all the event-level selections above, there are about 400 million events left.

3.1 Primary Vertex Selection

The primary vertex is the position of the collision, whose 3-dimensional position (V_x, V_y, V_z) can be reconstructed by TPC (Sec. 2.1). Its z-component is also measured by VPD (Sec. 2.3), denoted by V_z^{VPD}. The default cuts for z-position of the primary vertex are -70 cm $< V_z < 70$ cm. In addition, $|V_z^{\mathrm{VPD}} - V_z| < 3$ cm is required to ensure that the event is the triggered one.

Table 3.1. Primary vertex selection.

(cm)	default	systematics	
V_z	$[-70, 70]$	$[-60, 60]$	$[-80, 80]$
$V_r = \sqrt{V_x^2 + V_y^2}$	$[0, 2]$	–	–
$V_z^{\mathrm{VPD}} - V_z$	$[-3, 3]$	–	–

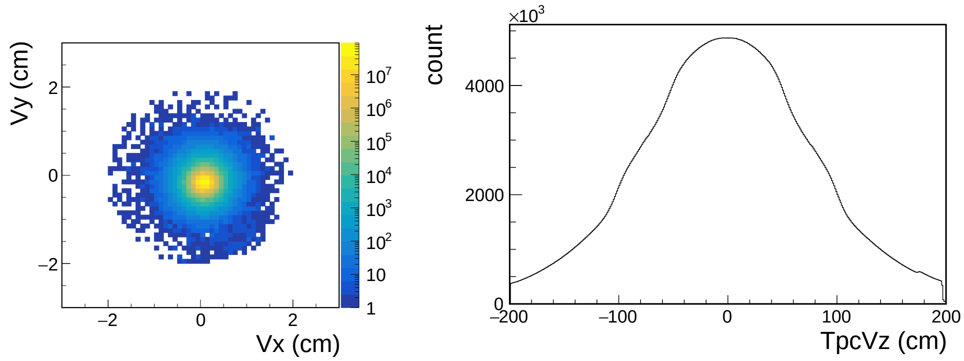

Figure 3.1. TPC vertex

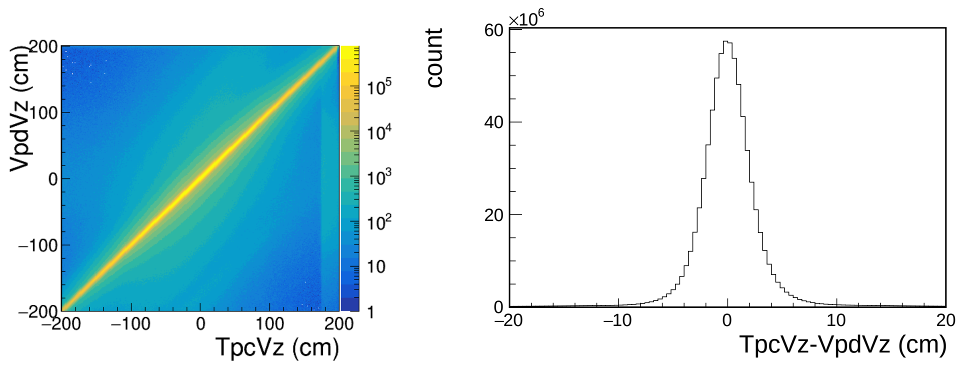

Figure 3.2. TPC VPD vertex comparison

3.2 Run-by-Run Quality Assurance (QA)

The STAR dataset is taken in a period of time with intervals, so, in another word, there are many "runs" of data taking. For this dataset, total 800 runs are used, where some of them may not be good to use in this analysis (bad runs). In run-by-run QA, we choose some variables and calculate their average values for each run. The bad runs would have average values largely deviating from the most of other runs beyond fluctuations, so they could be identified in this way. For plotting, we use run IDs instead of run numbers. The correspondence between them is shown by the list on RHIC-ATLAS Computing Facility (RACF): `/star/u/fengyich/gpfs01/datainfo/Run18AuAu27Full/run18List27.0.list` The first run number of this list corresponds to run ID = 0.

Table 3.2. Variables for run-by-run QA.

	name in code	description
1	RbyR_RefMult	reference multiplicity (from `StRefMultCorr`)
2	RbyR_RefMultWt	weighted RefMult (from `StRefMultCorr`)
3	RbyR_TofMatch	RefMult matched by TOF
4	RbyR_RawTpcPt0	$\langle p_T \rangle$
5	RbyR_RawTpcEta	$\langle \eta \rangle$
6	RbyR_RawTpcPhi	$\langle \phi \rangle$
7	RbyR_RawTpcQ1x	$\langle \cos(1\phi) \rangle$
8	RbyR_RawTpcQ1y	$\langle \sin(1\phi) \rangle$
9	RbyR_RawTpcQ2x	$\langle \cos(2\phi) \rangle$
10	RbyR_RawTpcQ2y	$\langle \sin(2\phi) \rangle$
11	RbyR_RawTpcNhits	$\langle$nHitsFit$\rangle$
12	RbyR_RawTpcGDca	$\langle$gDca$\rangle$
13	RbyR_TpcVz	Vertex position in z-axis $\langle V_z \rangle$

- This QA does not check the jumps, so there is no division of regions. All runs are considered together without time dependence.
- The mean value and error bands are calculated from the good runs weighted by $1/e^2$ (e is the statistical uncertainty for each run), and the bad runs are those beyond the $5\times$RMS band in any of the variables. Therefore, iterations are proceeded until no further bad runs are identified.
- The bad runs given by `StRefMultCorr` will also be removed, even if they are not completely covered by the list below.

The following pages show the run-by-run plots (Fig. 3.3–3.15), where the red and magenta markers show the bad runs. The magenta markers show the bad runs identified in the current observable, while the red markers are from other observables. It is possible that a bad run has already been identified by another observable, so this bad run would be marked by red, even if it can also be identified by the current observable.

From this QA, 116 bad runs are identified:

19131013 19131030 19131031 19131040 19131041 19131042 19131045 19131046 19131048 19131049 19131050 19131051 19131052 19132014 19132017 19132029 19132030 19132031 19132032 19132036 19132037 19132038 19132039 19132064 19132065 19132070 19132071

19132074 19132075 19132076 19132081 19132082 19133004 19133005 19133008 19133018
19133059 19133060 19133061 19134007 19134008 19134009 19134024 19134025 19134027
19134028 19134029 19134030 19134036 19134037 19134038 19134041 19134042 19134049
19134050 19135001 19135004 19135012 19135027 19135028 19135029 19135037 19135038
19135039 19135040 19135043 19136001 19136003 19136004 19136005 19136008 19136009
19136011 19136012 19136013 19136014 19136017 19136018 19136040 19136041 19136042
19136045 19136046 19136047 19137001 19137002 19137004 19137007 19137008 19137009
19137010 19137011 19137014 19137016 19137019 19137020 19137025 19137026 19137027
19137028 19137029 19137050 19137051 19137052 19141019 19158003 19158007 19158009
19158010 19158011 19158013 19158014 19158015 19158017 19158018 19158019

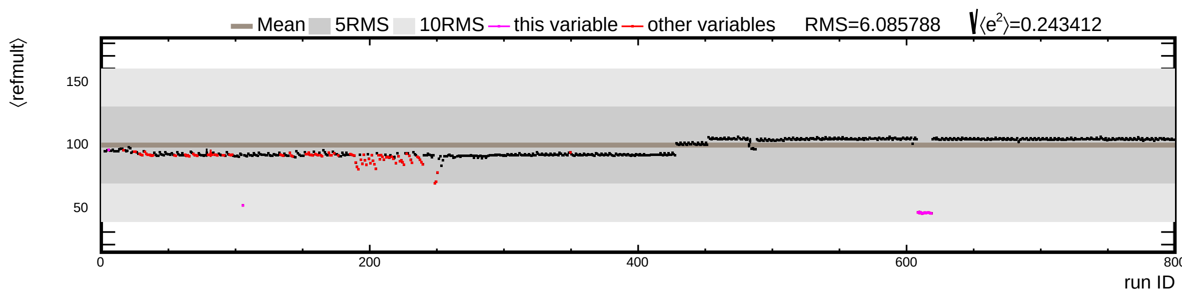

Figure 3.3. Run-by-run ⟨RefMult⟩

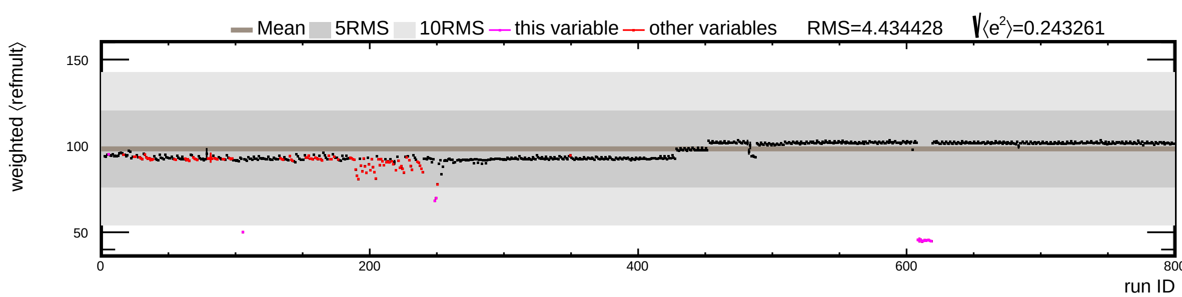

Figure 3.4. Run-by-run weighted ⟨RefMult⟩

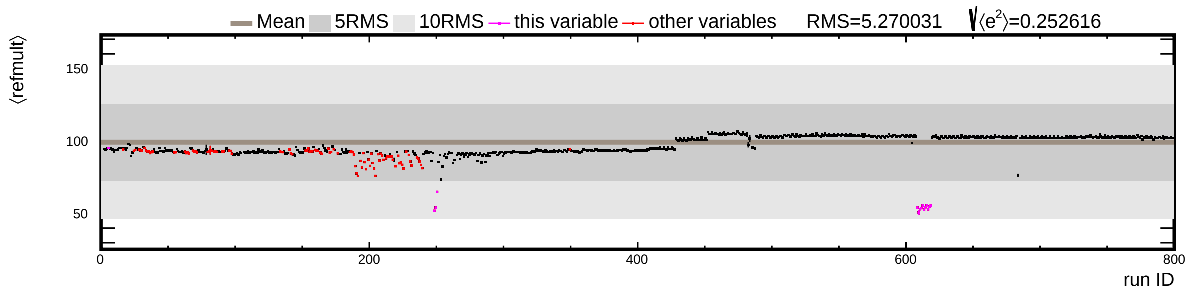

Figure 3.5. Run-by-run ⟨TofMatch⟩

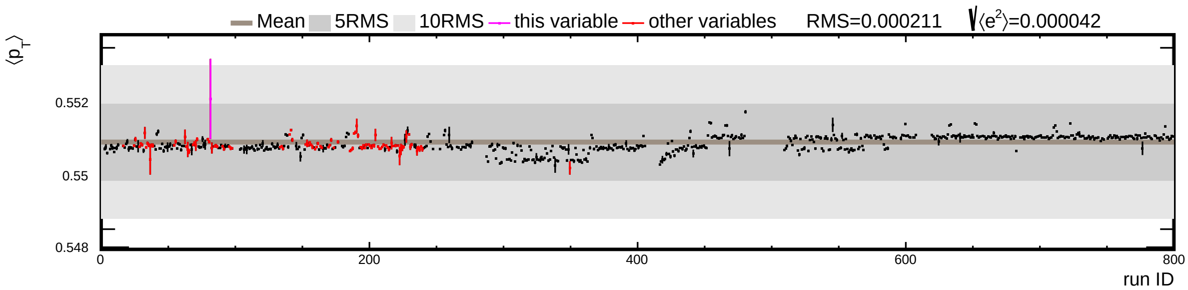

Figure 3.6. Run-by-run $\langle p_T \rangle$

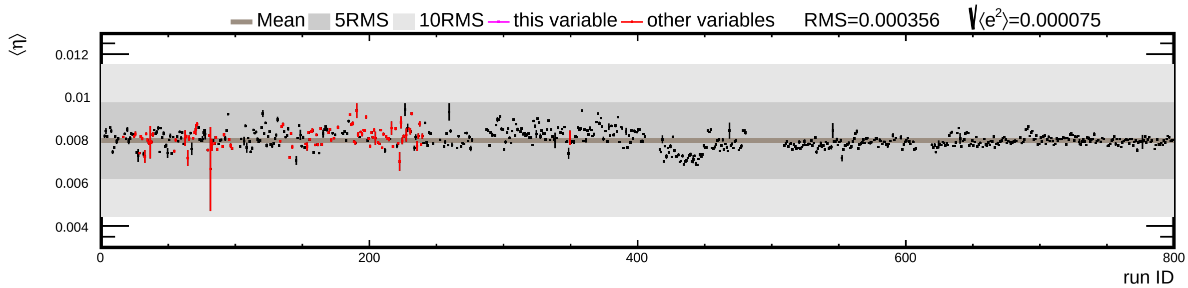

Figure 3.7. Run-by-run $\langle \eta \rangle$

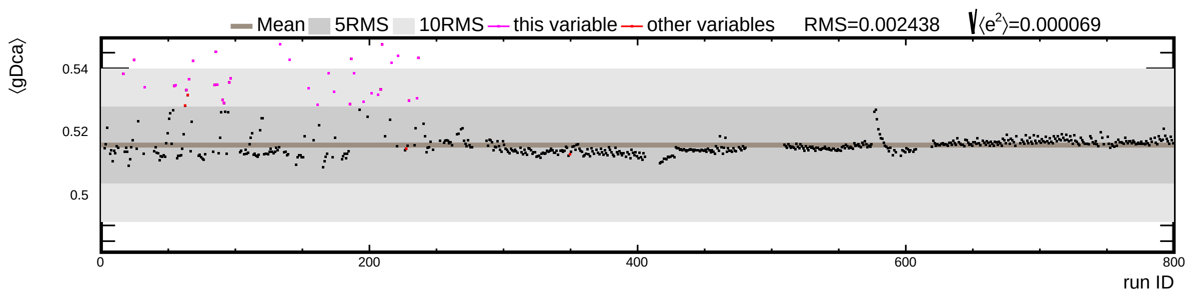

Figure 3.14. Run-by-run ⟨gDca⟩

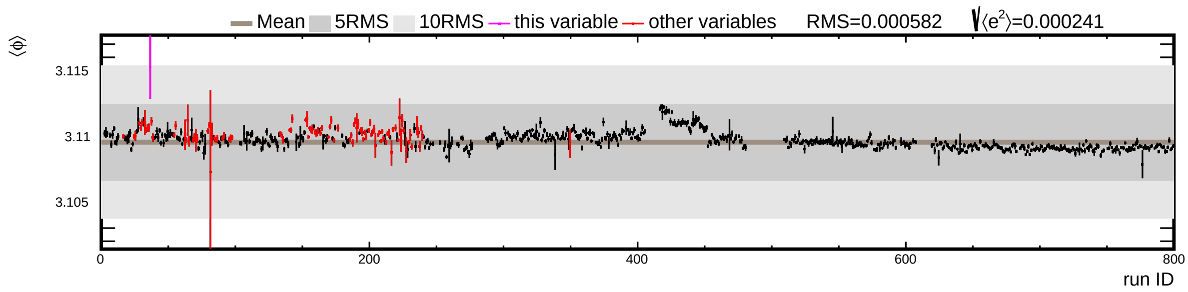

Figure 3.8. Run-by-run $\langle \phi \rangle$

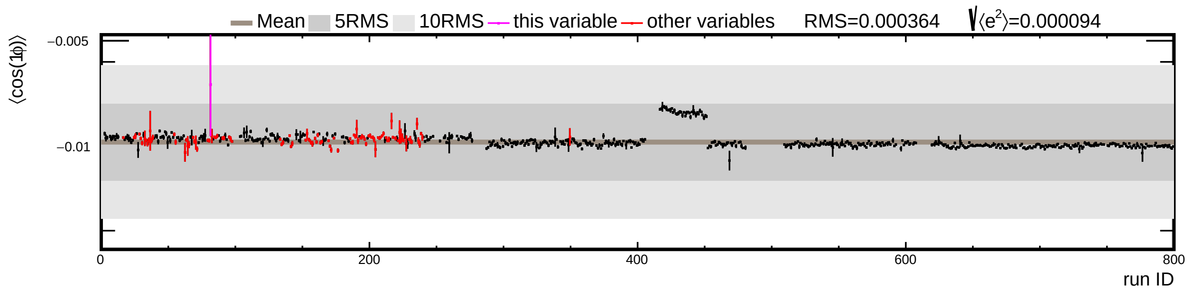

Figure 3.9. Run-by-run $\langle \cos 1\phi \rangle$

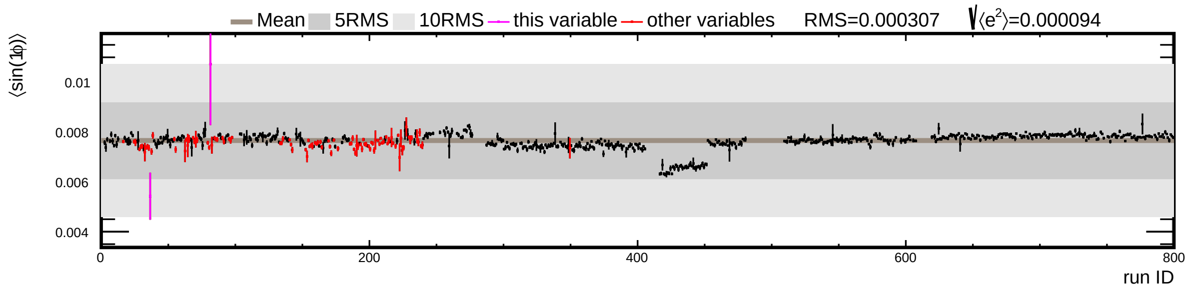

Figure 3.10. Run-by-run $\langle \sin 1\phi \rangle$

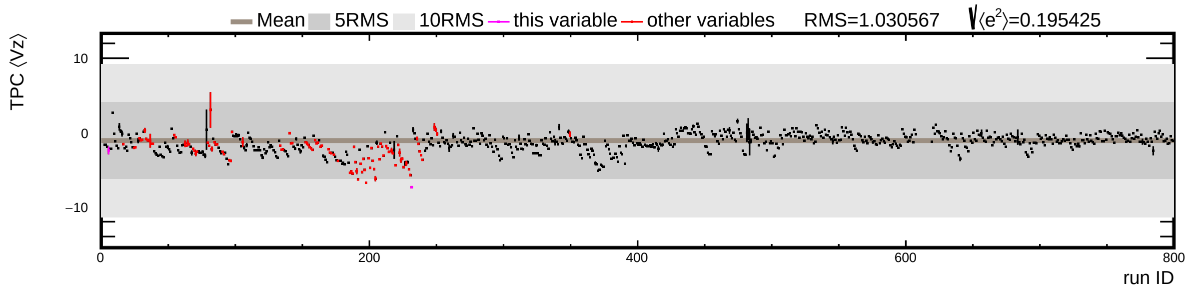

Figure 3.15. Run-by-run $\langle V_z \rangle$

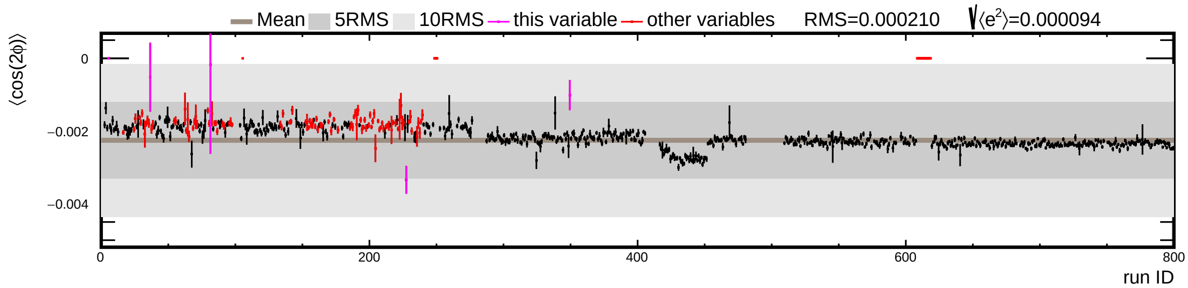

Figure 3.11. Run-by-run $\langle \cos 2\phi \rangle$

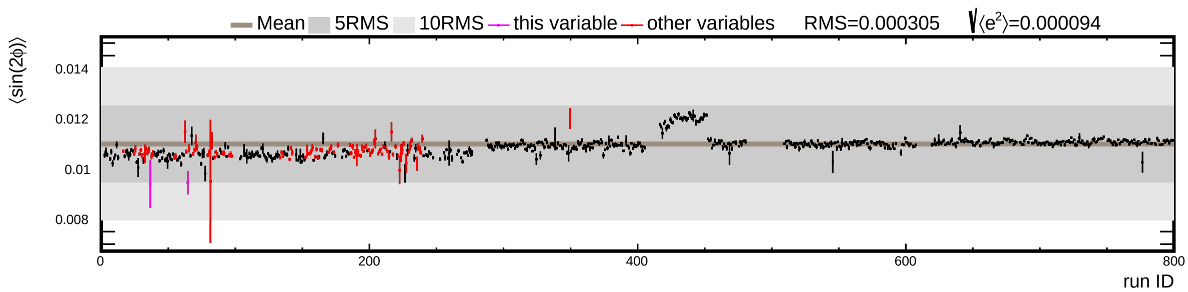

Figure 3.12. Run-by-run $\langle \sin 2\phi \rangle$

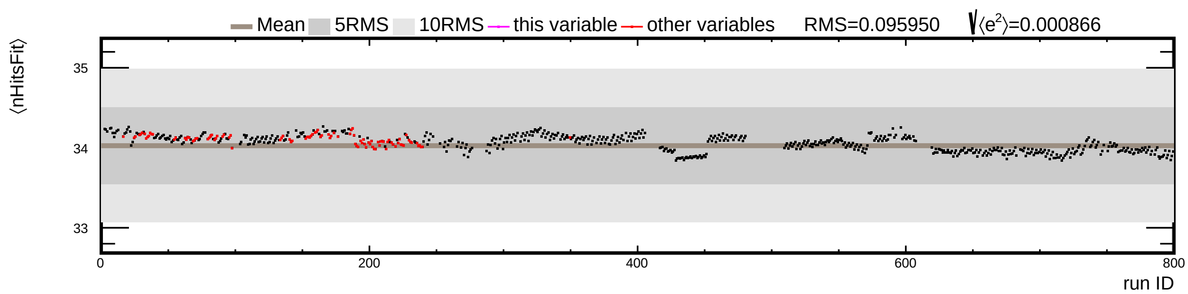

Figure 3.13. Run-by-run ⟨nHitsFit⟩

3.3 Centrality Definition `StRefMultCorr`

In heavy ion collisions, centrality describes how much the two nuclei overlap with each other in the collision between them, and is usually defined by the RefMult distribution with corrections and fittings, where “RefMult” means the reference multiplicity counted during data taking from middle TPC with $-0.5 < \eta < 0.5$ (cf. Fig. 3.16).

The centrality study for this dataset Run18AuAu27GeV has been done by Yiding Han and Zaochen Ye from Rice University [57]. Their study also identified some bad runs and removed the pileups, where pileup means two or more events misidentified as one single event. Based on their study, they calibrated the class `StRefMultCorr` for this dataset, which

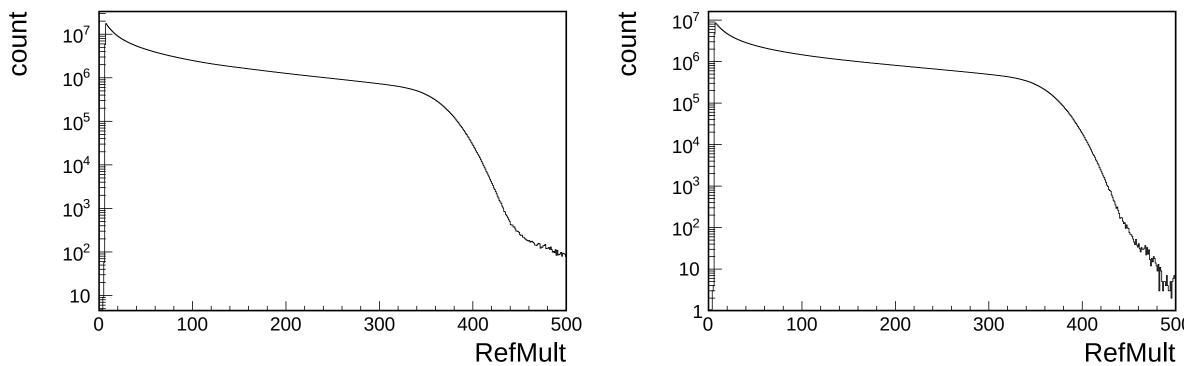

Figure 3.16. RefMult distribution. Raw count (left) and weighted count after pileup removal (right).

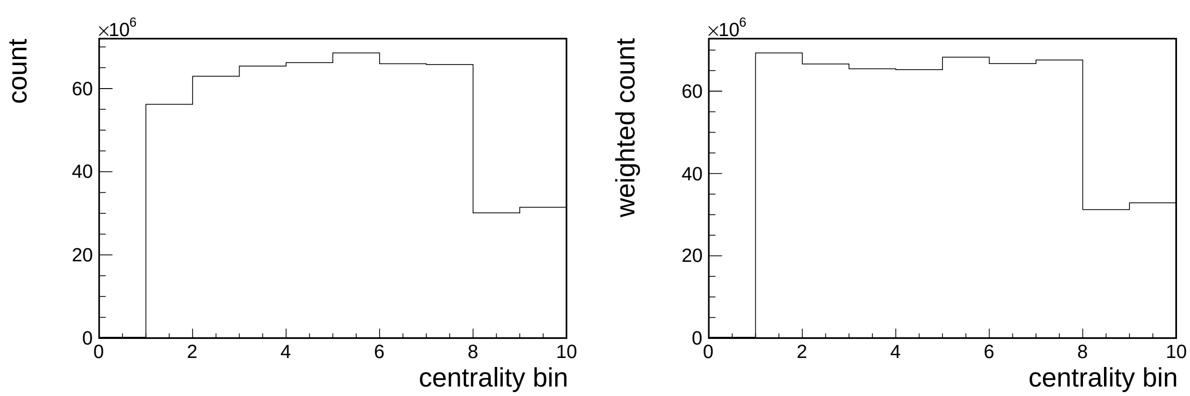

Figure 3.17. Event number of each centrality bin. Raw count (left) and weighted count after pileup removal (right).

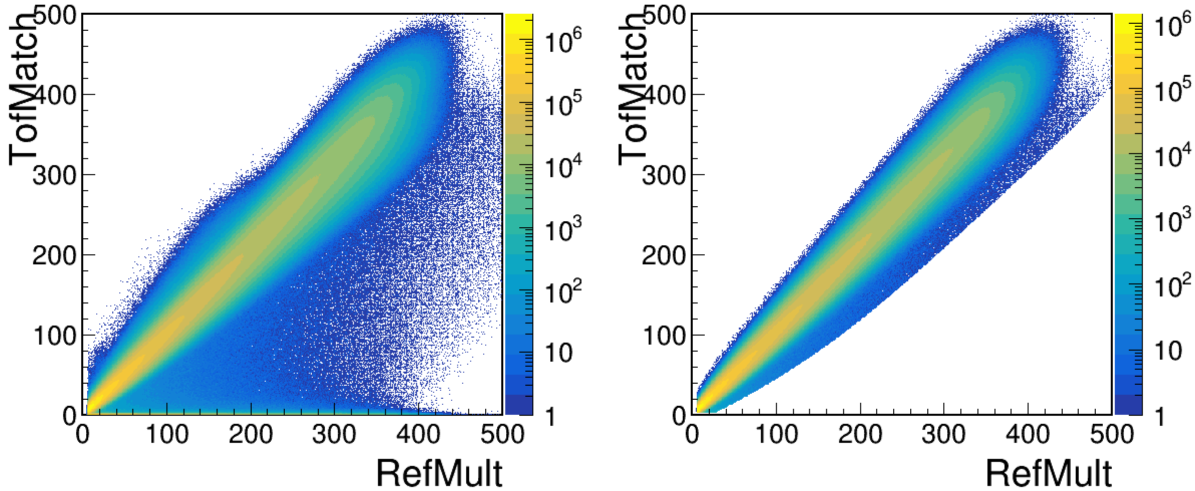

Figure 3.18. TofMatch vs RefMult plots. Raw count (left) and weighted count after pileup removal (right).

can be used to identify the centrality for each event of this dataset. This study just uses this class to get the centrality bin (cf. Fig. 3.17), and to remove bad runs and pileups (cf Fig. 3.16 and 3.18).

4. RECONSTRUCTION ALGORITHM

The Λ ($\bar{\Lambda}$) hyperons cannot reach TPC, because its decay length is about 7.89 cm [45], relatively short compared with the detector size of TPC. Even if Λ ($\bar{\Lambda}$) hyperons had reached TPC, they still cannot be detected directly, because they are neutral in charge. However, their charged decay daughters can be measured and used. The main decay channels of the Λ ($\bar{\Lambda}$) hyperons are $\Lambda \to p\pi^-$ ($\bar{\Lambda} \to \bar{p}\pi^+$) with branching ratio 63.9% and $\Lambda \to n\pi^0$ ($\bar{\Lambda} \to n\pi^0$) with branching ratio 35.8% [45], where we are only interested in the former, because decay daughters of the latter are neutral. Thus, in this study, we use protons (p, $\bar{p}$) and pions (π^-, π^+) to reconstruct Λ ($\bar{\Lambda}$).

This chapter reviews the algorithms to reconstruct particles from their decay daughters, which have been well-established in the previous researches.

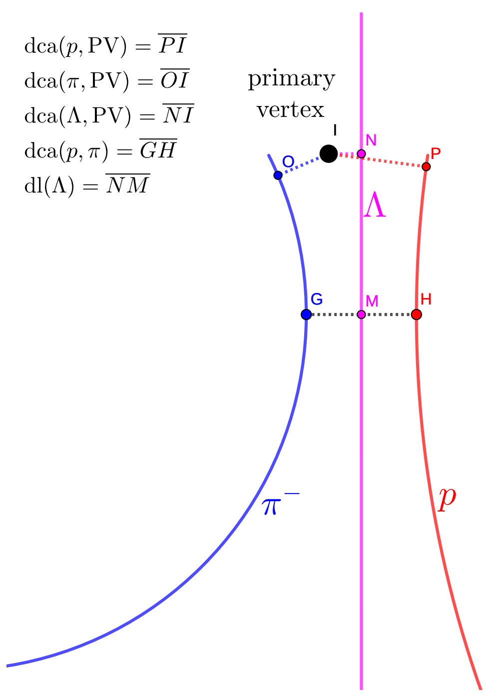

Figure 4.1. Λ decay topology.

Table 4.1. Topological cuts for Λ ($\bar{\Lambda}$) reconstruction. The numbers come from the previous studies of STAR [59], which was presented in QM2019 [60] where the table is listed on page 37 of the slides.

Centrality	dca(p, PV)	dca(π, PV)	dca(p, π)	dca(Λ, PV)	dl(Λ)
$0 - 10\%$	> 0.4 cm	> 1.5 cm	< 0.9 cm	< 0.8 cm	> 4.0 cm
$10 - 20\%$	> 0.4 cm	> 1.5 cm	< 0.9 cm	< 0.8 cm	> 4.0 cm
$20 - 30\%$	> 0.3 cm	> 1.3 cm	< 1.0 cm	< 0.9 cm	> 3.5 cm
$30 - 40\%$	> 0.2 cm	> 1.2 cm	< 1.0 cm	< 0.9 cm	> 3.5 cm
$40 - 50\%$	> 0.2 cm	> 1.0 cm	< 1.0 cm	< 1.0 cm	> 3.0 cm
$50 - 60\%$	> 0.2 cm	> 0.8 cm	< 1.1 cm	< 1.0 cm	> 3.0 cm
$60 - 70\%$	> 0.1 cm	> 0.8 cm	< 1.1 cm	< 1.1 cm	> 2.5 cm
$70 - 80\%$	> 0.1 cm	> 0.7 cm	< 1.2 cm	< 1.2 cm	> 2.5 cm

4.1 Conventional Topological Cut

The topological cut method is conventional to reconstruct a decayed particle from its decay daughters, and was used for Λ ($\bar{\Lambda}$) reconstructions [58]. This method assumes that the closest points between π^- track and p track (points G, H in Fig. 4.1) are their respective production vertices (the position where the particle is created), and their middle point (M) is the Λ's decay vertex (the position where the particle decays). Then, some (empirical) topological cuts are applied to the decay length (dl) and distance of closest approach (dca) between the two tracks or between one track and the primary vertex (PV, where the collision happens).

For Λ ($\bar{\Lambda}$) reconstruction, the topological cuts could be the numbers listed in the table 4.1 from the previous STAR study [59, 60].

Those assumptions of vertices are good estimations, but not necessary the optimal. To improve that, an algorithm based on the Kalman filter method is used recently in particle reconstruction.

4.2 Kalman Filter Method

The Kalman filter method [61, 62], also called linear quadratic estimation, is a special case of an earlier nonlinear filter developed by Stratonovich [63, 64, 65, 66]. The general idea of the Kalman filter method is to estimate the true value of the quantity from its measurements.

In terms of the reconstruction of decay parent particle, the position measurments of the decay vertex are its decay daughters' production vertices, which is not necessarily the simple "middle point" of the "closest points" used in the conventional topological cut method, but instead an "optimal point" around the "closest points" given by the algorithm.

4.2.1 General framework

In this section, we will briefly go through the general framework of the Kalman filter method with some math, where the contents are based on Maksym Zyzak's thesis [67] and Sergey Gorbunov's thesis [68].

Firstly, quantities are needed to set up to describe the Kalman filter method. The target quantities can be described as a vector called state vector $\boldsymbol{r}_k^t$, which is a vector of real numbers that represents the unknown quantities to be estimated. The superscript t stands for "*true*", and the subscript k indicates the time step, in case that the state vector has time dependence. $\boldsymbol{r}_k^t$ is unknown, but fixed for given k. Time evolution is assumed from time $k-1$ to time k:

$$\boldsymbol{r}_k^t = A_k \boldsymbol{r}_{k-1}^t + \boldsymbol{\nu}_k, \tag{4.1}$$

which is one kind of Markov chain [69]. In the time-evolution equation above, extrapolator A_k is a known linear operator represented as a matrix; process noise $\boldsymbol{\nu}_k$ is an unknown and random variable, which is assumed to be unbiased and its variance matrix Q_k is known:

$$\langle \boldsymbol{\nu}_k \rangle = \mathbf{0}, \qquad Q_k \equiv \mathrm{cov}(\boldsymbol{\nu}_k) = \langle (\boldsymbol{\nu}_k - \langle \boldsymbol{\nu}_k \rangle)(\boldsymbol{\nu}_k - \langle \boldsymbol{\nu}_k \rangle)^T \rangle = \langle \boldsymbol{\nu}_k \boldsymbol{\nu}_k^T \rangle. \tag{4.2}$$

The measurement of the target quantities can also be described as a vector $\boldsymbol{m}_k$, which is a known (measured) quantity linearly depending on the state vector $\boldsymbol{r}_k^t$:

$$\boldsymbol{m}_k = H_k \boldsymbol{r}_k^t + \boldsymbol{\eta}_k. \tag{4.3}$$

In the measurement equation above, model of measurement H_k is a known linear operator represented as a matrix; measurement error $\boldsymbol{\eta}_k$ is an unknown and random variable, which is assumed to be unbiased and its variance matrix V_k is known. In different time step $k \neq k'$, $\boldsymbol{\eta}_k$, $\boldsymbol{\eta}_{k'}$ are uncorrelated. The estimations for the state vector $\boldsymbol{r}_k^t$ can be calculated from the measurements, which is called the estimator $\boldsymbol{r}_k$.

Then, the Kalman filter method has the iterative steps shown as the following.

(1) Initialization step: Choose an approximate $\boldsymbol{r}_0$, whose covariance matrix is set to $C_0 =$ (a large positive number) $\cdot I$, where I means the identity matrix.

(2) Extrapolation step: Also called "priori estimation", an estimation based on measurements up to $\boldsymbol{m}_{k-1}$, before $\boldsymbol{m}_k$. It uses the known extrapolator A_k:

$$\begin{aligned}\tilde{\boldsymbol{r}}_k \equiv& A_k \boldsymbol{r}_{k-1},\\ \tilde{C}_k \equiv& \operatorname{cov}(\tilde{\boldsymbol{r}}_k - \boldsymbol{r}_k^t) = \operatorname{cov}(A_k \boldsymbol{r}_{k-1} - (A_k \boldsymbol{r}_{k-1}^t + \boldsymbol{\nu}_k))\\ =& \operatorname{cov}(A_k(\boldsymbol{r}_{k-1} - \boldsymbol{r}_{k-1}^t)) + \operatorname{cov}(\boldsymbol{\nu}_k) = A_k C_{k-1} A_k^T + Q_k.\end{aligned} \tag{4.4}$$

(3) Filtration step: Also called "posteriori" estimation based on measurements up to $\boldsymbol{m}_k$:

$$\begin{aligned}\text{measurement} \quad \boldsymbol{m}_k =& H_k \boldsymbol{r}_k^t + \boldsymbol{\eta}_k,\\ \text{innovation} \quad \boldsymbol{\zeta}_k =& \boldsymbol{m}_k - H_k \tilde{\boldsymbol{r}}_k,\\ \text{estimator} \quad \boldsymbol{r}_k =& \tilde{\boldsymbol{r}}_k + K_k \boldsymbol{\zeta}_k,\\ \text{covariance} \quad C_k =& \operatorname{cov}(\boldsymbol{r}_k - \boldsymbol{r}_k^t),\end{aligned} \tag{4.5}$$

where K_k is called the gain matrix which will be calculated later.

The covariance matrix can be expanded as the following:

$$\begin{aligned}C_k =& \operatorname{cov}(\boldsymbol{r}_k - \boldsymbol{r}_k^t) = \operatorname{cov}(\tilde{\boldsymbol{r}}_k + K_k \boldsymbol{\zeta}_k - \boldsymbol{r}_k^t)\\ =& \operatorname{cov}(\tilde{\boldsymbol{r}}_k + K_k(\boldsymbol{m}_k - H_k \tilde{\boldsymbol{r}}_k) - \boldsymbol{r}_k^t) = \operatorname{cov}(\tilde{\boldsymbol{r}}_k + K_k(H_k \boldsymbol{r}_k^t + \boldsymbol{\eta}_k - H_k \tilde{\boldsymbol{r}}_k) - \boldsymbol{r}_k^t)\\ =& \operatorname{cov}((I - K_k H_k)(\tilde{\boldsymbol{r}}_k - \boldsymbol{r}_k^t)) + \operatorname{cov}(K_k \boldsymbol{\eta}_k)\\ =& (I - K_k H_k)\tilde{C}_k (I - K_k H_k)^T + K_k V_k K_k^T\\ =& \tilde{C}_k - K_k H_k \tilde{C}_k - \tilde{C}_k H_k^T K_k^T + K_k(V_k + H_k \tilde{C}_k H_k^T) K_k^T.\end{aligned} \tag{4.6}$$

The total variance can be quantified as a number:

$$\sum_{\mathrm{i}} \mathrm{var}[(r_k)_{\mathrm{i}} - (r_k^t)_{\mathrm{i}}] = \mathrm{tr} C_k. \tag{4.7}$$

Then, the K_k matrix can be chosen to minimized $\mathrm{tr}C_k$:

$$\begin{aligned} \frac{\partial \mathrm{tr} C_k}{\partial K_k} &= -\tilde{C}_k^T H_k^T - \tilde{C}_k H_k^T + K_k(V_k + H_k \tilde{C}_k H_k^T) + K_k(V_k + H_k \tilde{C}_k H_k^T)^T \\ &= -2\tilde{C}_k H_k^T + 2K_k(V_k + H_k \tilde{C}_k H_k^T). \end{aligned} \tag{4.8}$$

The optimal point requires the derivative to be 0, then

$$K_k = \tilde{C}_k H_k^T (V_k + H_k \tilde{C}_k H_k^T)^{-1}, \tag{4.9}$$

which is called the Kalman gain matrix. Using this Kalman gain matrix, the Filtration step can be completed. When we plug the Eq. 4.9 into Eq. 4.5, the covariance in Eq. 4.5 becomes

$$C_k = \mathrm{cov}(\boldsymbol{r}_k - \boldsymbol{r}_k^t) = \tilde{C}_k - K_k H_k \tilde{C}_k. \tag{4.10}$$

The χ^2 test is by definition:

$$\chi_k^2 = \sum_{\mathrm{i}=1}^{k} (\boldsymbol{m}_{\mathrm{i}} - H_{\mathrm{i}} \boldsymbol{r}_k)^T V_{\mathrm{i}}^{-1} (\boldsymbol{m}_{\mathrm{i}} - H_{\mathrm{i}} \boldsymbol{r}_k) = \sum_{\mathrm{i}=1}^{k} \mathrm{tr}\left(V_{\mathrm{i}}^{-1} (\boldsymbol{m}_{\mathrm{i}} - H_{\mathrm{i}} \boldsymbol{r}_k)(\boldsymbol{m}_{\mathrm{i}} - H_{\mathrm{i}} \boldsymbol{r}_k)^T \right). \tag{4.11}$$

Reference [68] gives a recursive formula, which I have not really understood:

$$\chi_k^2 = \chi_{k-1}^2 + \boldsymbol{\zeta}_k^T \left(V_k + H_k \tilde{C}_k H_k^T \right)^{-1} \boldsymbol{\zeta}_k. \tag{4.12}$$

In the previous paragraphs, linear Kalman filter is discussed, while the reference [68] also discussed the nonlinear cases. When the measurement is nonlinear, we can use Taylor expansion at a certain state vector $\boldsymbol{r}_k^{lin}$ (can adapt in each step k):

$$\boldsymbol{m}_k(\boldsymbol{r}_k^t) \equiv \boldsymbol{h}_k(\boldsymbol{r}_k^t) + \boldsymbol{\eta}_k \approx \boldsymbol{h}_k(\boldsymbol{r}_k^{lin}) + H_k(\boldsymbol{r}_k^t - \boldsymbol{r}_k^{lin}) + \boldsymbol{\eta}_k, \tag{4.13}$$

where H_k is the hessian of $\boldsymbol{h}_k(\boldsymbol{r}_k)$ at $\boldsymbol{r}_k^{lin}$:

$$H_{k\ \text{(ij)}} = \left.\frac{\partial \boldsymbol{h}_k(\boldsymbol{r}_k)_{\text{(i)}}}{\partial \boldsymbol{r}_{k\ \text{(j)}}}\right|_{\boldsymbol{r}_k=\boldsymbol{r}_k^{lin}}. \tag{4.14}$$

Similarly for the extrapolator,

$$\tilde{\boldsymbol{r}}_k \equiv \boldsymbol{a}_k(\boldsymbol{r}_{k-1}^t) \approx \boldsymbol{a}_k(\boldsymbol{r}_{k-1}^{lin}) + A_k(\boldsymbol{r}_{k-1}^t - \boldsymbol{r}_{k-1}^{lin}), \qquad A_{k\ \text{(ij)}} = \left.\frac{\partial \boldsymbol{a}_k(\boldsymbol{r}_k)_{\text{(i)}}}{\partial \boldsymbol{r}_{k\ \text{(j)}}}\right|_{\boldsymbol{r}_k=\boldsymbol{r}_k^{lin}}. \tag{4.15}$$

With the linearizations above, the linear Kalman filter formula (Eq. 4.4, 4.5, 4.10) can be used with the only modification:

$$\boldsymbol{\zeta}_k = \boldsymbol{m}_k - \left(\boldsymbol{h}_k(\boldsymbol{r}_k^{lin}) + H_k(\tilde{\boldsymbol{r}}_k - \boldsymbol{r}_k^{lin})\right). \tag{4.16}$$

Further extensions or variations are also discussed in the Ref. [68], but here we select some of them and do not get into details.

- Extended measurement model: If the measurement has more dimensions than the state vector, a known matrix G_k can be used for projection:

  $$G_k(\boldsymbol{m}_k - \boldsymbol{\eta}_k) = H_k \boldsymbol{r}_k^t. \tag{4.17}$$

  The previous formula (Eq. 4.4, 4.5, 4.10) can still be used with the substitution:

  $$\boldsymbol{m}_k \to G_k \boldsymbol{m}_k, \qquad V_k \to G_k V_k G_k^T. \tag{4.18}$$

- Correlated measurement: If the error of measurement $\boldsymbol{m}_k$ is correlated with previous measurements, $\boldsymbol{m}_k$ and $\tilde{\boldsymbol{r}}_k$ are correlated by a known matrix $D_{k\ \text{(ij)}} \equiv \text{cov}(\boldsymbol{m}_{k\ \text{(i)}}, \tilde{\boldsymbol{r}}_{k\ \text{(j)}})$.

4.2.2 Application in reconstructing particle from its decay daughters

For the problem to reconstruct decayed particle from its decay daughters, the state vector is defined as

$$\boldsymbol{r}_k \equiv (x, y, z, p_x, p_y, p_z, E)^T = (\boldsymbol{v}_k, \boldsymbol{p}_k, E)^T = (\boldsymbol{v}_k, p_k)^T. \tag{4.19}$$

From the detector measurements, the final-state tracks are identified. We can get the closest points of two (or more) decay daughter tracks. The conventional method takes those points as the production vertices of the decay daughters and takes their center as the decay vertex, whereas Kalman filter optimizes the decay vertices around the closest points and regards each production vertex ($\boldsymbol{r}_k^d = (\boldsymbol{v}_k^d, p_k^d)^T$) as one measurement ($\boldsymbol{m}_k$) of the decay vertex $\boldsymbol{r} = \boldsymbol{r}_k$ with errors (V_k). The subscript k hereby means the k^{th} decay daughter. Due to uncertainties, one measurement could fluctuate on the track around the production vertex:

$$\boldsymbol{m}_k = \boldsymbol{r}_k^d + \begin{pmatrix} \boldsymbol{p}_k^d \\ \boldsymbol{p}_k^d \times \boldsymbol{B} q_k^d \\ 0 \end{pmatrix} s_k^d + \mathcal{O}((s_k^d)^2), \tag{4.20}$$

where $s_k^d = l_k^d / |\boldsymbol{p}_k^d|$ is the unknown length of shifts on the track divided by momentum, whose average value should be $\langle s_k^d \rangle = 0$ and variance $\sigma^2_{s_k^d}$.

The measurement in terms of the true decay vertex position ($\boldsymbol{v}_k^t$ of $\boldsymbol{r}_k^t$) is

$$G_k(\boldsymbol{m}_k - \boldsymbol{\eta}_k) = H_k \boldsymbol{r}_k^t, \qquad G_k = H_k = \begin{pmatrix} I_3 & 0 \end{pmatrix}, \tag{4.21}$$

since we only focus on the position. We also multiply Eq. 4.20 by the matrices (only leading order):

$$G_k \boldsymbol{m}_k = H_k \left(\boldsymbol{r}_k^d + \begin{pmatrix} \boldsymbol{p}_k^d \\ \boldsymbol{p}_k^d \times \boldsymbol{B} q_k^d \\ 0 \end{pmatrix} s_k^d \right) = H_k \boldsymbol{r}_k^t + H_k \left(\boldsymbol{r}_k^d - \boldsymbol{r}_k^t + \begin{pmatrix} \boldsymbol{p}_k^d \\ \boldsymbol{p}_k^d \times \boldsymbol{B} q_k^d \\ 0 \end{pmatrix} s_k^d \right). \tag{4.22}$$

Therefore, the measurement error is

$$\boldsymbol{\eta}_k = \boldsymbol{r}_k^d - \boldsymbol{r}_k^t + \begin{pmatrix} \boldsymbol{p}_k^d \\ \boldsymbol{p}_k^d \times \boldsymbol{B} q_k^d \\ 0 \end{pmatrix} s_k^d. \tag{4.23}$$

The covariance of measurement is

$$V_k = C_k^d + \begin{pmatrix} \boldsymbol{p}_k^d \\ \boldsymbol{p}_k^d \times \boldsymbol{B} q_k^d \\ 0 \end{pmatrix} \begin{pmatrix} \boldsymbol{p}_k^d \\ \boldsymbol{p}_k^d \times \boldsymbol{B} q_k^d \\ 0 \end{pmatrix}^T \sigma^2_{s_k^d}, \tag{4.24}$$

where $C_k^d \equiv \mathrm{cov}(\boldsymbol{r}_k^d - \boldsymbol{r}_k^t)$.

Since the decay vertex position is the same for all associated decay daughters, $A_k = I$, $\boldsymbol{\nu}_k = \mathbf{0}$. Then, the relationships become

$$\begin{aligned}
\boldsymbol{r}_k^t =& A_k \boldsymbol{r}_{k-1}^t + \boldsymbol{\nu}_k = \boldsymbol{r}_{k-1}^t, \\
Q_k \equiv& \mathrm{cov}(\boldsymbol{\nu}_k) = 0, \\
\tilde{\boldsymbol{r}}_k \equiv& A_k \boldsymbol{r}_{k-1} = \boldsymbol{r}_{k-1}, \\
\tilde{C}_k =& A_k C_{k-1} A_k^T + Q_k = C_{k-1}, \\
S_k \equiv& (G_k V_k G_k^T + H_k \tilde{C}_k H_k^T)^{-1} = (G_k V_k G_k^T + H_k C_{k-1} H_k^T)^{-1}, \\
K_k =& \tilde{C}_k H_k^T (G_k V_k G_k^T + H_k \tilde{C}_k H_k^T)^{-1} = C_{k-1} H_k^T S_k, \\
\boldsymbol{\zeta}_k =& G_k \boldsymbol{m}_k - H_k \tilde{\boldsymbol{r}}_k = G_k \boldsymbol{m}_k - H_k \boldsymbol{r}_{k-1}, \\
\chi_k^2 =& \chi_{k-1}^2 + \boldsymbol{\zeta}_k^T S_k \boldsymbol{\zeta}_k.
\end{aligned} \tag{4.25}$$

Since $G_k = H_k = \begin{pmatrix} I_3 & 0 \end{pmatrix}$ are simple projection matrices, reference [68] writes the above equations in augmented format.

We focused on the position only, so the current updated estimator is not the complete. To avoid confusion, we add the superscript f:

$$\begin{aligned} \boldsymbol{r}_k^f =& \tilde{\boldsymbol{r}}_k + K_k \boldsymbol{\zeta}_k, \\ C_k^f =& \tilde{C}_k - K_k H_k \tilde{C}_k. \end{aligned} \tag{4.26}$$

Reference [68] also shows how to update the 4-momentum of $\boldsymbol{r}_k$. Due to momentum conservation, $\boldsymbol{p}_k^d$ should be added to $\boldsymbol{p}_{k-1}$ with some correction. I have not fully understood the corrections, but I just list them below:

$$\begin{aligned} \boldsymbol{m}_k^f =& \boldsymbol{m}_k - V_k H_k^T S_k \boldsymbol{\zeta}_k, \\ V_k^f =& V_k - V_k H_k^T S_k H_k V_k, \\ D_k^f =& V_k H_k^T S_k H_k \tilde{C}_k = V_k H_k^T S_k H_k C_{k-1}, \end{aligned} \tag{4.27}$$

$$\begin{aligned} \boldsymbol{r}_k =& \boldsymbol{r}_k^f + F_k \boldsymbol{m}_k^f, \qquad F_k = \mathrm{diag}(0, I_4), \\ C_k =& C_k^f + A_k D_k^f + D_k^{f\,T} A_k^T + A_k V_k^f A_k^T. \end{aligned} \tag{4.28}$$

4.2.3 `KFParticle`

`KFParticle` package is invented by FIAS (Frankfurt Institute for Advanced Studies) group, M. Zyzak [67, 70], S. Gorbunov [68]. As mentioned before, Kalman filter method needs to know the covariance matrices and model, so each collaboration should have their own calibration. The package TMVA (Toolkit for MultiVariate data Analysis) is used to optimize the calibrations. To increase the computing speed, the array-based package SIMD (Single Instruction/Multiple Data) is used, which can use parallel computation and GPU. Based on the original `KFParticle` package and STAR calibrations, STAR experts (Yuri Fisyak, et al.) developed `StKFParticle` and `StKFParticleInterface` for users. Reference [70] gives the tutorial and code sample.

Some useful links for `KFParticle` in STAR analysis:
https://drupal.star.bnl.gov/STAR/subsys/hlt/kfparticle-tutorial,
https://www.star.bnl.gov/webdata/dox/html/classKFParticle.html.

4.3 Comparison Between the Two Methods

To compare the above two methods, they both are used for the same dataset, from which the invariant mass distributions are calculated for Λ and $\bar{\Lambda}$ hyperons. For the centrality range $30 \sim 40\%$, Fig. 4.2 (Λ) and 4.3 ($\bar{\Lambda}$) show the conventional topological cut method results on the left and `KFParticle` package results on the right. All those distributions are fitted by a double-Gaussian (signal) plus a first-order polynomial (background). It is obvious that `KFParticle` has much smaller background contamination, while the signal is not affected much, rendering a significantly higher signal over background ratio than the conventional

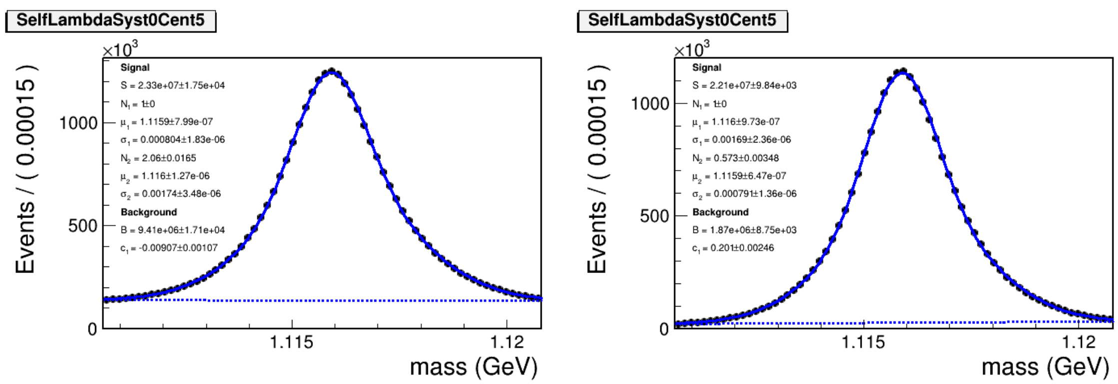

Figure 4.2. Invariant mass distribution of the reconstructed Λ hyperon by the conventional topological cut method (left) and the `KFParticle` package (right). Centrality $30 \sim 40\%$.

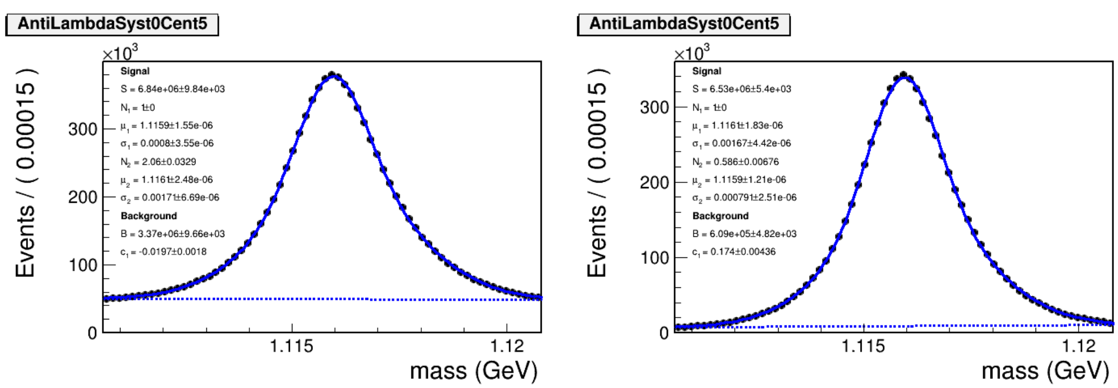

Figure 4.3. Invariant mass distribution of the reconstructed $\bar{\Lambda}$ hyperon by the conventional topological cut method (left) and the `KFParticle` package (right). Centrality $30 \sim 40\%$.

topological cut method. Moreover, `KFParticle` has narrower signal peak, which means better resolution.

5. DATA ANALYSIS

After the dataset preparation (Chapter 3), this chapter goes to the details of this analysis. Roughly speaking, this analysis first goes along two paths: Λ ($\bar{\Lambda}$) reconstructions and CME observable measurements. Then, the two paths meet at the event-by-event correlations (Chapter 6).

For the Λ ($\bar{\Lambda}$) reconstructions, we use the identified protons and pions from TPC, together with the `KFParticle` algorithm (reviewed in Chapter 4). After proper background subtraction, we can get the polarization (P) [1, 2] and handedness imbalance [4] (Δn^{obs}) of Λ, $\bar{\Lambda}$, and their sum for each event.

For the CME observable measurements, we use the unidentified charged hadrons from TPC, and exclude those already used in Λ ($\bar{\Lambda}$) reconstruction. The exclusion here should not make any big difference because the Λ ($\bar{\Lambda}$) numbers per event are quite small (cf. Fig. 5.10). Since the CME observables are azimuthal correlations, the TPC efficiency correction is applied. Then, Δa_1 and $\Delta\gamma$ can be calculated for each event.

The track-level cuts are listed for each path respectively in this chapter. The event planes measured by EPD are used for both paths.

5.1 Particle Identification

STAR detectors can identify the directly measured particles like pions, kaons, and protons from TPC or TOF as we mentioned in the previous sections (Sec. 2.1, 2.3).

In TPC, the energy loss $\mathrm{d}E/\mathrm{d}x$ is measured for each detected particle. If we plot the particle distribution on energy loss and rigidity ($|\vec{p}|/q$, charge sign $q = \pm 1$, see Fig. 5.1), different types of particles have distinguishable patterns in certain ranges, which are the characteristic energy loss curves as functions of rigidity. By fitting on this 2D distribution of one particle type, we can get the mean value and standard deviation of its energy loss as a function of rigidity. For a measured particle, $n\sigma\{\mathrm{d}E/\mathrm{d}x\}$ is the difference between its energy loss and the mean value then scaled by the standard deviation.

In TOF, the squared mass m^2 is measured for each detected particle. If we plot the particle distribution on squared mass and rigidity (Fig. 5.3), different types of particles have

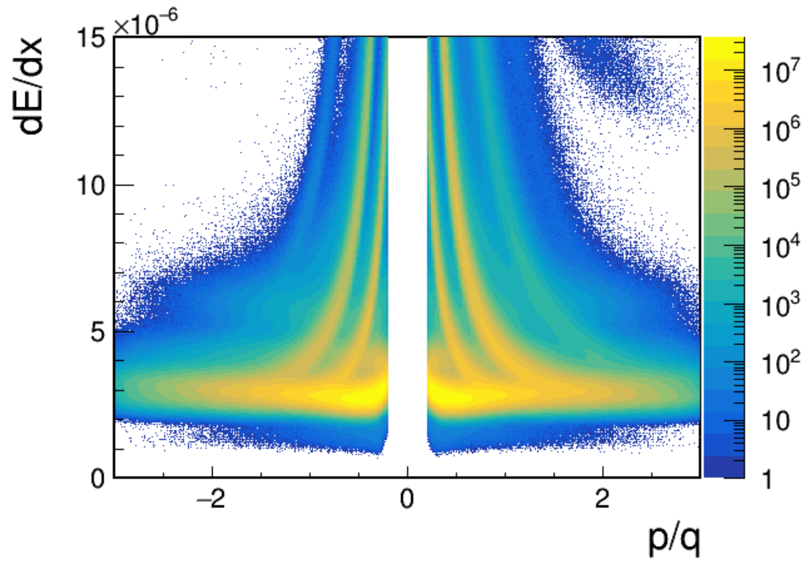

Figure 5.1. TPC energy loss

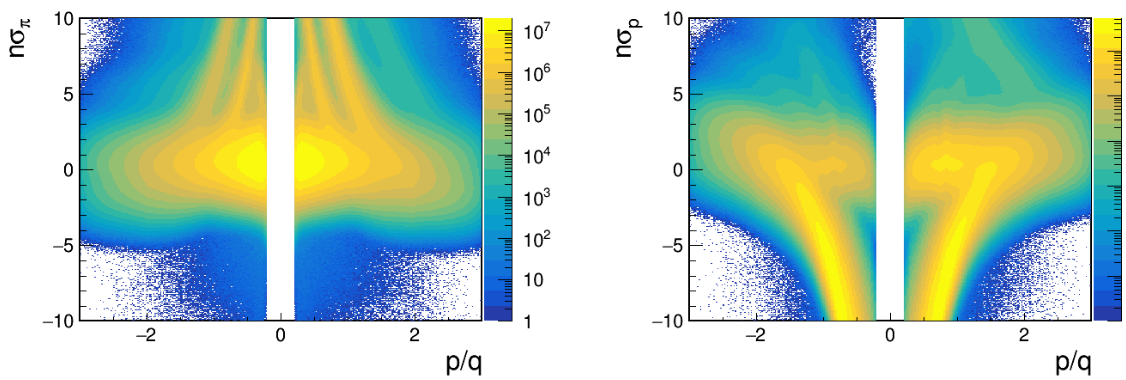

Figure 5.2. TPC $n\sigma\{\mathrm{d}E/\mathrm{d}x\}$ for pion (left) and proton (right)

distinguishable patterns in certain ranges, which are the characteristic squared mass curves as functions of rigidity. By fitting on this 2D distribution of one particle type, we can get the mean value and standard deviation of its squared mass as a function of rigidity ($q|\vec{p}|$). For a measured particle, $n\sigma\{m^2\}$ is the difference between its squared mass and the mean value then scaled by the standard deviation.

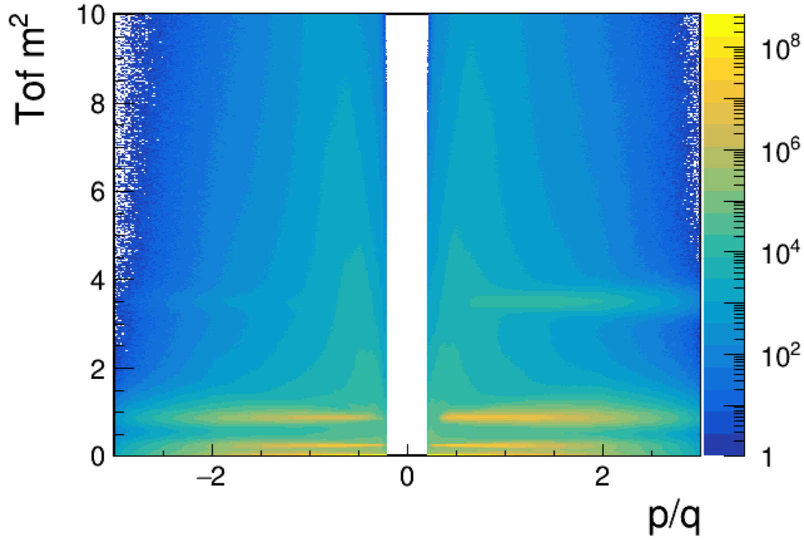

Figure 5.3. TOF squared mass m^2

In this analysis, we need to identify protons and pions for Λ ($\bar{\Lambda}$) reconstruction. The following bullets show the criterias given by STAR `StKFParticle` package used in this analysis.

- proton:

  If this particle is only detected by TPC, then the cuts are $|q| = 1$, $n\sigma_p\{\mathrm{d}E/\mathrm{d}x\} < 3$. If this particle is detected by both TPC and TOF, then the cuts are $|q| = 1$, $n\sigma_p\{\mathrm{d}E/\mathrm{d}x\} < 3$, $n\sigma_p\{m^2\} < 3$.

- pion:

  If this particle is only detected by TPC, then the cuts are $|q| = 1$, $n\sigma_\pi\{\mathrm{d}E/\mathrm{d}x\} < 3$. If this particle is detected by both TPC and TOF, then the cuts are $|q| = 1$, $n\sigma_\pi\{\mathrm{d}E/\mathrm{d}x\} < 3$, $n\sigma_\pi\{m^2\} < 3$.

For Δa_1 and $\Delta\gamma$ calculation, the unidentified charged hadrons are used, without the above selections.

5.2 Track Quality Cuts

This study uses tracks for two different purposes:

(1) primordial particles to calculate CME observables.

(2) secondary protons and pions for Λ ($\bar{\Lambda}$) reconstruction.

There are some common cuts for all particles, and specific cuts for each purpose respectively, which are listed in Table 5.1. In this table, "nHitsFit" is the number of hits used to reconstruct this track; "nHitsMax" is a soft upper limit for nHitsFit; "gDca" stands for the distance of the closest approach to the primary vertex for global tracks.

Table 5.1. Track quality cuts. The numbers in the parentheses are the systematical variations for track-level cuts.

	primordial particles for CME observable	secondary protons and pions for Λ ($\bar{\Lambda}$) reconstruction
common cuts	nHitsFit ≥ 15 $(10, 20)$	
specific cuts	gDca < 1.0 $(0.8, 2.0)$ cm 0.2 GeV/$c \leq p_T \leq 2.0$ GeV/c $-1 \leq \eta \leq 1$ $0.52 \leq \frac{\text{nHitsFit}}{\text{nHitsMax}} \leq 1.05$	identified as proton/pion (Sec. 5.1) `KFParticle` package For reconstructed Λ ($\bar{\Lambda}$) 0.4 GeV/$c < p_{T,\Lambda} < 3.0$ GeV/c

5.3 TPC Efficiency Correction

Collisions do not have azimuthal preference in the Lab frame, so ideally the azimuthal distribution (ϕ) should be uniform in $[0, 2\pi)$. However, the detector, Time Projection Chamber (TPC), is not perfectly a uniform cylinder equally covering the azimuthal angle. Instead, TPC is made by 12 sectors each side (East/West side) (see Fig. 2.3 in Sec. 2.1). The two sides are separated by a central membrane.

It is harder to detect particles from the edge of each sector than other positions, so the azimuthal detection efficiency is periodically lower in those directions. Other than that, the sectors are not perfectly identical to each others. Their different electronic performances contribute additional efficiency changes among different directions. For example, the sector near 330° (about $315 \sim 345°$) has obviously lower efficiency than other sectors (see Fig. 5.4).

To correct this detector effect, we first applied the technique called "reweighting". We divide the events into 18 (9×2) categories according to the centraltiy bins (9 types) and vectex V_z position (2 types, $V_z < 0$ and $V_z > 0$). For each event category, we divide the tracks into 70 ($2 \times 5 \times 7$) categories according to charge sign (2 types, + and −), η ranges (5 types, $-1.0 < \eta < -0.6$, $-0.6 < \eta < -0.2$, $-0.2 < \eta < 0.2$, $0.2 < \eta < 0.6$, $0.6 < \eta < 1.0$), p_T ranges (7 types, $0.0 < p_T < 0.4$, $0.4 < p_T < 0.6$, $0.6 < p_T < 0.8$, $0.8 < p_T < 1.0$, $1.0 < p_T < 1.4$, $1.4 < p_T < 2.0$, $p_T > 2.0$ GeV). Therefore, there are totally 1260 categories. For each category, we calculate the distribution. Ideally, the ϕ distribution $f(\phi)$ of each category should be flat. To achieve that, we can reset the weight for each ϕ bin, which can be calculated by

$$w(\phi) = \frac{1}{2\pi f(\phi)} \int_0^{2\pi} f(\phi) d\phi. \tag{5.1}$$

However, there could be some dead channels where $f(\phi) = 0$ or very small, which should not be counted. Therefore, we set the weight to be 0 if calculated value from Eq. 5.1 is larger than 10. After reweighting, the ϕ distribution becomes quite flat, which is shown by the red curve in Fig. 5.4.

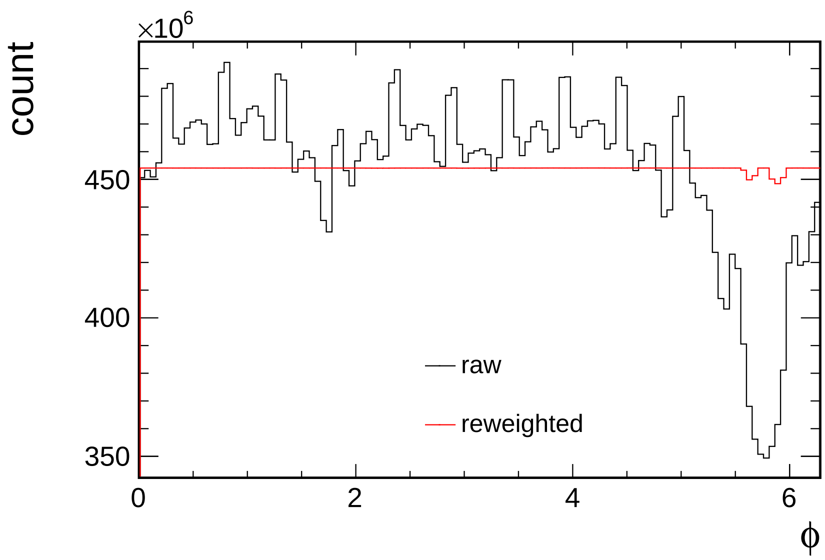

Figure 5.4. Particle azimuthal distribution detected from TPC. The black curve is the raw distribution, and the red curve is the reweighted distribution.

After reweighting, since the distribution is flat, the average values $\langle\sin(n\phi)\rangle$, $\langle\cos(n\phi)\rangle$ should be by definition 0. However, there could still be some residual fluctuations due to the dead channels or the finite bin size, so we can continue to do recentering for the γ and a_1 correlators.

$$\begin{aligned} \cos(n\phi) &\Rightarrow \cos(n\phi) - \langle\cos(n\phi)\rangle, \\ \sin(n\phi) &\Rightarrow \sin(n\phi) - \langle\sin(n\phi)\rangle. \end{aligned} \tag{5.2}$$

The raw TPC measurements are directly used for the Λ ($\bar{\Lambda}$) reconstructions and their polarization calculations.

5.4 Event Plane Reconstruction

The n^{th}-order event plane Ψ_n is defined as

$$\Psi_n = \frac{1}{n}\arctan\left(\frac{\sum_{\mathrm{i}}\sin n\phi_{\mathrm{i}}}{\sum_{\mathrm{i}}\cos n\phi_{\mathrm{i}}}\right), \tag{5.3}$$

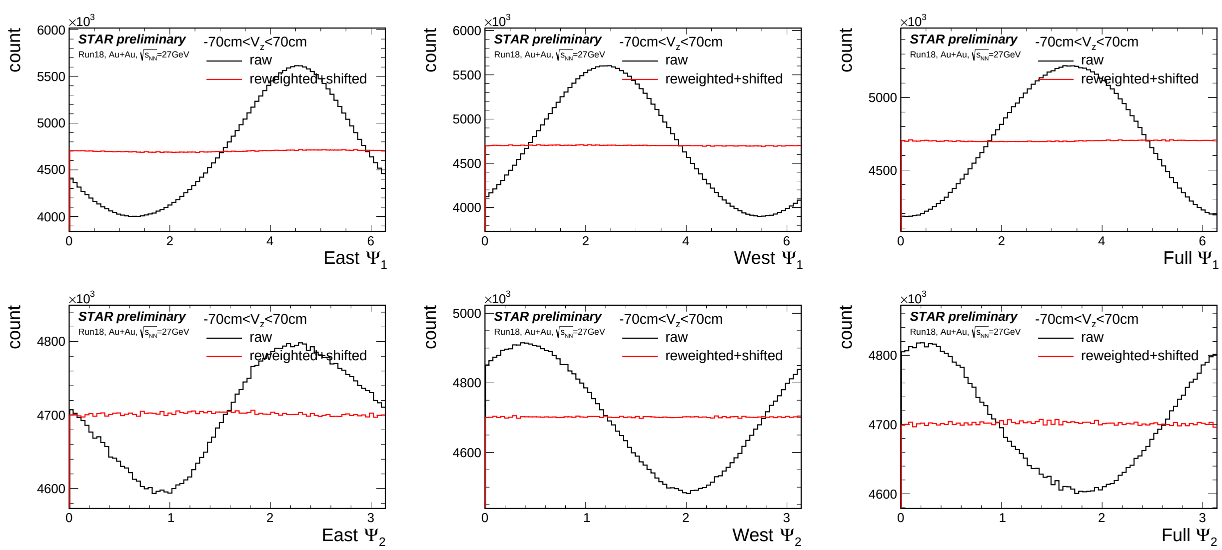

Figure 5.5. EPD Ψ_n distributions. The default cut $|V_z| < 70$ cm is used. The raw (black) and corrected (red) distributions are plotted together.

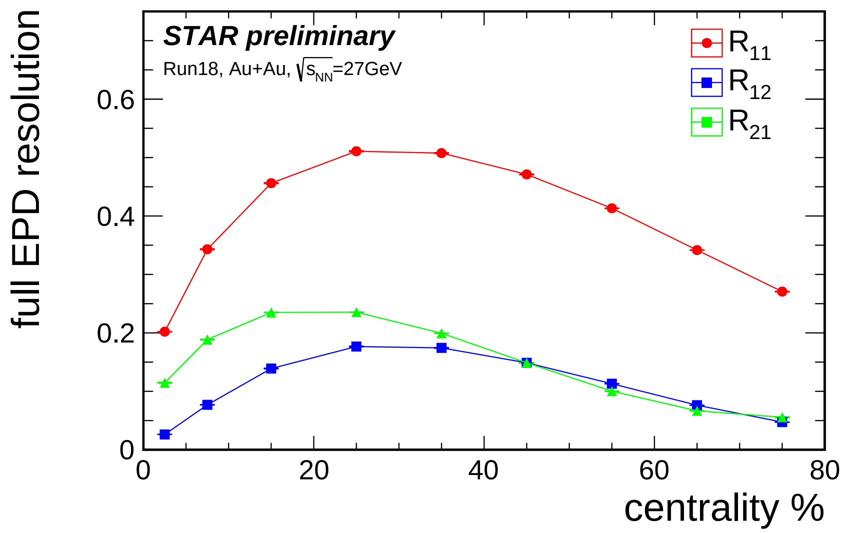

Figure 5.6. EPD Ψ_n resolutions. The default cut $|V_z| < 70$ cm is used. Two variations on V_z is used to calculate the systemaical uncertainty, which is too small to be visible on the plot.

where the arctan function is signed and returns value in $[-\pi, \pi)$ range. In `C++` code, it is the `atan2` function.

This analysis uses the Event Plane Detector (EPD) measurements to reconstruct the event planes (cf. Sec. 2.2), which means $\phi_{\rm i}$ in Eq. 5.3 comes from EPD hits.

STAR has an existing standard package `StEpdEpFinder` for EPD [71], which takes EPD v_1 as the input weight as a function of η [72]. Similar to TPC, EPD also needs efficiency correction due to the detector effect for Ψ_n, and `StEpdEpFinder` can do the reweighting and shifting automatically. The reweighting has already been mentioned in Sec. 5.3. The details of event plane (Ψ_n) shifting has been thoroughly discussed in Ref. [73].

$$n\Delta\Psi_n = \sum_{k=1}^{k_{\max}} \frac{2}{k} \left(-\langle \sin(kn\Psi_n)\rangle \cos(kn\Psi_n) + \langle \cos(kn\Psi_n)\rangle \sin(kn\Psi_n)\right). \tag{5.4}$$

From my understanding, recentering can be regarded as a low-order shifting, and shifting can be regarded as the generalized format of recentering.

In this analysis, we directly use the package `StEpdEpFinder`. After the reweighting and shifting (up to 20$^{\rm th}$ order), the event plane distributions are shown in Fig. 5.5. The black curves are the raw distribtuions of the reconstructed event plane from EPD, while the red curves are the corrected ones after reweighting and shifting. After correction, the Ψ_n distributions are very flat compared to the raw ones.

The resolution of the event planes measured from EPD is shown in Fig. 5.6. The notations R_{mk} is defined in the flow method paper [73].

$$R_{mk} = \langle \cos\left(mk(\Psi_m - \Psi_{\mathrm{RP}})\right)\rangle . \tag{5.5}$$

When a correlator uses $n\Psi_{\mathrm{RP}}$, we can use $n\Psi_m$ with R_{mk} as an estimation, where $n = mk$ are integers. We can directly measure R_{m1} by using subevent method.

$$R_{m1}^{\mathrm{sub}} = \sqrt{\langle \cos m(\Psi_m^E - \Psi_m^W)\rangle}. \tag{5.6}$$

Then, we can calculate the χ_m^{sub} from R_{m1}^{sub} by modified Bessel functions (Eq. 5.7). The full event is then $\chi_m = \sqrt{2}\chi_m^{\mathrm{sub}}$, and therefore the full event resolution is R_{mk} calculated from Eq. 5.7 with χ_m.

$$R_{mk} = \frac{\sqrt{\pi}}{2\sqrt{2}}\chi_m \mathrm{e}^{-\chi_m^2/4}\left[I_{\frac{k-1}{2}}(\chi_m^2/4) + I_{\frac{k+1}{2}}(\chi_m^2/4)\right], \tag{5.7}$$

where I_ν is the modified Bessel function of order ν [73].

5.5 Λ and $\bar{\Lambda}$ Reconstruction

The `KFParticle` package has been used to reconstruct Λ ($\bar{\Lambda}$) from decays $\Lambda \to p + \pi^-$ ($\bar{\Lambda} \to \bar{p} + \pi^+$), as mentioned in Chapter 4. This package can use the TPC and TOF information to identify those directly measured particles–pions and protons, as shown in Sec. 5.1. In addition, the track quality cuts are applied as mentioned in Sec. 5.2.

The mass spectra of the reconstructed Λ and $\bar{\Lambda}$ are shown in Fig. 5.7 (a), while Fig. 5.7 (b) shows the peak region ($m_{\Lambda/\bar{\Lambda}} \pm 0.005$ GeV, $1.110683 \sim 1.120683$ GeV bounded by red dashed lines) and the off-peak regions ($1.090 \sim 1.105$ GeV and $1.125 \sim 1.180$ GeV bounded by blue dashed lines). The peak region is still a mixture of signal and background, so we

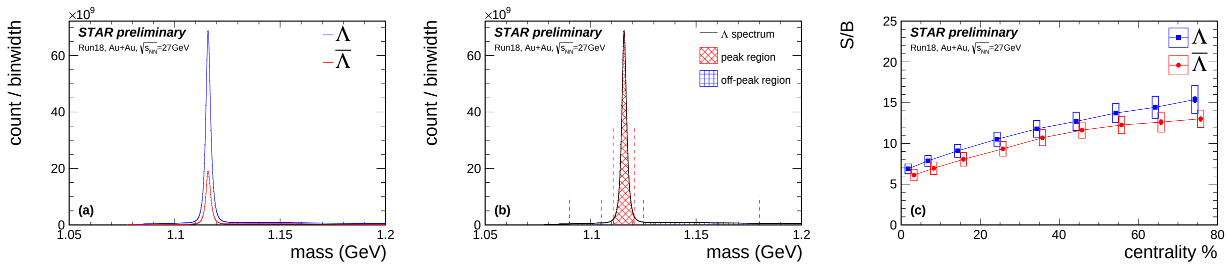

Figure 5.7. (a) the reconstructed Λ ($\bar{\Lambda}$) mass spectra in centrality range 0-80% Au+Au collisions at $\sqrt{s_{\mathrm{NN}}} = 27$ GeV (Run18). The `KFParticle` package is used to reconstruct Λ ($\bar{\Lambda}$) from protons and pions. The track quality cuts are listed in Sec. 5.2. (b) illustration of mass regions for Λ (and $\bar{\Lambda}$) candidates and combinatoric background. The candidates are selected in the peak region ($1.110683 \sim 1.120683$ GeV bounded by red dashed lines) and the background is assessed by the off-peak region ($1.090 \sim 1.105$ GeV and $1.125 \sim 1.180$ GeV bounded by blue dashed lines). (c) signal to background ratio in the Λ ($\bar{\Lambda}$) mass on-peak region as functions of centrality.

need to fit the mass spectra of this region by a function including signal (double-Gaussian) and background (1$^{\mathrm{st}}$-order polynomial). Then, the number of signal particle (S) and background particle (B) can be extracted in each centrality bin for each systematical variations respectively. The right plots of Fig. 4.2 and 4.3 show examples of the fittings. The S/B ratio is shown in Fig. 5.7 (c). For further purity correction, the off-peak regions (Fig. 5.7 (b)) will be used to estimate the background baseline.

In Fig. 5.7, the Λ ($\bar{\Lambda}$) peak seems quite sharp with a very low background, which is also quantified by the large S/B ratio. This indicates the high efficiency of the `KFParticle` package in Λ ($\bar{\Lambda}$) reconstruction, which is an advantage over the conventional topological cut method. The detailed comparison and discussion are available in Sec. 4.3.

It also shows that more Λ hyperons are measured/reconstructed than $\bar{\Lambda}$. This is mainly because of the "baryon stopping effect". The large stopping of the participant baryons is found in experiments [74, 75] and explained in theory [76], which could be quantified by a big change in rapidity (Δy) before and after the collision. In heavy-ion collisions, the participant baryons are the nucleons of the two heavy ions participating in the collision. They are slowed down in z-direction and therefore contributing to the fireball evolution. Since they are all

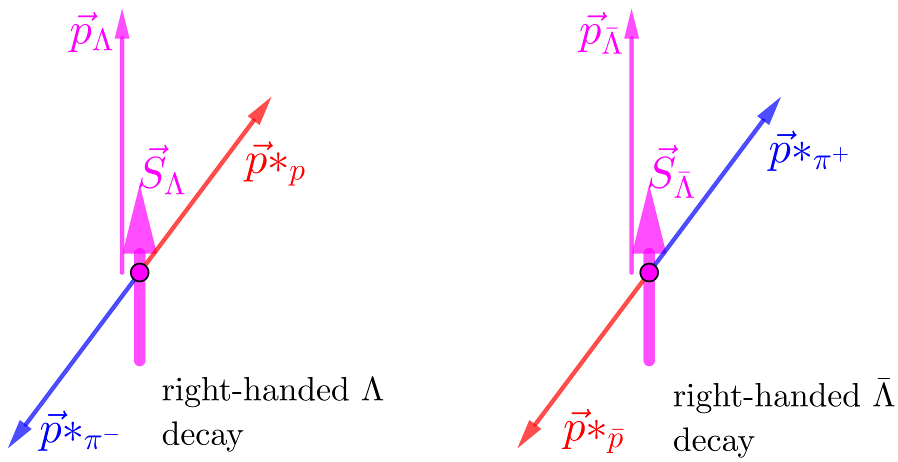

Figure 5.8. The schematic diagram for the observed handedness for Λ and $\bar{\Lambda}$ in their respective rest frame. The right handedness is taken as an example.

baryons at the first place, they make the final state more baryons than anti-baryons, which accounts for the more Λ we see than $\bar{\Lambda}$.

5.6 Λ and $\bar{\Lambda}$ Handedness

For a decay $\Lambda \to p + \pi^-$ (or $\bar{\Lambda} \to \bar{p} + \pi^+$), the spin direction of Λ ($\bar{\Lambda}$) can be approximated by its decay daughter proton's momentum $\vec{p}^*_p$ ($-\vec{p}^*_{\bar{p}}$) in the rest frame of that Λ ($\bar{\Lambda}$). On the other hand, the momentum of Λ ($\bar{\Lambda}$), $\vec{p}_\Lambda$ ($\vec{p}_{\bar{\Lambda}}$), can be reconstructed by its decay daughters. Then, the helicity sign (handedness) of Λ ($\bar{\Lambda}$) can be estimated by $\vec{p}^*_p \cdot \vec{p}_\Lambda$ ($\vec{p}^*_{\bar{p}} \cdot \vec{p}_{\bar{\Lambda}}$).

$$
\begin{aligned}
&\begin{cases}
\vec{p}^*_p \cdot \vec{p}_\Lambda < 0 & \Rightarrow \quad \Lambda_L : \text{“left-handed” } \Lambda \\
\vec{p}^*_p \cdot \vec{p}_\Lambda > 0 & \Rightarrow \quad \Lambda_R : \text{“right-handed” } \Lambda
\end{cases} \\
&\begin{cases}
\vec{p}^*_{\bar{p}} \cdot \vec{p}_{\bar{\Lambda}} < 0 & \Rightarrow \quad \bar{\Lambda}_R : \text{“right-handed” } \bar{\Lambda} \\
\vec{p}^*_{\bar{p}} \cdot \vec{p}_{\bar{\Lambda}} > 0 & \Rightarrow \quad \bar{\Lambda}_L : \text{“left-handed” } \bar{\Lambda}
\end{cases}
\end{aligned}
\tag{5.8}
$$

Figure 5.8 shows the schematics for the right-handed Λ and $\bar{\Lambda}$ in their respective rest frame.

To make connection from the observed to the true Λ ($\bar{\Lambda}$) handedness, detector effects and decay angular distribution need to be considered. In this exploratory study we will only

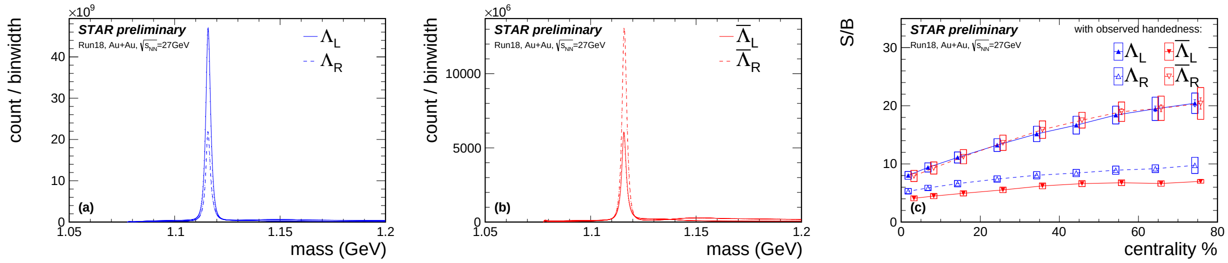

Figure 5.9. The measured left- and right-handed Λ (a) and $\bar{\Lambda}$ (b) reconstructed invariant mass spectra in centrality range 0-80% Au+Au collisions at $\sqrt{s_{\rm NN}}$ = 27 GeV (Run18). The `KFParticle` package is used to reconstruct Λ ($\bar{\Lambda}$) from protons and pions. The daughter track cuts are listed in Sec. 5.2. (c) Signal to background ratio in the Λ ($\bar{\Lambda}$) mass on-peak region as a function of centrality for each observed handedness.

consider the observed number of left/right-handed $\Lambda/\bar{\Lambda}$ ($N_L^{\rm obs}$, $N_R^{\rm obs}$ for $\Lambda/\bar{\Lambda}$), and then the observed difference between the number of left- and right-handed Λ ($\bar{\Lambda}$) after normalization, which is referred to as

$$\Delta n^{\rm obs} \equiv \frac{N_L^{\rm obs} - N_R^{\rm obs}}{\left\langle N_L^{\rm obs} + N_R^{\rm obs} \right\rangle}. \tag{5.9}$$

The superscripts "obs" means "observed" handedness. The $\Delta n^{\rm obs}$ will be calculated for Λ, $\bar{\Lambda}$, and their sum respectively.

Figure 5.10 shows the event average of $N^{\rm obs}$ for left/right-handed $\Lambda/\bar{\Lambda}$ in each centrality bin, without correction for the "Lambda efficiency" detector effect (which is discussed in the next paragraph). The "on-peak total" (green square) is calculated from all Λ ($\bar{\Lambda}$) candidates in the peak region. The "off-peak bkg" (blue circle) is calculated from all Λ ($\bar{\Lambda}$) candidates in

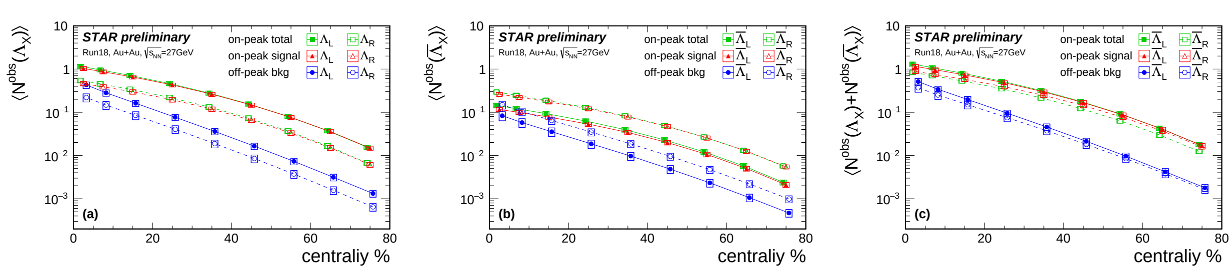

Figure 5.10. Observed handed Λ (a), $\bar{\Lambda}$ (b), and their sum (c) number per event for each centrality bin ("Lambda efficiency" detector effect uncorrected).

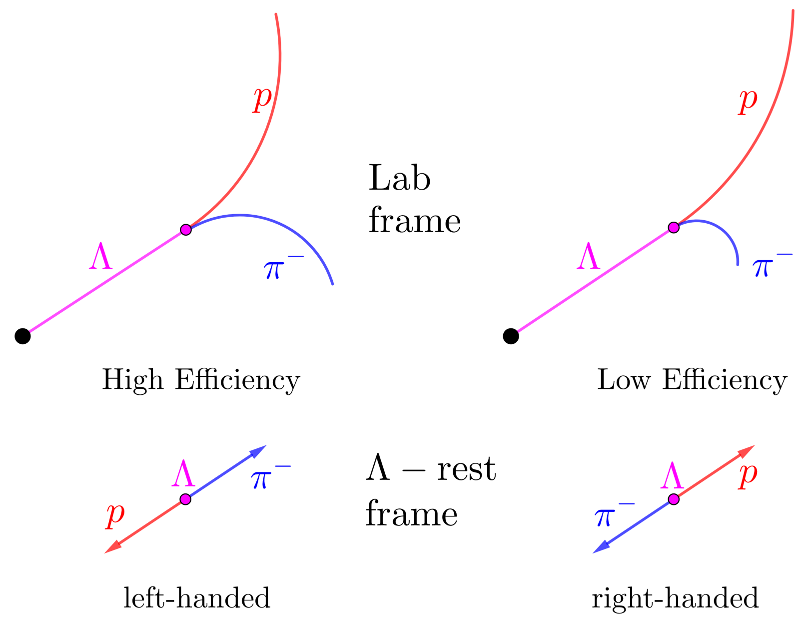

Figure 5.11. The schematic diagram for Lambda efficiency. This cartoon is based on Ref. [59] and page 64 of Ref. [77].

the off-peak regions. The "on-peak signal" (red triangle) is calculated from "on-peak total" with the corresponding S/B ratio, separately for left/right-handed $\Lambda/\bar{\Lambda}$ (see Fig. 5.9 (c)). The average Λ ($\bar{\Lambda}$) numbers per event are less than 2 in central collisions and down to 10^{-3} in peripheral collisions, much smaller than the multiplicity (RefMult $\sim$ 100, cf. Fig. 3.3), so the exclusion of those decay daughters from CME observables should not make any big difference.

In one event, the numbers of left-handed and right-handed Λ (or $\bar{\Lambda}$), N_L and N_R, can be different due to the topological charge fluctuaions, but the event averages, $\langle N_L \rangle$ and $\langle N_R \rangle$, should be equivalent, because, as mentioned before, the fluctuations are totally random from event to event. However, Fig. 5.10 shows $\langle N_L^{\rm obs}(\Lambda)\rangle \gg \langle N_R^{\rm obs}(\Lambda)\rangle$ and $\langle N_L^{\rm obs}(\bar{\Lambda})\rangle \ll \langle N_R^{\rm obs}(\bar{\Lambda})\rangle$. This asymmetric measurement comes from a detector effect called "Lambda efficiency" [59, 77]. On one hand, handedness results in very different daughter pion p_T. On the other hand, STAR TPC detector efficiency has a strong p_T dependence at low p_T–an efficiency dropping at low p_T. Thus, detection efficiencies are very different for left- and right-handed Λ ($\bar{\Lambda}$). Figure 5.11 shows the low and high efficiency cases for the decay

$\Lambda \to p + \pi^-$. If the decay daughter π^-'s momentum in the Λ-rest frame is opposite to the decay parent Λ's momentum in the lab frame (observed right-handed, cf. Eq. 5.8), then, after Lorentz boost, the momentum of that π^- in the lab frame would be relatively small, so it would be relatively hard for the TPC to detect that π^-, which means low efficiency. On the contrary, if the decay daughter π^- is in the same direction to the decay parent Λ (observed left-handed, cf. Eq. 5.8), the detector efficiency would be relatively high. As we also use the decay daughter proton's momentum in the Λ ($\bar{\Lambda}$)-rest frame to estimate the Λ ($\bar{\Lambda}$) handedness, more left(right)-handed Λ ($\bar{\Lambda}$) decays are measured by TPC due to this detector effect.

This detector effect causing $\langle N_L \rangle \neq \langle N_R \rangle$ should not affect the physics correlations between Δn^{obs} and Δa_1. This effect is not physical and should only contribute an uncorrelated pedestal to Δn^{obs}, which should be automatically subtracted by the definition of covariance used to quantify the correlations.

5.7 Λ and $\bar{\Lambda}$ Global Polarization

The geometry of Λ polarization is described by Fig. 5.12 (which is the Figure 1 of Ref. [1]). The polarization of $\Lambda/\bar{\Lambda}$ can be measured from its decay daughter protons:

$$\begin{aligned} P_\Lambda &= -\frac{8}{\pi \alpha_\Lambda} \langle \sin(\phi_p^* - \Psi_{\mathrm{RP}}) \rangle = -\frac{8}{\pi \alpha_\Lambda R_{11}} \langle \sin(\phi_p^* - \Psi_1) \rangle, \\ P_{\bar{\Lambda}} &= -\frac{8}{\pi \alpha_{\bar{\Lambda}}} \langle \sin(\phi_{\bar{p}}^* - \Psi_{\mathrm{RP}}) \rangle = -\frac{8}{\pi \alpha_{\bar{\Lambda}} R_{11}} \langle \sin(\phi_{\bar{p}}^* - \Psi_1) \rangle, \end{aligned} \tag{5.10}$$

where ϕ_p^* ($\phi_{\bar{p}}^*$) is the decay daughter proton (anti-proton)'s momentum azimuthal angle in the rest frame of the decay parent Λ ($\bar{\Lambda}$). In another word, ϕ_p^* ($\phi_{\bar{p}}^*$) is the azimuthal angle of $\vec{p}_p^*$ ($\vec{p}_{\bar{p}}^*$) in Eq. 5.8. Since the reaction plane (RP) is unknown in real data, in this analysis, we use EPD to measure the first-order event plane Ψ_1 as an estimate. The corresponding resolution (R_{11}, Fig. 5.6) needs to be divided out. The decay parameters (α_Λ, $\alpha_{\bar{\Lambda}}$) come from Ref. [45]:

$$\alpha_\Lambda = -\alpha_{\bar{\Lambda}} = 0.732 \pm 0.014. \tag{5.11}$$

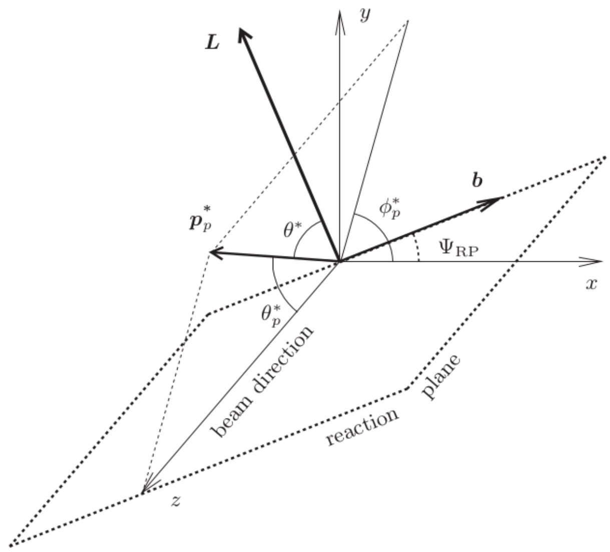

FIG. 1. Diagram showing the notations for the different angles adopted in this paper. The laboratory frame is defined by the x, y, and z (beam direction) axes. $\boldsymbol{p}_p^*$ is the hyperon decay baryon three-momentum in the hyperon rest frame. The reaction plane is spanned by the impact parameter $\boldsymbol{b}$ and the beam direction. The normal to the reaction plane defines the direction of the system orbital momentum $\boldsymbol{L}$. Reversal of the orbital momentum, $\boldsymbol{L} \rightarrow -\boldsymbol{L}$, corresponds to changing the reaction plane angle by $\Psi_{\mathrm{RP}} \rightarrow \Psi_{\mathrm{RP}} + \pi$.

Figure 5.12. The geometry of Λ polarization (Fig. 1 of Ref. [1]).

Although the measurement result of $-\alpha_{\bar{\Lambda}}$ is slightly different from α_Λ, the decay parameter magnitudes ($|\alpha_\Lambda|$, $|\alpha_{\bar{\Lambda}}|$) are still taken as the same, because there is no specific physics reason indicating any difference between them.

Since the calculations for Λ and $\bar{\Lambda}$ follow the same procedure, the following discussion will only take Λ as an example. Before any correction, we can get the term $\langle \sin(\Psi_1 - \phi_p^*) \rangle$ depending on centrality in both the Λ mass peak region and the off-peak background region. Then, we can do the purity correction [78]

$$\langle \sin(\Psi_1 - \phi_p^*) \rangle = \frac{S+B}{S} \langle \sin(\Psi_1 - \phi_p^*) \rangle_{\text{peak}} - \frac{B}{S} \langle \sin(\Psi_1 - \phi_p^*) \rangle_{\text{off-peak}}, \tag{5.12}$$

where the signal over background ratio (S/B) has been shown in Fig. 5.7.

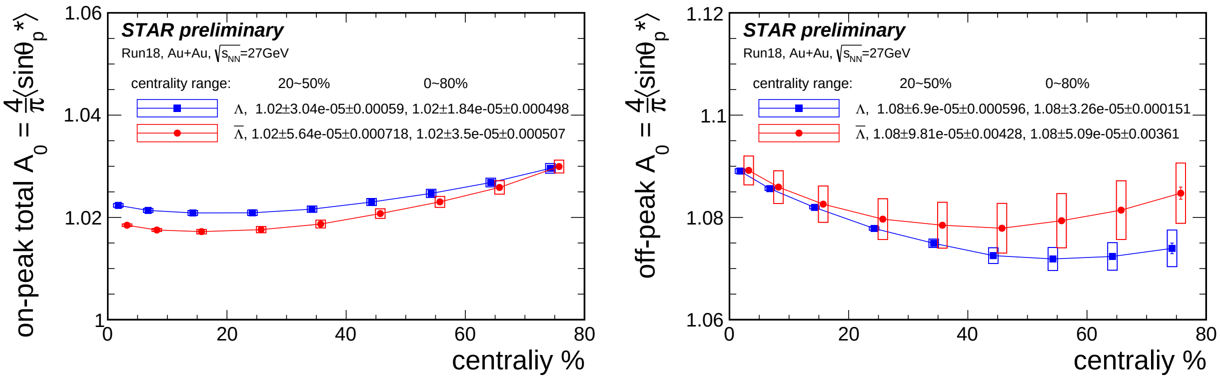

Figure 5.13. Acceptance A_0 for on-peak total Λ ($\bar{\Lambda}$) candidates (left), and for off-peak background Λ ($\bar{\Lambda}$) (right).

As suggested by Ref. [78], the polarizations need to be further corrected by acceptance

$$A_0 = \frac{4}{\pi}\langle \sin\theta_p^* \rangle, \tag{5.13}$$

where θ_p^* is the decay daughter proton's momentum polar angle in the rest frame of the decay parent Λ. Then, the correction should be done by a division

$$\begin{aligned} &\langle \sin(\Psi_1 - \phi_p^*)\rangle_{\text{peak}} \to \langle \sin(\Psi_1 - \phi_p^*)\rangle_{\text{peak}}/A_{0,\text{peak}}, \\ &\langle \sin(\Psi_1 - \phi_p^*)\rangle_{\text{off-peak}} \to \langle \sin(\Psi_1 - \phi_p^*)\rangle_{\text{off-peak}}/A_{0,\text{off-peak}}. \end{aligned} \tag{5.14}$$

As shown by Fig. 5.13 (left), we calculate the acceptance factor A_0 from the total on-peak candidates, which is very close to unity, only deviating by $2 \sim 3\%$. We also calculate A_0 for off-peak backgrounds, which is also quite close to unity.

5.8 Charge Separation Δa_1 of Unidentified Charged Hadrons

The azimuthal distribution of particles in each event can be expanded into Fourier series:

$$\frac{1}{N^{\pm}}\frac{\mathrm{d}N^{\pm}}{\mathrm{d}\phi} = \frac{1}{2\pi}\left[1 + 2a_1^{\pm}\sin(\phi - \Psi_{\text{RP}}) + \sum_{n=1}^{+\infty} 2v_n \cos n(\phi - \Psi_{\text{RP}})\right]. \tag{5.15}$$

In each event, the CME coefficients $a_1^{\pm}$ and Δa_1 could be calculated from unidentified charged hadrons as follows:

$$
\begin{aligned}
a_1^{+} =& \langle \sin(\phi^{+} - \Psi_{\mathrm{RP}}) \rangle = \langle \sin(\phi_{+} - \Psi_1) \rangle / R_{11}, \\
a_1^{-} =& \langle \sin(\phi^{-} - \Psi_{\mathrm{RP}}) \rangle = \langle \sin(\phi_{-} - \Psi_1) \rangle / R_{11},
\end{aligned}
\tag{5.16}
$$

$$
\Delta a_1 = a_1^{+} - a_1^{-}\,, \tag{5.17}
$$

where the superscripts "$\pm$" indicate the charge sign of the particle. The reaction plane (RP) cannot be directly obtained from the real data, so we use the EPD first-order event plane Ψ_1 to estimate Ψ_{RP}, and the corresponding resolution R_{11} is divided out (cf. Sec. 5.4). As a parity-odd observable, Δa_1 (also a_1^{+}, a_1^{-}) averages to zero because of random topological charge (Q_w) fluctuations from event to event (also discussed in Sec. 1.4).

To focus on the primordial particles, we set the distance of the closest approach to the collision primary vertex (gDca) smaller than 1 cm (gDca $<$ 1 cm as the default, and gDca $< 0.8, 2.0$ cm as systematical variations, cf. Sec. 5.2) and remove the decay daughters from Λ ($\bar{\Lambda}$). When forming correlation with on-peak Λ ($\bar{\Lambda}$) handedness (Δn^{obs}), Δa_1 is calculated without the decay daughters from Λ ($\bar{\Lambda}$) candidates from the peak region. When forming correlation with off-peak "Λ ($\bar{\Lambda}$)", Δa_1 is calculated without the decay daughters from "Λ ($\bar{\Lambda}$) candidates" from the off-peak region.

5.9 Correlator $\Delta\gamma$ of Unidentified Charged Hadrons

A CME-sensitive EP-dependent correlator $\Delta\gamma$ ($\equiv \gamma_{\mathrm{OS}} - \gamma_{\mathrm{SS}}$) [23] is widely used in CME studies. Similar as Δa_1, the unidentified charged hadrons are used to calculate this $\Delta\gamma$ correlator. The definitions of γ_{OS} and γ_{SS} are as follows:

$$
\begin{aligned}
\gamma_{\mathrm{OS}} =& \langle \cos(\phi_{\alpha}^{\pm} + \phi_{\beta}^{\mp} - 2\Psi_{\mathrm{RP}}) \rangle = \langle \cos(\phi_{\alpha}^{\pm} + \phi_{\beta}^{\mp} - 2\Psi_2) / R_{21}, \\
\gamma_{\mathrm{SS}} =& \langle \cos(\phi_{\alpha}^{\pm} + \phi_{\beta}^{\pm} - 2\Psi_{\mathrm{RP}}) \rangle = \langle \cos(\phi_{\alpha}^{\pm} + \phi_{\beta}^{\pm} - 2\Psi_2) / R_{21},
\end{aligned}
\tag{5.18}
$$

where the subscripts α and β denote two different (primordial) particles in the same event. If the two particles have the opposite sign (OS), we call it γ_{OS}. If the two particles have the same sign (SS), we call it γ_{SS}. Since the reaction plane (RP) cannot be directly obtained from the real data, we use the EPD second-order event plane Ψ_2 to estimate Ψ_{RP}, and the corresponding resolution R_{21} is divided out (cf. Sec. 5.4). To subtract the charge-independent background contributions (e.g., momentum conservation, inter-jet correlation, ...), we take the difference

$$\Delta\gamma = \gamma_{\mathrm{OS}} - \gamma_{\mathrm{SS}}. \tag{5.19}$$

The CME signal can contribute to a positive $\Delta\gamma$ value, while some backgrounds can also contribute in this way [23, 35, 36, 37, 38, 39, 40].

Similar to Δa_1, $\Delta\gamma$ needs to be calculated from the primordial particles, so the same gDca cuts are applied and the decay daughters from Λ ($\bar{\Lambda}$) are removed. When forming correlation with on-peak Λ ($\bar{\Lambda}$) polarizations (P_{Λ}, $P_{\bar{\Lambda}}$, ΔP), $\Delta\gamma$ calculation excludes the decay daughters from $\Lambda/\bar{\Lambda}$ candidates from the peak region. When forming correlation with off-peak "Λ ($\bar{\Lambda}$) polarizations" ("P_{Λ}", "$P_{\bar{\Lambda}}$", "ΔP"), $\Delta\gamma$ calculation excludes the decay daughters from "Λ ($\bar{\Lambda}$) candidates" from the off-peak region.

6. RESULTS

This chapter first shows the individual measurements of the Λ ($\bar{\Lambda}$) quantities (P, Δn^{obs}), and the CME observables (Δa_1, $\Delta\gamma$). Since the individual correlations are event averages, the parity-odd observable Δa_1 vanishes to zero as expected, whereas Δn^{obs} can be non-zero due to a large unphysical detector effect. The parity-even observables ($\Delta\gamma$, P_Λ, $P_{\bar{\Lambda}}$) are nontrivial and are well studied in STAR. The cross checks indicate that our results are consistent with others. The polarization difference $\Delta P = P_\Lambda - P_{\bar{\Lambda}}$ shows nothing beyond statistical uncertainty, which is also the conclusion of other STAR measurements of this dataset and other datasets.

Then, the covariances are used to quantify the correlations between the observables ΔP–$\Delta\gamma$ and Δn^{obs}–Δa_1. In this exploratory study, all those correlations are consistent with zero.

6.1 Λ and $\bar{\Lambda}$ Handedness Imbalance Measurement Δn

In Sec. 5.6, we have already defined the observed handedness of Λ ($\bar{\Lambda}$) and the event-average numbers of left-/right-handed Λ ($\bar{\Lambda}$) N^{obs} (cf. Fig. 5.10). The normalized handedness imbalance Δn^{obs} is defined by Eq. 5.9, where, similar to N^{obs}, the superscript "obs" means "observed".

The individual measurement of Δn^{obs} is an event average:

$$\langle \Delta n^{\text{obs}} \rangle = \left\langle \frac{N_L^{\text{obs}} - N_R^{\text{obs}}}{\langle N_L^{\text{obs}} + N_R^{\text{obs}} \rangle} \right\rangle = \frac{\langle N_L^{\text{obs}} - N_R^{\text{obs}} \rangle}{\langle N_L^{\text{obs}} + N_R^{\text{obs}} \rangle} = \frac{\langle N_L^{\text{obs}} \rangle - \langle N_R^{\text{obs}} \rangle}{\langle N_L^{\text{obs}} \rangle + \langle N_R^{\text{obs}} \rangle}. \tag{6.1}$$

Therefore, it can be directly calculated from $\langle N^{\text{obs}} \rangle$ in Fig. 5.10. Figure 6.1 shows the individual handedness imbalance measurements for Λ (a), $\bar{\Lambda}$ (b), and their sum (c).

As discussed in Sec. 5.6, the "Lambda efficiency" detector effect makes $\langle N_L^{\text{obs}}(\Lambda) \rangle \gg \langle N_R^{\text{obs}}(\Lambda) \rangle$ and $\langle N_L^{\text{obs}}(\bar{\Lambda}) \rangle \ll \langle N_R^{\text{obs}}(\bar{\Lambda}) \rangle$, rendering $\Delta n^{\text{obs}}(\Lambda) > 0$ and $\Delta n^{\text{obs}}(\bar{\Lambda}) < 0$. Since more Λ hyperons are measured/reconstructed than $\bar{\Lambda}$ due to baryon stopping effect, the inclusive handedness imbalance $\Delta n^{\text{obs}}(\Lambda + \bar{\Lambda}) > 0$.

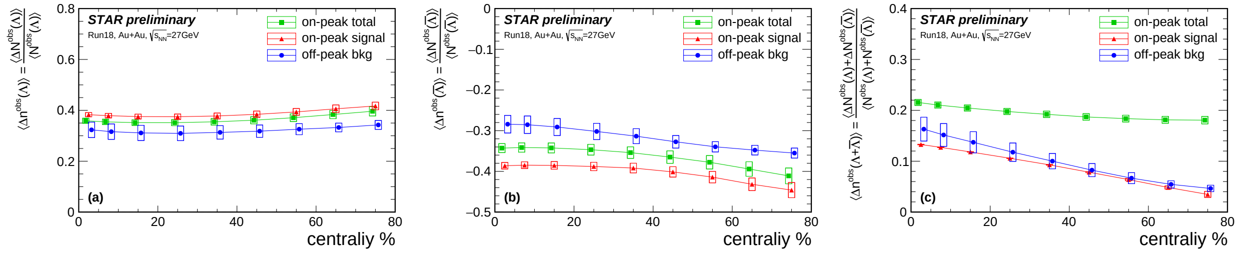

Figure 6.1. Observed handedness imbalance Δn^{obs} for Λ (left), $\bar{\Lambda}$ (middle), and their sum (right) as functions of centrality. Need to note here that the data are not corrected for the acceptance effect.

6.2 Λ and $\bar{\Lambda}$ Global Polarization Measurement P_Λ, $P_{\bar{\Lambda}}$, ΔP

The method to measure Λ ($\bar{\Lambda}$) global polarization is discussed in Sec. 5.7. After the purity, Ψ_1 resolution, and A_0 acceptance corrections, we can get the polarization of Λ and $\bar{\Lambda}$ as functions of centrality in Fig. 6.2. Both Λ and $\bar{\Lambda}$ have positive polarization ($P_\Lambda, P_{\bar{\Lambda}}$) of value ~ 0.01 with good significance, and show increasing trend from central to peripheral collisions (centrality 0 to 80%). However, the polarization difference between Λ and $\bar{\Lambda}$, ΔP, is consistent with zero from this analysis (Fig. 6.2(c)), which has been also seen by other STAR analysis on this dataset and other datasets.

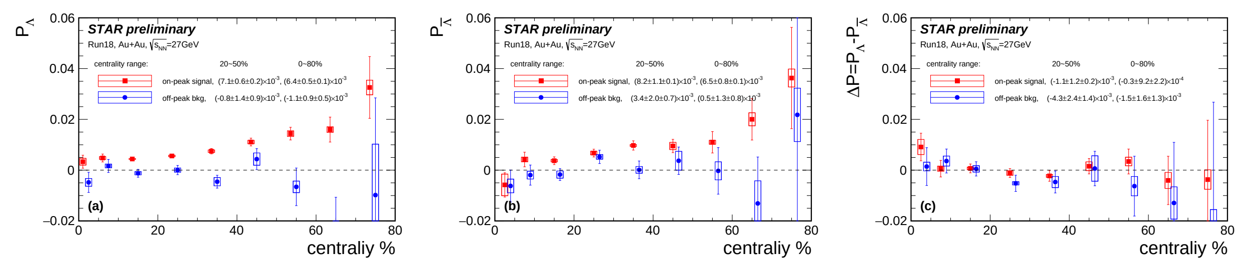

Figure 6.2. Λ (left) and $\bar{\Lambda}$ (middle) global polarizations and their difference (right) as functions of centrality in Au+Au collisions at $\sqrt{s_{\mathrm{NN}}} = 27$ GeV (Run18). The track quality cuts are listed in Sec. 5.2. Error bars are statistical uncertainties and boxes are systematic uncertainties. Lambda efficiency corrections are not applied.

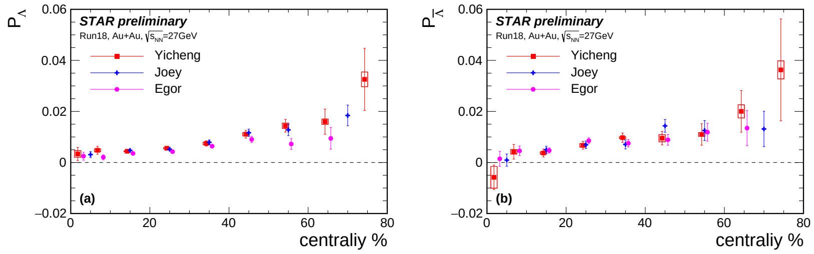

Figure 6.3. Λ ($\bar{\Lambda}$) polarization comparison between this study and Joey's and Egor's studies

For this same dataset, the Λ ($\bar{\Lambda}$) polarizations in this dataset have also been measured by other groups in STAR. The cross checks in Fig. 6.3 show our results consistent with Joseph Adams's [2] and Egor Alpatov's measurements.

6.3 Charge Separation Δa_1 of Unidentified Charged Hadrons

Figure 6.4 shows a_1^+, a_1^-, and Δa_1 as functions of centrality, whose definitions are shown in Sec. 5.8. The calculations use unidentified charged hadrons with selections $-1 \le \eta \le 1$, 0.2 GeV $\le p_T \le$ 2.0 GeV, nHitsFit $\ge$ 15 $(10, 20)$, $0.52 \le \frac{\text{nHitsFit}}{\text{nHitsMax}} \le 1.05$, and gDca $<$ 1.0 $(0.8, 2.0)$ cm (cf. Sec. 5.2), where the gDca cut selects primordial particles. To avoid

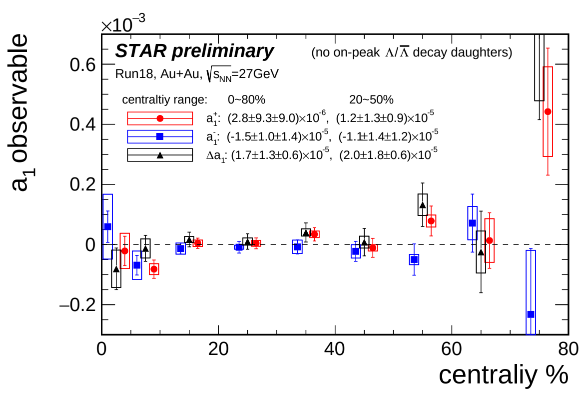

Figure 6.4. The a_1 observables (a_1^+, a_1^-, Δa_1) as functions of centrality in Au+Au collisions at $\sqrt{s_{\rm NN}}$ = 27 GeV. The unidentified charged hadrons are used with the track quality cuts listed in Sec. 5.2. Hadrons used to reconstruct Λ or $\bar{\Lambda}$ in the mass peak region are excluded.

possible self-correlation, the particles are excluded from calculation if they are used to reconstruct on-peak Λ ($\bar{\Lambda}$) candidates. Since the reconstructed Λ ($\bar{\Lambda}$) numbers (cf. Fig. 5.10) are much smaller than the multiplicity (cf. Fig. 3.3), this exclusion should not make any big difference.

Both the markers and the average values show that all those observables are consistent with zero, as expected by the totally random topological charge fluctuations from event to event. This also shows why the individual measurements of parity-odd observables are trivial and vanish to zero.

6.4 Correlator $\Delta\gamma$ of Unidentified Charged Hadrons

Figure 6.5 shows γ_{OS}, γ_{SS}, and $\Delta\gamma$ as functions of centrality, whose definitions are shown in Sec. 5.9. Similar to Δa_1, the particles used are unidentified charged hadrons with requirements $-1 \leq \eta \leq 1$, 0.2 GeV $\leq p_T \leq$ 2.0 GeV, nHitsFit ≥ 15 $(10, 20)$, $0.52 \leq \frac{\text{nHitsFit}}{\text{nHitsMax}} \leq 1.05$, gDca < 1.0 $(0.8, 2.0)$ cm (cf. Sec. 5.2), and the particles are excluded if they used to reconstruct on-peak Λ ($\bar{\Lambda}$) candidates.

For this same dataset Run18 Au+Au $\sqrt{s_{\mathrm{NN}}} = 27$ GeV, BNL-Fudan group has an analysis including $\Delta\gamma$. As a consistency check, the $\Delta\gamma$ results of their study and this study are plotted

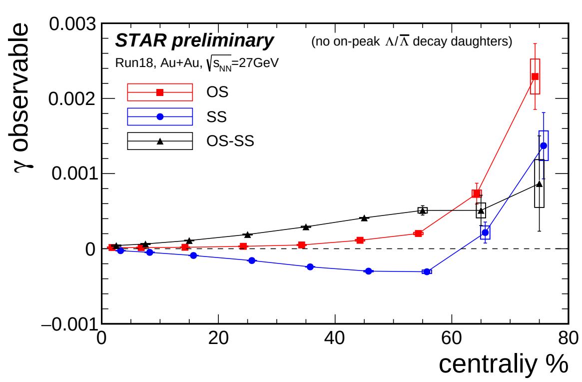

Figure 6.5. γ observables (γ_{OS}, γ_{SS}, $\Delta\gamma$) as functions of centrality in Au+Au collisions at $\sqrt{s_{\mathrm{NN}}} = 27$ GeV. The unidentified charged hadrons are used with the track quality cuts listed in Sec. 5.2. Hadrons used to reconstruct Λ or $\bar{\Lambda}$ in the mass peak region are excluded.

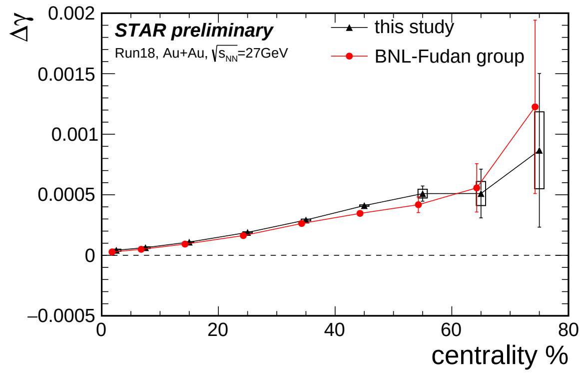

Figure 6.6. $\Delta\gamma$ comparison between this study (black) and BNL-Fudan's study (red). The two results are consistent with each other.

together for easy comparison (Fig. 6.6). The two studies have $\Delta\gamma$ results consistent with each other in both values and error bars (agreed by Yu Hu, Prithwish Tribedy, and myself). The minor difference could come from the different cuts. For example, BNL-Fudan's analysis uses gDca < 3 cm, and does not cut on nHitsFit/nHitsMax.

6.5 Correlation Measurements Between Δn and Δa_1

In this section, we present correlation measurements. In order to quantify event-by-event correlations, we calculate covariances. The covariance between observables X and Y is defined as

$$\mathrm{Cov}[X, Y] = \langle XY \rangle - \langle X \rangle \langle Y \rangle \,, \tag{6.2}$$

where $\langle \cdot \rangle$ means the event average in this analysis. For each event, we can get one measurement for X, one for Y, and therefore one for XY. Then, we go through all events (for each centrality respectively) to get the averages $\langle X \rangle$, $\langle Y \rangle$, and $\langle XY \rangle$, from which the covariance can be calculated. The $\langle X \rangle$, $\langle Y \rangle$ corresponds to the individual measurements, whose product $\langle X \rangle \langle Y \rangle$ is the pedestal subtracted in Eq. 6.2. By this means, the detector effects like Lambda efficiency (cf. Sec. 5.6) are automatically cancelled.

As mentioned in the Introduction (Chapter 1), the physical vacuum is complex. QCD vacuum fluctuations cause nonzero topological charge in a local domain. Here, without loss

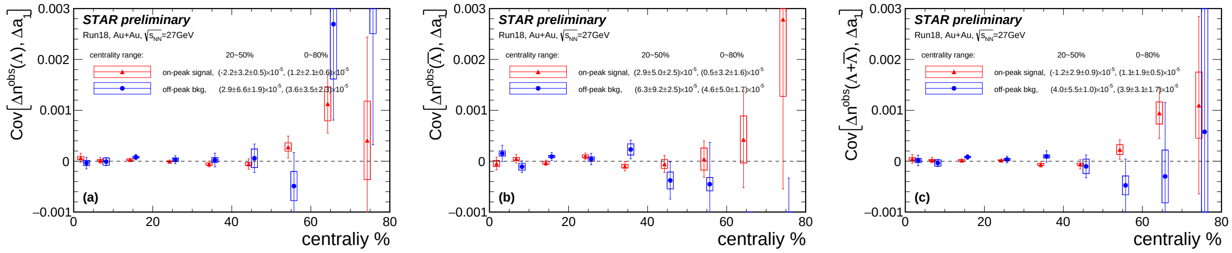

Figure 6.7. The covariance between Δa_1 and Δn^{obs} for Λ (left), $\bar{\Lambda}$ (right), and their sum (right) as functions of centrality in Au+Au collisions at $\sqrt{s_{\mathrm{NN}}}$ = 27 GeV (Run18). The track cuts are listed in Sec. 5.2. Hadrons used to reconstruct Λ or $\bar{\Lambda}$ in the mass peak region are excluded from Δa_1.

of generality, we take the negative topological charge ($Q_w < 0$) for example (cf. Fig. 1.3). In that local domain, the chirality anomaly results in different numbers of left- and right-handed quarks. This difference in this analysis is characterized by Δn. On one hand, Δn of s quark is less than zero due to negative topological charge. Since Λ hyperon contains s quark, Δn of Λ is also less than zero. On the other hand, u and d quarks also have the same preference for handedness. If meanwhile there is a strong magnetic field, created by the spectator protons in heavy-ion collisions, the postive and negative charges will have spins in the opposite directions. As a result, their momentum would also be opposite. We use Δa_1 and $\Delta\gamma$ to characterize this kind of charge separation. Provided the relationship between the magnetic field and the measured Ψ_1 in STAR experiment (cf. Fig. 1.2), the negative topological charge causes positive Δa_1. As a result, the Δn and Δa_1 are expected to be negatively correlated.

Figure 6.7 shows the observed correlation between Δa_1 and Δn^{obs} in each centrality bin. Both the signal and background are consistent with zero with the current uncertainties.

6.6 Correlation Measurements Between ΔP and $\Delta\gamma$

In heavy-ion collisions, the participants contribute to the nonzero total angular momentum, which affects the whole system. The global angular momentum should roughly align with the magnetic field. The vorticity can cause global polarization preference with respect to the impact parameter [1, 2], equally on Λ and $\bar{\Lambda}$. Meanwhile, the magnetic field

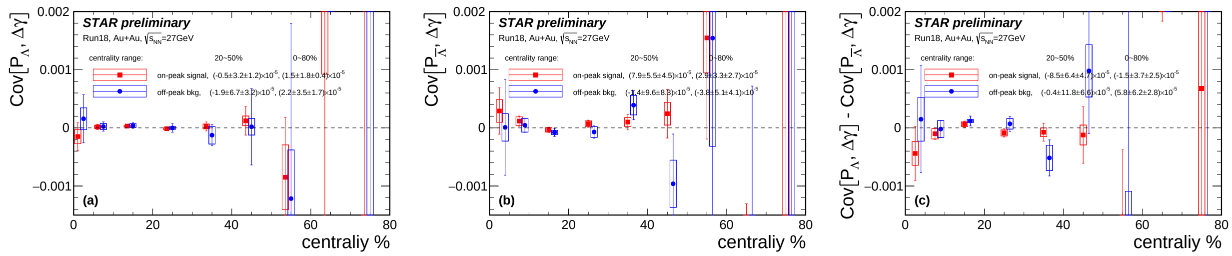

Figure 6.8. Covariance between the parity-even observables, (left) P_Λ and $\Delta\gamma$, (middle) $P_{\bar{\Lambda}}$ and $\Delta\gamma$, and (right) and their difference as functions of centrality in Au+Au collisions at $\sqrt{s_{\rm NN}} = 27$ GeV (Run18). The track cuts are listed in Sec. 5.2. Hadrons used to reconstruct Λ or $\bar{\Lambda}$ in the mass peak region are excluded from $\Delta\gamma$.

can enhance the polarization of $\bar{\Lambda}$ and reduce that of Λ. As a result, it was proposed to probe the magnetic field by measuring the polarization difference between Λ (P_Λ) and $\bar{\Lambda}$ ($P_{\bar{\Lambda}}$), $\Delta P = P_\Lambda - P_{\bar{\Lambda}}$, where $\Delta P < 0$ is expected for the signal of magnetic field existence (cf. Fig. 1.3). However, the current results for ΔP are still inconclusive (cf. Sec. 6.2). On the other hand, that magnetic field in the same event is a key factor to cause the CME, while the CME signal contributes to a positive $\Delta\gamma$. Therefore, the possible signal makes ΔP and $\Delta\gamma$ negatively correlated.

To gain statistics, we calculate the event-by-event covariance between P_Λ and $\Delta\gamma$, and between $P_{\bar{\Lambda}}$ and $\Delta\gamma$ separately. The self-correlation is removed as mentioned before. Then, we can take the difference $\mathrm{Cov}[P_\Lambda, \Delta\gamma] - \mathrm{Cov}[P_{\bar{\Lambda}}, \Delta\gamma]$. We need to note that the two covariances are not necessarily using the same events, because some events may only have Λ ($\bar{\Lambda}$) and no $\bar{\Lambda}$ (Λ), which is counted in $\mathrm{Cov}[P_\Lambda, \Delta\gamma]$ ($\mathrm{Cov}[P_{\bar{\Lambda}}, \Delta\gamma]$) but not in the other term.

Figure 6.8 shows the observed correlation between $\Delta\gamma$ and polarizations (P_Λ, $P_{\bar{\Lambda}}$, and ΔP) as functions of centrality. With the current statistics, both the signal and background are consistent with zero.

7. SUMMARY

The purpose of this study is to search for evidence of the magnetic field created by spectator protons in heavy ion collisions and the chiral magnetic effect (CME) arising from vacuum topological charge fluctuations acted under this magnetic field. Two Λ ($\bar{\Lambda}$) hyperon observables (ΔP, Δn^{obs}) and two CME observables (Δa_1, $\Delta\gamma$) are used in this study, where ΔP and $\Delta\gamma$ are parity-even; Δn^{obs} and Δa_1 are parity-odd.

The global polarization of Λ and $\bar{\Lambda}$ are well measured respectively. However, the polarization difference between Λ and $\bar{\Lambda}$ has large statistical uncertainty and is presently consistent with zero for all analyzed datasets, including the one used for this study. The correlator $\Delta\gamma$ is widely used to search for the CME at RHIC and at the LHC. Although positive $\Delta\gamma$ values have been observed in many of those measurments, the large background contaminations render no firm conclusion on the CME signal. Many background removal attempts have been exercised with so far limited success. As for the parity-odd observables (Δn^{obs}, Δa_1), their event averages are by definition trivial because of the event-by-event random fluctuations of the topological charges.

To gain further insights, the event-by-event correlations between those observables are proposed to detect the CME and the magnetic field, as they are affected by the same physical source in the event. We have carried out such a correlation study in this thesis. We conduct a thorough analysis, including data quality assurance (QA), TPC efficiency correction, EPD event plane reconstruction, Λ ($\bar{\Lambda}$) reconstructions, etc. We then measure the event average of each quantity individually as functions of centrality, which, as expected, are not enough to draw conclusion on the CME or magnetic field. The results are consistent with previous and on-going analyses of the same data sample in STAR. Finally, we report an exploratory measurement of event-by-event correlations between Δn^{obs} and Δa_1, and between ΔP and $\Delta\gamma$, by the STAR experiment in Au+Au collisions at $\sqrt{s_{\mathrm{NN}}} = 27$ GeV. Our results, with the current dataset, show that both correlations are consistent with zero signal. Future endeavor of this analysis is to exact an upper limit of the correlation signal. The correlation analysis can be applied to other and future data samples.

8. OTHER STUDIES

During my PhD project, I attended many studies as one of the principal authors. In this chapter, I will briefly go through those studies, where some have been finished and others are still on-going. The flow chart below shows all the studies I took part in, whose common physics topic is the chiral magnet effect (cf. Sec. 1.4).

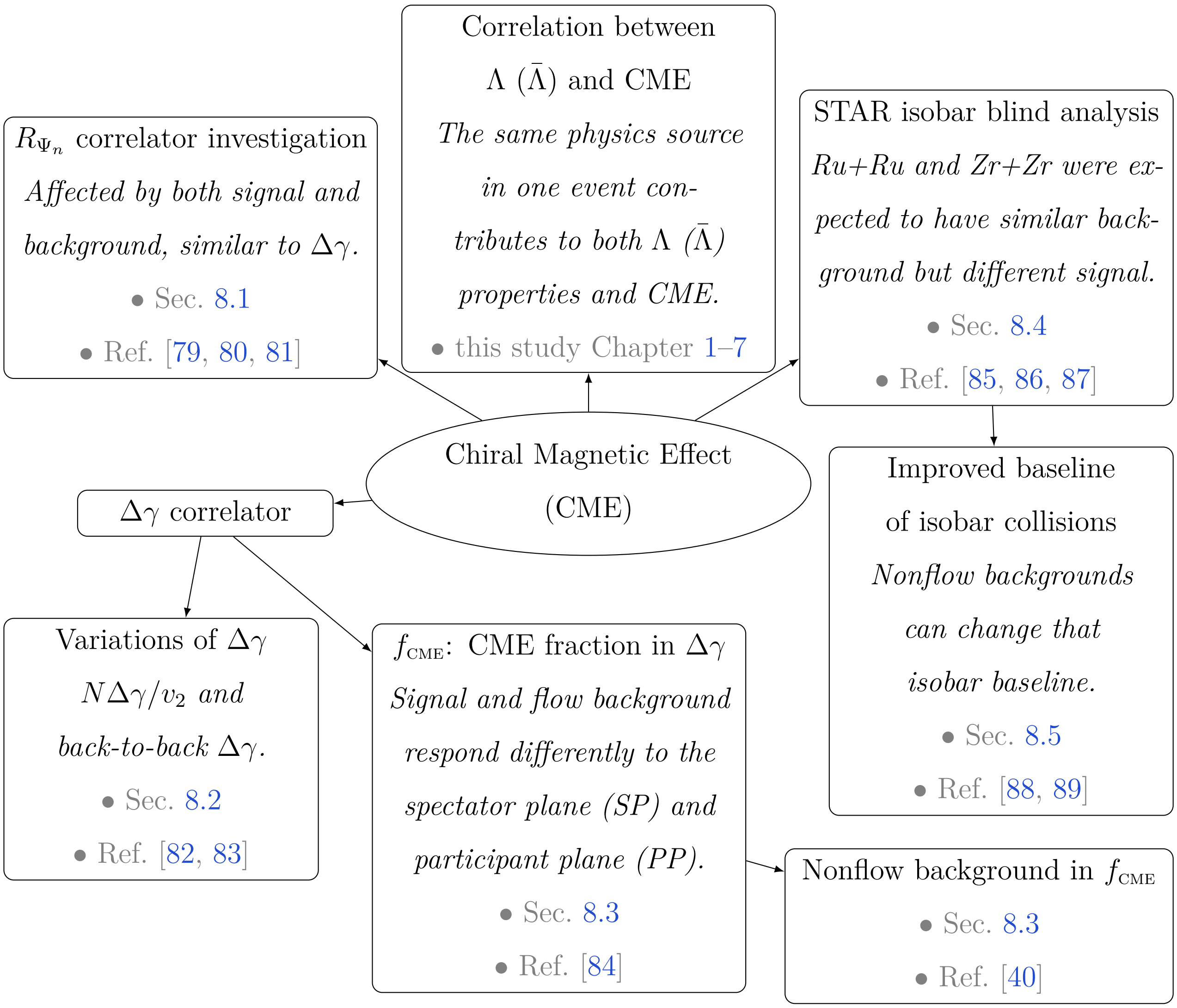

8.1 Investigation of the R_{Ψ_m} Correlators

Publications:

- **Yicheng Feng**, Jie Zhao, and Fuqiang Wang, *Responses of the chiral-magnetic-effect–sensitive sine observable to resonance backgrounds in heavy-ion collisions*, Phys. Rev. C **98**, 034904 (2018), doi:10.1103/PhysRevC.98.034904, arXiv:1803.02860 [nucl-th]. [79]

- **Yicheng Feng**, Fuqiang Wang, and Jie Zhao, *Comment on "A sensitivity study of the primary correlators used to characterize chiral-magnetically-driven charge separation" by Magdy, Nie, Ma, and Lacey*, arXiv:2009.10057 [nucl-ex] (2020). [80]

- **Yicheng Feng**, Jie Zhao, Hao-jie Xu, and Fuqiang Wang, *Decipher the R_{Ψ_m} correlator in search for the chiral magnetic effect in relativistic heavy ion collisions*, Phys. Rev. C **103**, 034912 (2021), doi:10.1103/PhysRevC.103.034912 arXiv:2011.01123 [nucl-th]. [81]

R_{Ψ_m} $(m = 2, 3)$ is an azimuthal correlator proposed to measure the CME [90, 91]. To understand this observable, we first perform analytical calculations and toy model simulations [79]. We find R_{Ψ_2} has obvious dependences on POI p_T, v_2, and resonance v_2, indicating R_{Ψ_2} is contaminated by background. We also find that R_{Ψ_3} is ill-defined, because it does not preserve the periodicity $\phi \to \phi + 2\pi$; its numerical value depends on the choice of the ϕ angle range.

Later, the authors of the R_{Ψ_m} correlators use A Multi-Phase Transport (AMPT) model [92, 93] with input CME signal to study the sensitivity of R_{Ψ_m} and $f_{\text{CME}} = \Delta\gamma_{\text{CME}}/\Delta\gamma$ correlators to CME [94]. They claim that f_{CME} is insensitive to small CME signal, which we think is moot because there are some obvious mistakes in their error proporgations. They also claim that their R_{Ψ_2} is more sensitive to CME and not affected by background, where, however, some data points are dropped. If added back, that datapoint shows finite background contamination at zero CME input to their model simulation. To point out those errors, we have written a comment [80] on their publication. Since Physics Letters B does not publish comments, we did not pursue further publication of our comment.

A preprint (arXiv:2006.04251v1) [95] from STAR, mainly analyzed by the authors of the R_{Ψ_m} observable, suggests that the R_{Ψ_m} observable is sensitive to the CME signal and relatively insensitive to backgrounds, and their Au+Au data are inconsistent with known background contributions, by observing the same R_{Ψ_2} and R_{Ψ_3} (convex) distributions from AMPT model and by contrasting data and model as well as large and small systems. We examine those claims by studying the robustness of the R_{Ψ_m} observable using AMPT as well as toy model simulations. We compare R_{Ψ_m} to the more widely used $\Delta\gamma$ azimuthal correlator to identify their commonalities and differences [81]. We use AMPT to simulate Au+Au, p+Au, and d+Au collisions at $\sqrt{s_{\mathrm{NN}}} = 200$ GeV, and study the responses of R_{Ψ_m} to anisotropic flow backgrounds in the model. We also use a toy model to simulate resonance flow background and input CME signal to investigate their effects in R_{Ψ_2}. Additionally we use the toy model to perform an event shape engineering (ESE) [41] analysis to compare to STAR data as well as to predict the degree of sensitivity of R_{Ψ_2} to isobar collisions with the event statistics taken at RHIC. Our AMPT results show that the R_{Ψ_2} in Au+Au collisions is concave and apparently different from R_{Ψ_3}, in contradiction to the findings in STAR's preprint, while the R_{Ψ_2} in p+Au and d+Au collisions are slightly concave. Our toy model ESE analysis indicates that the R_{Ψ_2} is sensitive to the event-by-event anisotropy q_2 as well as the elliptic flow parameter v_2. The toy model results further show that R_{Ψ_2} depends on both the CME signal and the flow backgrounds, similar to the $\Delta\gamma$ observable. It is found that the R_{Ψ_2} and $\Delta\gamma$ observables show similar sensitivities and centrality dependences in isobar collisions. We conclude that R_{Ψ_2} and the inclusive $\Delta\gamma$ are essentially the same.

In the process of our investigation, we found a coding error that effectively made the R_{Ψ_3} meaningless, even worse than ill-defined. This coding error was later also discovered, independently, by Yufu Lin [86]. There are other mistakes in the STAR preprint that are not worth going into detail. As a result, the STAR preprint has been withdrawn; see comment of arXiv:2006.04251 [95].

8.2 Back-to-Back $\Delta\gamma$ Correlator

Publications:

- Jie Zhao, **Yicheng Feng**, Hanlin Li and Fuqiang Wang, *HIJING can describe the anisotropy-scaled charge-dependent correlations at the BNL Relativistic Heavy Ion Collider*, Phys. Rev. C **101**, 034912 (2020), doi:10.1103/PhysRevC.101.034912, arXiv:1912.00299 [nucl-th]. [83]

- **Yicheng Feng**, Jie Zhao, and Fuqiang Wang, *Back-to-back relative-excess observable to identify the chiral magnetic effect*, Phys. Rev. C **101**, 014915 (2020), doi:10.1103/PhysRevC.101.014915, arXiv:1908.10210 [nucl-th]. [82]

The $\Delta\gamma$ is a widely-used CME-sensitive observable [23], whose definition w.r.t. RP (reaction plane) is given by Eq. 1.2. Studies in both large collision systems (Au+Au at RHIC [24, 25, 26, 27] and Pb+Pb at the LHC [29, 31, 32, 33, 34]) and small systems (d+Au at RHIC [28] and p+Pb at the LHC [31, 32]) have seen significantly positive $\Delta\gamma$. However, the latter (small systems) is expected to have no observable CME signal, which suggests strong background contaminations in $\Delta\gamma$ in heavy ion collisions. The backgrounds are mainly caused by two-particle (2p) nonflow correlations, such as resonance decays, coupled with elliptic flow (v_2) of the correlated pairs [23, 35, 36, 37, 38, 39].

We have studied the backgrounds in $\Delta\gamma$ by using AMPT (A Multi-Phase Transport [92, 93]) and HIJING (Heavy Ion Jet Interaction Generator [96, 97]) models [83]. Both large and small collision systems are simulated. Their $\Delta\gamma$, after proper scaling ($N\Delta\gamma/v_2$), are compared to STAR data.

Many techniques have been investigated to reduce the backgrounds, like event shape engineering [41, 30, 32, 33] and differential measurements in invariant mass [42, 43]. All those studies show that the possible CME signal is consistent with zero and the backgrounds are dominant.

One of my early studies [82] also aims to reduce the background by using analytical calculations and toy model simulations. A back-to-back requirement is applied to select particle pairs: their opening angle is required to satisfy $|\phi_\alpha - \phi_\beta| > \pi - 2\Delta$ (Δ is a parameter, which could be $\pi/12$), and they are required to come from two different subevents in η with a gap (east subevent: $-1 < \eta < -0.5$; west subevent $0.5 < \eta < 1.0$). By this means, the resonance decay contribution is significantly reduced, whereas the signal contribution is relatively unaffected. However, this method, while greatly improves signal over background ratio, cannot completely remove the background contamination coupled with v_2, and loses lots of statistics due to its selection of back-to-back pairs.

8.3 CME Fraction f_{CME} and Study of Nonflow Effect

Publications:

- **Y. Feng**, J. Zhao, H. Li, H. j. Xu and F. Wang, *Two- and three-particle nonflow contributions to the chiral magnetic effect measurement by spectator and participant planes in relativistic heavy ion collisions*, Phys. Rev. C **105**, no.2, 024913 (2022) doi:10.1103/PhysRevC.105.024913 [arXiv:2106.15595 [nucl-ex]] [40].
- M. Abdallah *et al.* [STAR], *"Search for the Chiral Magnetic Effect via Charge-Dependent Azimuthal Correlations Relative to Spectator and Participant Planes in Au+Au Collisions at $\sqrt{s_{NN}} = 200\,GeV$,"* Phys. Rev. Lett. **128**, no.9, 092301 (2022) doi:10.1103/PhysRevLett.128.092301 [arXiv:2106.09243 [nucl-ex]]. [84]

In 2017, a noval method [44, 98] was discovered to extract the CME signal from the flow-induced backgrounds by comparing $\Delta\gamma$ and v_2 with respect to the participant plane (PP, reconstructed from produced particles) and the spectator plane (SP, reconstructed from spectators), which is called the SP/PP method.

The elliptic flow v_2 is the maximum when measured w.r.t. PP; such a measurement is called $v_2\{\mathrm{PP}\}$. The v_2 measured w.r.t. SP ($v_2\{\mathrm{SP}\}$) is a projection from PP to SP by the projection factor $a \equiv \langle \cos 2(\Psi_{\mathrm{SP}} - \Psi_{\mathrm{PP}}) \rangle$ (cf. Fig. 8.1) [44, 99]. The v_2-induced backgrounds

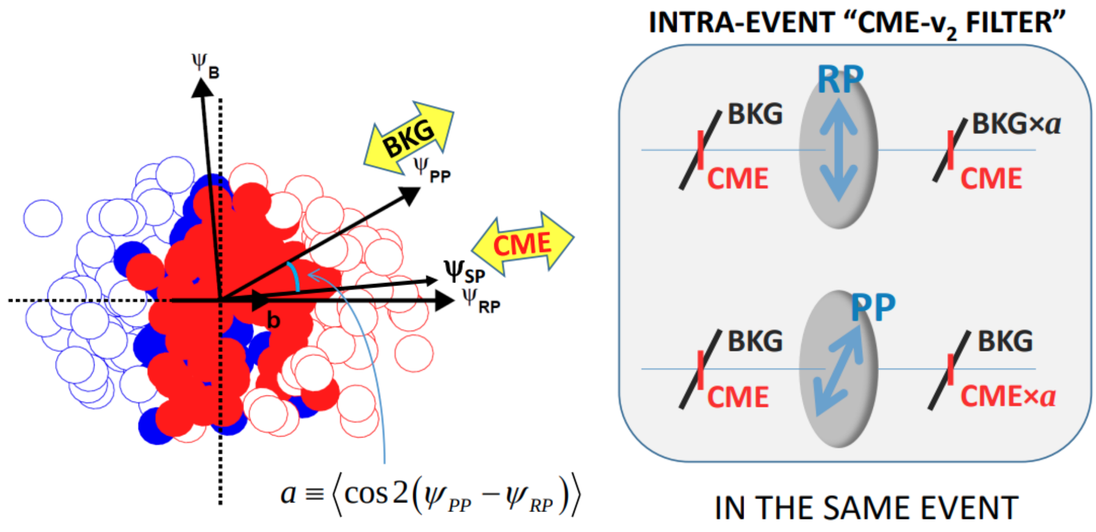

Figure 8.1. Schematic diagrams for the SP/PP method [44, 99].

in $\Delta\gamma$ follow the same relationship as v_2. On the other hand, because the CME signal is along the magnetic field created by the spectator protons, the CME signal in $\Delta\gamma$ ($\Delta\gamma_{\mathrm{CME}}$) would be the maximum when measured w.r.t. SP ($\Delta\gamma_{\mathrm{CME}}\{\mathrm{SP}\}$), and the CME signal w.r.t. PP ($\Delta\gamma_{\mathrm{CME}}\{\mathrm{PP}\}$) would be a projection from $\Delta\gamma_{\mathrm{CME}}\{\mathrm{SP}\}$. Because those measurements are in the *same* event, the geometry shows the signal projection factor is also a. After some straightforward algebra, the CME fraction in $\Delta\gamma$ is

$$f_{\mathrm{CME}} = \frac{\Delta\gamma_{\mathrm{CME}}\{\mathrm{PP}\}}{\Delta\gamma\{\mathrm{PP}\}} = \frac{A/a-1}{1/a^2-1}, \tag{8.1}$$

where

$$A = \Delta\gamma\{\mathrm{SP}\}/\Delta\gamma\{\mathrm{PP}\}. \tag{8.2}$$

Had there been no nonflow background, we think this method is very robust to extract the possible CME signal in $\Delta\gamma$. STAR collaboration has performed measurements [100, 101, 84] using this method.

In our recent study [40], we investigate the nonflow contaminations to the extracted CME signal fraction f_{CME}. The nonflow can be divided into several components according to their physics and contributions to the observables. The two-particle correlator $v_2^{*2} = \langle \cos 2\Delta\phi \rangle$ measurements include nonflow:

$$\begin{aligned} v_2^{*2} =& v_2^2 + v_{2,\mathrm{nf}}^2, \\ \epsilon_{\mathrm{nf}} \equiv& v_{2,\mathrm{nf}}^2 / v_2^2, \end{aligned} \tag{8.3}$$

where $\Delta\phi$ is the azimuthal angle difference of the two particles in the pair. The three-particle correlator C_3 is defined as follows:

$$\begin{aligned} C_{3,\mathrm{OS}} =& \langle \cos(\phi_\alpha^\pm + \phi_\beta^\mp - 2\phi_c) \rangle, \\ C_{3,\mathrm{SS}} =& \langle \cos(\phi_\alpha^\pm + \phi_\beta^\pm - 2\phi_c) \rangle, \\ C_3 =& C_{3,\mathrm{OS}} - C_{3,\mathrm{SS}}. \end{aligned} \tag{8.4}$$

C_3 is composed of flow-induced background (major), 3-particle nonflow correlations (minor), and possible CME (not written out) [40]:

$$C_3 = \frac{C_{2\mathrm{p}} N_{2\mathrm{p}}}{N^2} v_{2,2\mathrm{p}} v_2 + \frac{C_{3\mathrm{p}} N_{3\mathrm{p}}}{2N^3} = \frac{v_2^2 \epsilon_2}{N} + \frac{\epsilon_3}{N^2}, \tag{8.5}$$

where

- 2-particle (2p) nonflow (e.g., resonance, ...) $C_{2\mathrm{p}} \equiv \langle \cos(\phi_\alpha + \phi_\beta - 2\phi_{2\mathrm{p}}) \rangle$, where $\phi_{2\mathrm{p}}$ is the azimuth of the 2p cluster;
- 3-particle (3p) nonflow (e.g., jets, ...) $C_{3\mathrm{p}} \equiv \langle \cos(\phi_\alpha + \phi_\beta - 2\phi_c) \rangle$;
- $N \approx N_+ \approx N_-$ is POI multiplicity; $N_{2\mathrm{p},3\mathrm{p}}$ is 2p (3p) nonflow pair (triplet, where all 3 particles are correlated) multiplicity;
- $\epsilon_2 \equiv C_{2\mathrm{p}} N_{2\mathrm{p}} v_{2,2\mathrm{p}} / (N v_2)$ is the 2p correlation w.r.t. the 2p cluster azimuth, coupled with 2p cluster elliptic flow ($v_{2,2\mathrm{p}}$);
- $\epsilon_3 \equiv C_{3\mathrm{p}} N_{3\mathrm{p}} / (2N)$ is the 3p correlation within the correlated triplet.

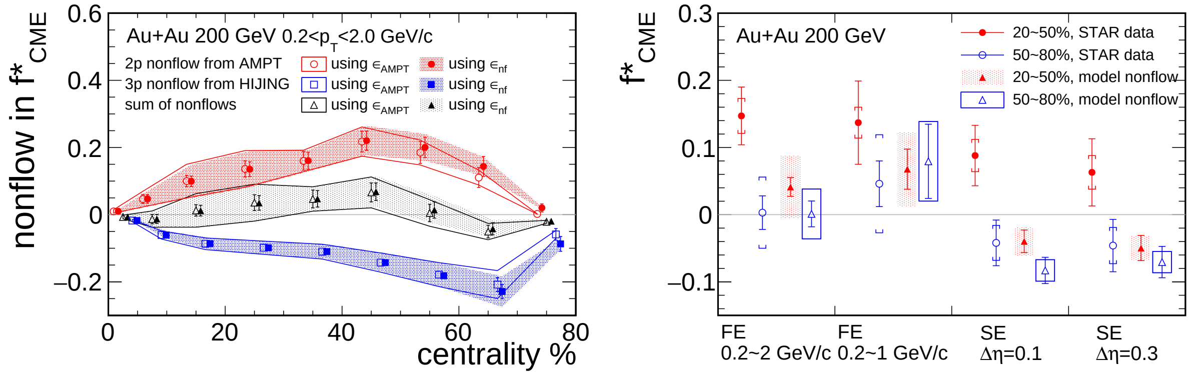

Figure 8.2. The nonflow backgrounds estimated from AMPT, HIJING simulations, and STAR data scaling [40]. The left plot shows the 2p, 3p, and total nonflow contributions as functions of centrality. The right plot shows the nonflow background estimates in the centrality range 20-50% compared with the STAR data [87].

The $\Delta\gamma^*$ w.r.t. event plane (EP) can be calculated from C_3 and v_2^*:

$$\Delta\gamma^* \equiv C_3/v_2^*, \tag{8.6}$$

where the asterisk means $\Delta\gamma^*$ contains nonflow. Then, the nonflow in $\Delta\gamma^*$ is

$$\frac{N\Delta\gamma^*}{v_2^*} = \frac{NC_3}{{v_2^*}^2} = \frac{\epsilon_2}{1+\epsilon_{\rm nf}} + \frac{\epsilon_3}{Nv_2^2(1+\epsilon_{\rm nf})} = \frac{\epsilon_2}{1+\epsilon_{\rm nf}}\left(1+\frac{\epsilon_3/\epsilon_2}{Nv_2^2}\right). \tag{8.7}$$

To estimate the various nonflow terms, we use AMPT (A Multiphase Transport) [92, 93], HIJING (Heavy Ion Jet Interaction Generator) [96, 97] model simulations, and STAR data scaling [102] for Au+Au collisions at $\sqrt{s_{\rm NN}}$ = 200 GeV [40]. The 2p nonflow can contribute to $v_2^*\{\rm PP\}$, $\Delta\gamma\{\rm SP\}$, and $\Delta\gamma^*\{\rm PP\}$, where the latter two are coupled with the true elliptic flow. (The asterisk means the variables contain the nonflow backgrounds. While there is no nonflow contribution to $\Delta\gamma\{\rm SP\}$, nonflow contamination to $\Delta\gamma^*\{\rm PP\}$ is through $v_2^*\{\rm PP\}$ which is divided in the three-particle correlator measurement.) The 3p nonflow can contribute to $\Delta\gamma^*\{\rm PP\}$. The AMPT is mainly affected by 2p nonflow, while the 3p nonflow contribution is only around 15% [83]. The three-particle correlator in HIJING is mainly affected by 3p nonflow, because HIJING does not have flow and the 2p nonflow contribution to $\Delta\gamma^*$ needs to be coupled with finite flow. Together with STAR data scaling, we use AMPT for 2p nonflow and HIJING for 3p nonflow contributions to estimate nonflow effect on $f_{\rm CME}$ as functions of centrality as well as on the average values of $f_{\rm CME}$ in the centrality range $20-50\%$ (cf. Fig. 8.2). We find 2p nonflow increases $f_{\rm CME}$ while 3p nonflow decreases $f_{\rm CME}$. Their net nonflow contribution to $f_{\rm CME}$ is positive (but still consistent with zero within errors) for the full-event method, and may be negative for subevent method. These results are currently model dependent, but they provide some semi-quantitative assessment of additional background contamination in the $f_{\rm CME}$ measurements [100, 101, 84]. I am continuing this study by employing data measurements as much as possible to arrive at a more rigorous estimate of nonflow effect on the $f_{\rm CME}$.

8.4 CME Search in Isobar Collisions–A Blind Analysis

Publications:

- **Yicheng Feng**, Yufu Lin, Jie Zhao and Fuqiang Wang, *Revisit the chiral magnetic effect expectation in isobaric collisions at the relativistic heavy ion collider*, Phys. Lett. B **820**, 136549 (2021) doi:10.1016/j.physletb.2021.136549 [arXiv:2103.10378 [nucl-ex]] [85].

- S. Choudhury, X. Dong, J. Drachenberg, J. Dunlop, S. Esumi, Y. Feng, E. Finch, Y. Hu, J. Jia and J. Lauret, *et al.* *Investigation of experimental observables in search of the chiral magnetic effect in heavy-ion collisions in the STAR experiment*, Chin. Phys. C **46**, no.4, 014101 (2022), doi:10.1088/1674-1137/ac2a1f, arXiv:2105.06044 [nucl-ex] [86]

- M. Abdallah *et al.* [STAR], *Search for the chiral magnetic effect with isobar collisions at $\sqrt{s_{NN}}$=200 GeV by the STAR Collaboration at the BNL Relativistic Heavy Ion Collider*, Phys. Rev. C **105**, no.1, 014901 (2022) doi:10.1103/PhysRevC.105.014901 [arXiv:2109.00131 [nucl-ex]] [87].

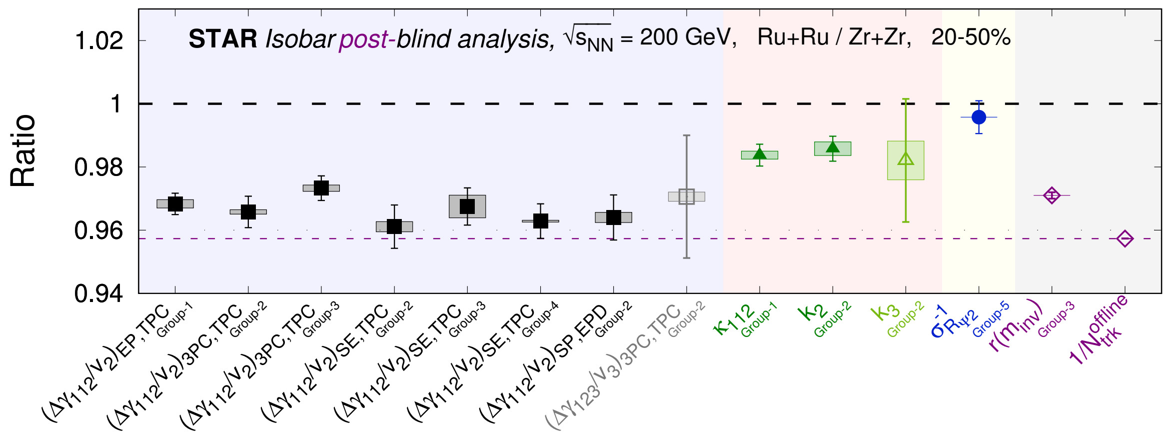

Figure 8.3. Isobar blind analysis results compilation, Fig. 27 of Ref. [87].

In 2018, STAR conducted the experiments of isobar collisions ($^{96}_{44}\mathrm{Ru}+^{96}_{44}\mathrm{Ru}$, $^{96}_{40}\mathrm{Zr}+^{96}_{40}\mathrm{Zr}$) at $\sqrt{s_{\mathrm{NN}}} = 200$ GeV [87]. Isobar means nucleus with the same nucleon number but different proton numbers, such as $^{96}_{44}\mathrm{Ru}$ and $^{96}_{40}\mathrm{Zr}$. It was initially anticipated that the same mass number would yield similar background contributions, whereas the different proton numbers (e.g., 10% between Ru and Zr) yield possibly distinguishable signal difference because the signal depends on the magnetic field created by the spectator protons. By comparing the observables from the isobar systems, possible CME signal may be extracted. This motivated the isobar collision program [103, 104, 105].

Many groups (BNL, Fudan, Huzhou, Purdue, SBU, Tsukuba, UCLA, UIC, WSU) in STAR Collaboration performed a blind analysis [87]. Myself, as a member of our Purdue HENP group, is one of the principal authors of this analysis. Each group focuses on a set of observables/methods in search for the CME. The isobar ratios of all the observables are shown in Fig. 8.3; they are all below or consistent with the naive unity baseline "1", which means no CME signal, as predefined in the blind analaysis, has been detected.

This result is not entirely unexpected. Our estimation [85] before the final blind analysis predicts only 2σ significance of isobar CME signal.

Additionally, the same mass number does not necessarily mean the same background. Ru and Zr differ in nuclei structure [98, 106, 107, 108, 109], which is enough to cause finite background difference. The current isobar results need further studies of the background baseline.

8.5 Improved Baseline of Isobar Collisions–Post Blind Analysis

Presentations:

- Yicheng Feng (for STAR Collaboration), *Study of nonflow baseline for the CME signal via two-particle $(\Delta\eta, \Delta\phi)$ correlations in isobar collisions at STAR*, XXIXth International Conference on Ultra-relativistic Nucleus-Nucleus Collisions, Quark Matter 2022, https://indico.cern.ch/event/895086/contributions/4721260/. [88]
- Yicheng Feng (for STAR Collaboration), *Estimate of a new baseline for the chiral magnetic effect in isobar collisions at RHIC*, The 20$^{\text{th}}$ International Conference on Strangeness in Quark Matter, https://indico.cern.ch/event/1037821/. [89]

From the isobar blind analysis [87] mentioned in Sec. 8.4, the Ru+Ru to Zr+Zr ratio of the CME-sensitive observable $\Delta\gamma$, normalized by elliptic anisotropy (v_2), is close to the inverse multiplicity (N) ratio. In other words, the ratio of the $N\Delta\gamma/v_2$ observable is close to the naive background baseline of unity (right axis of Fig. 8.6). However, nonflow correlations are expected to cause the baseline to deviate from unity.

To further understand the isobar results, we study nonflow effects using the same isobar data. Based on the nonflow study in Sec. 8.3, the isobar ratio of $N\Delta\gamma^*/v_2^*$ becomes:

$$\begin{aligned}\frac{(N\Delta\gamma^*/v_2^*)^{\mathrm{Ru}}}{(N\Delta\gamma^*/v_2^*)^{\mathrm{Zr}}} \equiv& \frac{(NC_3/v_2^{*2})^{\mathrm{Ru}}}{(NC_3/v_2^{*2})^{\mathrm{Zr}}} \approx \frac{\epsilon_2^{\mathrm{Ru}}}{\epsilon_2^{\mathrm{Zr}}} \cdot \frac{(1+\epsilon_{\mathrm{nf}})^{\mathrm{Zr}}}{(1+\epsilon_{\mathrm{nf}})^{\mathrm{Ru}}} \cdot \frac{[1+\epsilon_3/\epsilon_2/(Nv_2^2)]^{\mathrm{Ru}}}{[1+\epsilon_3/\epsilon_2/(Nv_2^2)]^{\mathrm{Zr}}} \\ \approx& 1+\frac{\Delta\epsilon_2}{\epsilon_2}-\frac{\Delta\epsilon_{\mathrm{nf}}}{1+\epsilon_{\mathrm{nf}}}+\frac{\epsilon_3/\epsilon_2/(Nv_2^2)}{1+\epsilon_3/\epsilon_2/(Nv_2^2)}\left(\frac{\Delta\epsilon_3}{\epsilon_3}-\frac{\Delta\epsilon_2}{\epsilon_2}-\frac{\Delta N}{N}-\frac{\Delta v_2^2}{v_2^2}\right),\end{aligned} \tag{8.8}$$

where $\Delta X = X^{\mathrm{Ru}} - X^{\mathrm{Zr}}$. The variables in the second line that are not of differences between the two isobar systems (i.e., without the Δ in front) are meant for Zr, but all quantities are

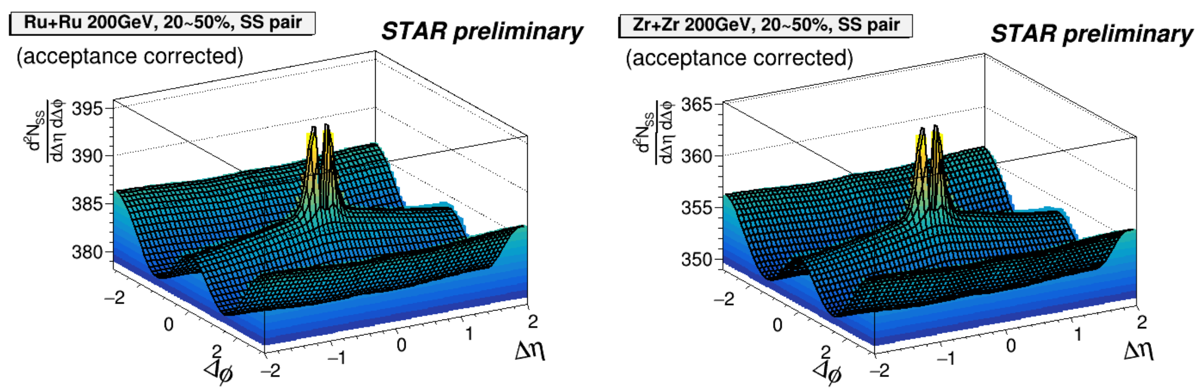

Figure 8.4. The two-particle $(\Delta\eta, \Delta\phi)$ distributions of SS pairs (left: Ru+Ru; right: Zr+Zr). The POI are from $0.2 < p_T < 2.0$ GeV/c, $|\eta| < 1$. The centrality range is $20 - 50\%$, which is defined by the POI multiplicity. The acceptance is corrected by mixed-event technique. The colors are the data histogram, and the black meshes are the fitting.

very similar between the two systems so we eliminated the superscript. We need $\epsilon_{\rm nf}$, ϵ_2, ϵ_3 for a new background estimate.

We fit the two-particle $(\Delta\eta, \Delta\phi)$ 2D same-sign (SS) pair distribution by a 2D function including different flow and nonflow components. By this means, we can estimate the "true" flow ($V_2 = v_2^2$) and nonflow (U) separately in $v_2^{*2} = \langle\cos(2\Delta\phi)\rangle$ measurement, and therefore calculate the nonflow fraction $\epsilon_{\rm nf} \equiv U/V_2$ [40]. For the STAR isobar data, we apply the cuts $0.2 < p_T < 2.0$ GeV/c, $|\eta| < 1$ for particles of interests (POI), and centrality $20\% \sim 50\%$ defined by POI distribution. The fitting function is

$$\begin{aligned} f(\Delta\eta, \Delta\phi) =& A_1 G_{\text{NS},W}(\Delta\eta) G_{\text{NS},W}(\Delta\phi) + A_2 G_{\text{NS},N}(\Delta\eta) G_{\text{NS},N}(\Delta\phi) + A_3 G_{\text{NS},D}(\Delta\eta) G_{\text{NS},D}(\Delta\phi) \\ &+ \frac{B}{2-|\Delta\eta|}\text{erf}\left(\frac{2-|\Delta\eta|}{\sqrt{2}\sigma_{\Delta\eta,\text{AS}}}\right) G_{\text{AS}}(\Delta\phi \pm \pi) + D G_{\text{RG}}(\Delta\eta) \\ &+ C\left[1 + 2V_1\cos(\Delta\phi) + 2V_2\cos(2\Delta\phi) + 2V_3\cos(3\Delta\phi)\right], \end{aligned} \tag{8.9}$$

where $G_s(x)$ is a Gaussian function with width $\sigma_{x,s}$, and $G_s(\Delta\phi + \mu)$ means $\Sigma_{n\in\mathbb{Z}} G_s(\Delta\phi + 2n\pi + \mu)$ to ensure periodicity. The subscripts mean NS–nearside, AS–awayside, RG–ridge; W–wide, N–narrow, D–dip. The complete fit results are listed in Table 8.1. If we assume

Table 8.1. The results of fits on the 2D $(\Delta\eta, \Delta\phi)$ distribution of SS pairs for STAR isobar data in Fig. 8.4.

STAR preliminary	Ru+Ru	Zr+Zr
A_1	2.96677 ± 0.00948	2.80128 ± 0.00742
$\sigma_{\Delta\eta,\mathrm{NS},W}$	0.98780 ± 0.00304	0.95502 ± 0.00251
$\sigma_{\Delta\phi,\mathrm{NS},W}$	0.63294 ± 0.00088	0.63643 ± 0.00080
A_2	15.61488 ± 0.01065	14.51507 ± 0.00909
$\sigma_{\Delta\eta,\mathrm{NS},N}$	0.12668 ± 0.00008	0.12839 ± 0.00008
$\sigma_{\Delta\phi,\mathrm{NS},N}$	0.12889 ± 0.00006	0.12977 ± 0.00006
A_3	-72.52241 ± 0.01842	-66.94299 ± 0.01592
$\sigma_{\Delta\eta,\mathrm{NS},D}$	0.02229 ± 0.00001	0.02231 ± 0.00001
$\sigma_{\Delta\phi,\mathrm{NS},D}$	0.10297 ± 0.00003	0.10262 ± 0.00003
B	0.21401 ± 0.00369	0.19428 ± 0.00305
$\sigma_{\Delta\eta,\mathrm{AS}}$	0.59135 ± 0.00529	0.58923 ± 0.00483
$\sigma_{\Delta\phi,\mathrm{AS}}$	$1.1 \times 10^5 \pm 18.3 \times 10^5$	$1.4 \times 10^5 \pm 11.7 \times 10^5$
D	0.27593 ± 0.00317	0.26596 ± 0.00259
$\sigma_{\Delta\eta,\mathrm{RG}}$	0.25998 ± 0.00176	0.25242 ± 0.00154
C	381.65092 ± 0.01080	351.98762 ± 0.00888
V_1	-0.001916 ± 0.000006	-0.001943 ± 0.000005
V_2	0.002972 ± 0.000003	0.002867 ± 0.000003
V_3	0.000177 ± 0.000001	0.000184 ± 0.000001
χ^2/NDF	$1018458.1/159982 = 6.4$	$1136361.1/159982 = 7.1$

Table 8.2. Some fit parameters and nonflow calculations. The asterisk means that the quantity (e.g., measured v_2^*) contains nonflow. The "inclusive" means all pairs including OS and SS.

STAR preliminary		Ru+Ru	Zr+Zr
SS	fit parameter C	381.651 ± 0.011	351.988 ± 0.009
	fit parameter $V_2 = v_2^2$	0.002972 ± 0.000003	0.002867 ± 0.000003
	$\langle\cos(2\Delta\phi)\rangle_{\mathrm{SS}}$ $(\lvert\Delta\eta\rvert > 0.05)$	0.0035968 ± 0.0000010	0.0034930 ± 0.0000010
inclusive	$\langle\cos(2\Delta\phi)\rangle = v_2^{*2}$ $(\lvert\Delta\eta\rvert > 0.05)$	0.0037161 ± 0.0000007	0.0036088 ± 0.0000007
	nonflow $U = \langle\cos(2\Delta\phi)\rangle - V_2$	0.000745 ± 0.000003	0.000742 ± 0.000003
	$\epsilon_{\mathrm{nf}} = U/V_2$	$(25.06 \pm 0.10)\%$	$(25.88 \pm 0.09)\%$

the "true" flow η-independent, then fitting parameters $V_n = v_n^2$ are the true flows, so we can get the flow and nonflow results in v_2^{*2} measurement. The results are listed in Table 8.2. If the nearside wide Gaussian (A_1 term) is counted into "true" flow, then $(v_2^2)^{\mathrm{Ru}} = 0.003489$, $(v_2^2)^{\mathrm{Zr}} = 0.003381$, $\epsilon_{\mathrm{nf}}^{\mathrm{Ru}} = 6.50\%$, $\epsilon_{\mathrm{nf}}^{\mathrm{Zr}} = 6.73\%$. We count half of this difference from the default as systematic uncertainty in the following quoted numbers: $\Delta\epsilon_{\mathrm{nf}} = (-0.82 \pm 0.13 \mp 0.30)\%$, $-\Delta\epsilon_{\mathrm{nf}}/(1+\epsilon_{\mathrm{nf}}) = (0.65 \pm 0.11 \pm 0.22)\%$, $\Delta v_2^2/v_2^2 = \Delta V_2/V_2 = (3.7 \pm 0.1 \mp 0.3)\%$.

The zero degree calorimeter (ZDC) measures the spectator neutrons, whose measurement can be a good estimate of the reaction plane (RP) without nonflow contamination. If we assume negligible CME, ϵ_2 can be obtained from ZDC measurement [87]: $\epsilon_2 = \frac{N\Delta\gamma\{\mathrm{ZDC}\}}{v_2\{\mathrm{ZDC}\}} \approx 0.57 \pm 0.04 \pm 0.02$ (here we have assumed the tracking efficiency $\sim 80\%$) and $\Delta\epsilon_2/\epsilon_2 \approx (2.3 \pm 9.2)\%$. While ϵ_2 is well determined from the ZDC measurement, the statistical precision of $\Delta\epsilon_2$ is too poor; for reference, AMPT simulation w.r.t. reaction plane gives $\Delta\epsilon_2/\epsilon_2 \approx (3.5 \pm 1.4)\%$. However, the pair multiplicity difference $r \equiv (N_{\mathrm{OS}} - N_{\mathrm{SS}})/N_{\mathrm{OS}}$ is relatively precisely measured [87]. Assuming $C_{\mathrm{2p}}^{\mathrm{Ru}} = C_{\mathrm{2p}}^{\mathrm{Zr}}$ (which is a good assumption as data indicates a difference only of the order of 0.1%), then $\epsilon_2 \propto Nr$, and $\Delta\epsilon_2/\epsilon_2 = \Delta r/r + \Delta N/N = (-2.95 \pm 0.08)\% + 4.4\% = (1.45 \pm 0.08)\%$.

The 3p nonflow background, ϵ_3, is relatively hard to measure, so for now we use HIJING model to estimate it. HIJING simulation (see Fig. 8.5) indicates $\epsilon_3 \approx (1.84 \pm 0.04)\%$, and $\Delta\epsilon_3/\epsilon_3 = (0.5 \pm 2.7)\%$ (from $\sim 8.6 \times 10^8$ events for each isobar). We assume 50% systematic uncertainty for ϵ_3 ($\pm 0.92\%$), and assume $\Delta\epsilon_3/\epsilon_3$ is presently dominated by statistics. HIJING without jet quenching gives $\epsilon_3 = (2.24 \pm 0.05)\%$, differing from the default by 22%, suggesting

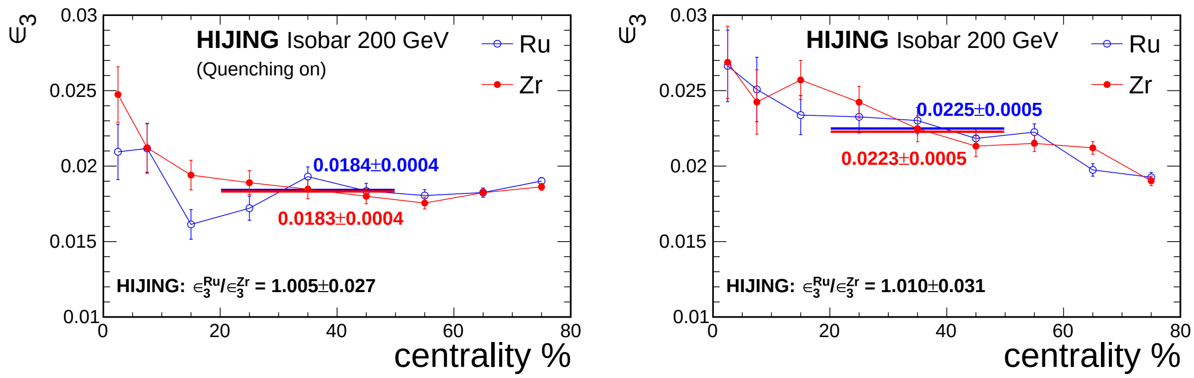

Figure 8.5. ϵ_3 estimate from HIJING simulations. The left plot has jet quenching on, and the right jet quenching off.

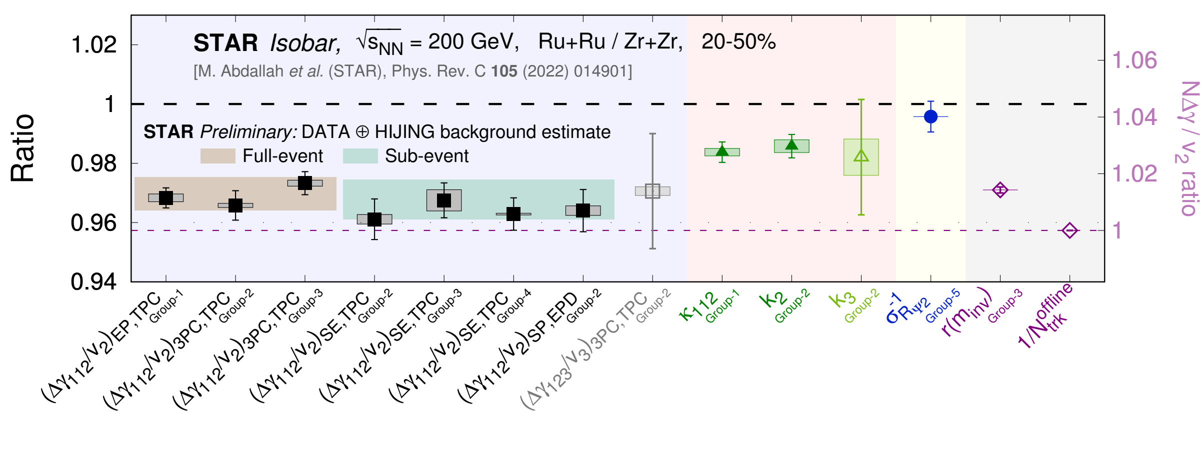

Figure 8.6. Isobar analysis results [87] with the new background estimates.

50% systematics a safe guesstimate. In future, we will try to find a data-driven way to better measure ϵ_3.

Table 8.3 summerizes all the quantities we have discussed above. We can calculate a new baseline of the isobar ratio $(N\Delta\gamma^*/v_2^*)^{\mathrm{Ru}}/(N\Delta\gamma^*/v_2^*)^{\mathrm{Zr}}$ by using the decomposition in Eq. 8.8:

$$\begin{aligned}\frac{(N\Delta\gamma^*/v_2^*)^{\mathrm{Ru}}}{(N\Delta\gamma^*/v_2^*)^{\mathrm{Zr}}} \approx& 1 + (1.45 \pm 0.08)\% + (0.65 \pm 0.11 \pm 0.22)\% \\ &+ (0.094 \pm 0.007 \pm 0.048)\Big[(0.5 \pm 2.7)\% - (1.45 \pm 0.08)\% \\ &- 4.4\% - (3.7 \pm 0.1 \pm 0.3)\%\Big] \\ =& 1+(1.45 \pm 0.08)\%+(0.65 \pm 0.11 \pm 0.22)\%-(0.85 \pm 0.26 \pm 0.44)\% \\ =& 1.013 \pm 0.003 \pm 0.005.\end{aligned} \tag{8.10}$$

If we use the subevent method with two subevents $-1 < \eta < -0.05$, $0.05 < \eta < 1$, then the number becomes $(1.011 \pm 0.005 \pm 0.005)$. Both numbers are plotted as the two bands in Fig. 8.6 for the new background baseline estimate.

Table 8.3. Quantities used for nonflow background estimate of the isobar ratio of Eq. 8.8 for STAR data.
† Except this column, all numbers quoted, including those in the text narrative, refer to those for full event. To obtain the sub-event estimate, we apply the two-particle acceptance of sub-events to the fitted nonflow of Eq. 8.9.

Quantity		Method	Systematic uncertainty	Full-event value	Sub-event value†
Multiplicity $\Delta N/N$	Measured		Negligible	4.4%	4.4%
Flow $\Delta v_2^2/v_2^2$	Measured	Nonflow subtracted as per below	From nonflow syst. uncertainty	$\Delta v_2^2/v_2^2 = (3.7 \pm 0.1 \pm 0.3)\%$	$\Delta v_2^2/v_2^2 = (3.7 \pm 0.1 \pm 0.3)\%$
v_2 nonflow	Measured	$(\Delta\eta, \Delta\phi)$ correlations, experimentally measured	Nonflow$\sim$ 25% (full event), dominated by NS wide Gaus; consider $\pm 1/2$ NS wide Gaus as syst. uncertainty	$-\Delta\epsilon_{\rm nf} = (0.82 \pm 0.13 \pm 0.30)\%$ $\frac{-\Delta\epsilon_{\rm nf}}{1+\epsilon_{\rm nf}} = (0.65 \pm 0.11 \pm 0.22)\%$	$-\Delta\epsilon_{\rm nf} = (0.59 \pm 0.15 \pm 0.27)\%$ $\frac{-\Delta\epsilon_{\rm nf}}{1+\epsilon_{\rm nf}} = (0.48 \pm 0.12 \pm 0.22)\%$
v_2-induced background: $\epsilon_2 = N\Delta\gamma/v_2$	Measured	Measured by ZDC (assume negligible CME)	Small	$\epsilon_2 = (0.57 \pm 0.04 \pm 0.02)\%$	$\epsilon_2 = (0.79 \pm 0.05 \pm 0.01)\%$
v_2-induced bkgd difference: $\frac{\Delta\epsilon_2}{\epsilon_2} \sim \frac{\Delta(N_{2\rm p}/N)}{(N_{2\rm p}/N)} = \frac{\Delta(rN)}{rN}$	Measured	$r = (N_{\rm OS} - N_{\rm SS})/N_{\rm OS}$ experimentally measured	Negligible	$\frac{\Delta\epsilon_2}{\epsilon_2} = (1.45 \pm 0.08)\%$	$\frac{\Delta\epsilon_2}{\epsilon_2} = (1.45 \pm 0.08)\%$
3p contribution to C_3: $\epsilon_3 = C_{3\rm p}N_{3\rm p}/(2N)$	Model estimate	HIJING simulations quenching-on	Quenching-on and off difference $\sim$ 20%. Take $\pm 50\%$ as syst. uncertainty	$\epsilon_3 = (1.84 \pm 0.04 \pm 0.92)\%$	$\epsilon_3 = (1.91 \pm 0.09 \pm 0.95)\%$
3p contribution difference: $\Delta\epsilon_3/\epsilon_3$	Model estimate	HIJING simulation quenching-on	Assumed negligible relative to the large stat. uncertainty	$\frac{\Delta\epsilon_3}{\epsilon_3} = (0.5 \pm 2.7)\%$ $\frac{\epsilon_3/\epsilon_2}{Nv_2^2} = 0.104 \pm 0.008 \pm 0.053$	$\frac{\Delta\epsilon_3}{\epsilon_3} = (-1.8 \pm 6.3)\%$ $\frac{\epsilon_3/\epsilon_2}{Nv_2^2} = 0.079 \pm 0.006 \pm 0.040$
Final background estimate				$1.013 \pm 0.003 \pm 0.005$	$1.011 \pm 0.005 \pm 0.005$

REFERENCES

1. Abelev, B. I. *et al.,* (STAR Collaboration). Global polarization measurement in Au+Au collisions. *Phys. Rev. C* **76,** 024915. https://link.aps.org/doi/10.1103/PhysRevC.76.024915 (2 Aug. 2007).

2. Adamczyk, L. *et al.,* (STAR Collaboration). Global Λ hyperon polarization in nuclear collisions: evidence for the most vortical fluid. *Nature* **548,** 62–65. arXiv: 1701.06657 [nucl-ex] (2017).

3. Du, F., Finch, L. E. & Sandweiss, J. Observing spontaneous strong CP violation through hyperon helicity correlations. *Phys. Rev. C* **78,** 044908 (2008).

4. Finch, L. E. & Murray, S. J. Investigating local parity violation in heavy-ion collisions using Λ helicity. *Phys. Rev. C* **96,** 044911. https://link.aps.org/doi/10.1103/PhysRevC.96.044911 (4 Oct. 2017).

5. Wikipedia. *Elementary particle* https://https://en.wikipedia.org/wiki/Elementary_particle.

6. Chatrchyan, S. *et al.,* (CMS Collaboration). Observation of a New Boson at a Mass of 125 GeV with the CMS Experiment at the LHC. *Phys. Lett. B* **716,** 30–61. arXiv: 1207.7235 [hep-ex] (2012).

7. Aad, G. *et al.,* (ATLAS Collaboration). Observation of a new particle in the search for the Standard Model Higgs boson with the ATLAS detector at the LHC. *Phys. Lett. B* **716,** 1–29. arXiv: 1207.7214 [hep-ex] (2012).

8. Han, M. Y. & Nambu, Y. Three Triplet Model with Double SU(3) Symmetry. *Phys. Rev.* **139** (ed Eguchi, T.) B1006–B1010 (1965).

9. Greensite, J. *An introduction to the confinement problem* https://link.springer.com/book/10.1007/978-3-642-14382-3 (2011).

10. Gross, D. J. & Wilczek, F. Ultraviolet Behavior of Nonabelian Gauge Theories. *Phys. Rev. Lett.* **30** (ed Taylor, J. C.) 1343–1346 (1973).

11. Politzer, H. D. Reliable Perturbative Results for Strong Interactions? *Phys. Rev. Lett.* **30** (ed Taylor, J. C.) 1346–1349 (1973).

12. Adler, S. L. Axial vector vertex in spinor electrodynamics. *Phys. Rev.* **177,** 2426–2438 (1969).

13. Bell, J. S. & Jackiw, R. A PCAC puzzle: $\pi 0 \to \gamma\gamma$ in the σ-model. *Il Nuovo Cimento A (1965-1970)* **60,** 47–61. ISSN: 1826-9869. https://doi.org/10.1007/BF02823296 (Mar. 1969).

14. Jackiw, R. W. Axial anomaly. *Scholarpedia* **3.** revision #136939, 7302 (2008).

15. Adams, J. *et al.,* (STAR Collaboration). Experimental and theoretical challenges in the search for the quark gluon plasma: The STAR Collaboration's critical assessment of the evidence from RHIC collisions. *Nucl. Phys. A* **757,** 102–183. arXiv: nucl-ex/0501009 (2005).

16. Adcox, K. *et al.,* (PHENIX Collaboration). Formation of dense partonic matter in relativistic nucleus-nucleus collisions at RHIC: Experimental evaluation by the PHENIX collaboration. *Nucl. Phys. A* **757,** 184–283. arXiv: nucl-ex/0410003 (2005).

17. Arsene, I. *et al.,* (BRAHMS Collaboration). Quark gluon plasma and color glass condensate at RHIC? The Perspective from the BRAHMS experiment. *Nucl. Phys. A* **757,** 1–27. arXiv: nucl-ex/0410020 (2005).

18. Back, B. B. *et al.,* (PHOBOS Collaboration). The PHOBOS perspective on discoveries at RHIC. *Nucl. Phys. A* **757,** 28–101. arXiv: nucl-ex/0410022 (2005).

19. Muller, B., Schukraft, J. & Wyslouch, B. First Results from Pb+Pb collisions at the LHC. *Ann. Rev. Nucl. Part. Sci.* **62,** 361–386. arXiv: 1202.3233 [hep-ex] (2012).

20. Armesto, N. & Scomparin, E. Heavy-ion collisions at the Large Hadron Collider: a review of the results from Run 1. *Eur. Phys. J. Plus* **131,** 52. arXiv: 1511.02151 [nucl-ex] (2016).

21. Kharzeev, D. E., McLerran, L. D. & Warringa, H. J. The Effects of topological charge change in heavy ion collisions: 'Event by event P and CP violation'. *Nucl.Phys.* **A803,** 227–253. arXiv: 0711.0950 [hep-ph] (2008).

22. Kharzeev, D. E. The Chiral Magnetic Effect and Anomaly-Induced Transport. *Prog. Part. Nucl. Phys.* **75,** 133–151. arXiv: 1312.3348 [hep-ph] (2014).

23. Voloshin, S. A. Parity violation in hot QCD: How to detect it. *Phys.Rev.* **C70,** 057901. arXiv: hep-ph/0406311 [hep-ph] (2004).

24. Abelev, B. *et al.,* (STAR Collaboration). Azimuthal Charged-Particle Correlations and Possible Local Strong Parity Violation. *Phys.Rev.Lett.* **103,** 251601. arXiv: 0909.1739 [nucl-ex] (2009).

25. Abelev, B. *et al.,* (STAR Collaboration). Observation of charge-dependent azimuthal correlations and possible local strong parity violation in heavy ion collisions. *Phys.Rev.* **C81,** 054908. arXiv: 0909.1717 [nucl-ex] (2010).

26. Adamczyk, L. *et al.,* (STAR Collaboration). Beam-energy dependence of charge separation along the magnetic field in Au+Au collisions at RHIC. *Phys. Rev. Lett.* **113,** 052302. arXiv: 1404.1433 [nucl-ex] (2014).

27. Adamczyk, L. *et al.,* (STAR Collaboration). Fluctuations of charge separation perpendicular to the event plane and local parity violation in $\sqrt{s_{NN}} = 200$ GeV Au+Au collisions at the BNL Relativistic Heavy Ion Collider. *Phys. Rev.* **C88,** 064911. arXiv: 1302.3802 [nucl-ex] (2013).

28. Adam, J. *et al.,* (STAR Collaboration). Charge-dependent pair correlations relative to a third particle in $p +$ Au and $d+$ Au collisions at RHIC. *Phys. Lett.* **B798,** 134975. arXiv: 1906.03373 [nucl-ex] (2019).

29. Abelev, B. *et al.,* (ALICE Collaboration). Charge separation relative to the reaction plane in Pb-Pb collisions at $\sqrt{s_{NN}} = 2.76$ TeV. *Phys.Rev.Lett.* **110,** 012301. arXiv: 1207.0900 [nucl-ex] (2013).

30. Adamczyk, L. *et al.,* (STAR Collaboration). Measurement of charge multiplicity asymmetry correlations in high-energy nucleus-nucleus collisions at $\sqrt{s_{NN}} = 200$ GeV. *Phys. Rev.* **C89,** 044908. arXiv: 1303.0901 [nucl-ex] (2014).

31. Khachatryan, V. *et al.,* (CMS Collaboration). Observation of charge-dependent azimuthal correlations in p-Pb collisions and its implication for the search for the chiral magnetic effect. *Phys. Rev. Lett.* **118,** 122301. arXiv: 1610.00263 [nucl-ex] (2017).

32. Sirunyan, A. M. *et al.,* (CMS Collaboration). Constraints on the chiral magnetic effect using charge-dependent azimuthal correlations in pPb and PbPb collisions at the CERN Large Hadron Collider. *Phys. Rev. C* **97,** 044912. arXiv: 1708.01602 [nucl-ex] (2018).

33. Acharya, S. *et al.,* (ALICE Collaboration). Constraining the magnitude of the Chiral Magnetic Effect with Event Shape Engineering in Pb-Pb collisions at $\sqrt{s_{\mathrm{NN}}} = 2.76$ TeV. *Phys. Lett.* **B777,** 151–162. arXiv: 1709.04723 [nucl-ex] (2018).

34. Acharya, S. *et al.,* (ALICE Collaboration). Constraining the Chiral Magnetic Effect with charge-dependent azimuthal correlations in Pb-Pb collisions at $\sqrt{s_{\mathrm{NN}}} = 2.76$ and 5.02 TeV. *JHEP* **09,** 160. arXiv: 2005.14640 [nucl-ex] (2020).

35. Wang, F. Effects of Cluster Particle Correlations on Local Parity Violation Observables. *Phys.Rev.* **C81,** 064902. arXiv: 0911.1482 [nucl-ex] (2010).

36. Bzdak, A., Koch, V. & Liao, J. Remarks on possible local parity violation in heavy ion collisions. *Phys.Rev.* **C81,** 031901. arXiv: 0912.5050 [nucl-th] (2010).

37. Schlichting, S. & Pratt, S. Charge conservation at energies available at the BNL Relativistic Heavy Ion Collider and contributions to local parity violation observables. *Phys.Rev.* **C83,** 014913. arXiv: 1009.4283 [nucl-th] (2011).

38. Wang, F. & Zhao, J. Challenges in flow background removal in search for the chiral magnetic effect. *Phys. Rev.* **C95,** 051901. arXiv: 1608.06610 [nucl-th] (2017).

39. Zhao, J. & Wang, F. Experimental searches for the chiral magnetic effect in heavy-ion collisions. *Prog. Part. Nucl. Phys.* **107,** 200–236. arXiv: 1906.11413 [nucl-ex] (2019).

40. Feng, Y., Zhao, J., Li, H., Xu, H.-j. & Wang, F. Two- and three-particle nonflow contributions to the chiral magnetic effect measurement by spectator and participant planes in relativistic heavy ion collisions. *Phys. Rev. C* **105,** 024913. arXiv: 2106.15595 [nucl-ex] (2022).

41. Schukraft, J., Timmins, A. & Voloshin, S. A. Ultra-relativistic nuclear collisions: event shape engineering. *Phys. Lett.* **B719,** 394–398. arXiv: 1208.4563 [nucl-ex] (2013).

42. Zhao, J., Li, H. & Wang, F. Isolating the chiral magnetic effect from backgrounds by pair invariant mass. *Eur. Phys. J. C* **79,** 168. arXiv: 1705.05410 [nucl-ex] (2019).

43. Adam, J. *et al.,* (STAR Collaboration). Pair invariant mass to isolate background in the search for the chiral magnetic effect in Au+Au collisions at $\sqrt{s_{\rm NN}}= 200$ GeV. arXiv: 2006.05035 [nucl-ex] (June 2020).

44. Xu, H.-j. *et al.* Varying the chiral magnetic effect relative to flow in a single nucleus-nucleus collision. *Chin. Phys. C* **42,** 084103. arXiv: 1710.07265 [nucl-th] (2018).

45. Zyla, P. A. *et al.,* (Particle Data Group). Review of Particle Physics. *PTEP* **2020,** 083C01 (2020).

46. Harrison, M., Ludlam, T. & Ozaki, S. RHIC project overview. *Nucl. Instrum. Meth. A* **499,** 235–244 (2003).

47. Harrison, M., Peggs, S. G. & Roser, T. The RHIC accelerator. *Ann. Rev. Nucl. Part. Sci.* **52,** 425–469 (2002).

48. Courant, E. D. Accelerators, colliders, and snakes. *Ann. Rev. Nucl. Part. Sci.* **53,** 1–37 (2003).

49. *STAR lite* https://www.star.bnl.gov/lite/.

50. Wieman, H. *et al.,* (STAR Collaboration). STAR TPC at RHIC. *IEEE Trans. Nucl. Sci.* **44** (eds Barsotti, E., Hoffman, E. J. & Kirsten, F. A.) 671–678 (1997).

51. Anderson, M. *et al.* The Star time projection chamber: A Unique tool for studying high multiplicity events at RHIC. *Nucl. Instrum. Meth. A* **499,** 659–678. arXiv: nucl-ex/0301015 (2003).

52. Shen, F. *et al.* MWPC prototyping and performance test for the STAR inner TPC upgrade. *Nucl. Instrum. Meth. A* **896,** 90–95. arXiv: 1805.03938 [physics.ins-det] (2018).

53. Adams, J. *et al.* The STAR Event Plane Detector. *Nucl. Instrum. Meth. A* **968,** 163970. arXiv: 1912.05243 [physics.ins-det] (2020).

54. Llope, W. J. *et al.* The TOFp / pVPD time-of-flight system for STAR. *Nucl. Instrum. Meth. A* **522,** 252–273. arXiv: nucl-ex/0308022 (2004).

55. *STAR data production streams picoDst summary and availability* https://www.star.bnl.gov/public/comp/prod/localdata/ProdDDstreams_pico.html.

56. *STAR Run18 Au+Au* $\sqrt{s_{NN}}$ = *27 GeV, P19ib production summary* https://www.star.bnl.gov/public/comp/prod/prodsum/27GeV_production_2018.P19ib.html.

57. Han, Y. & Ye, Z., (STAR Collaboration). *Centrality Definition for Run18 27 GeV AuAu MB Data* https://drupal.star.bnl.gov/STAR/system/files/CentralityDefinition_Run18_27GeV_ZaochenYe_20190930.pdf.

58. Adler, C. *et al.,* (STAR Collaboration). Midrapidity Lambda and anti-Lambda production in Au + Au collisions at $\sqrt{s_{NN}} = 130$ GeV. *Phys. Rev. Lett.* **89,** 092301. arXiv: nucl-ex/0203016 (2002).

59. Adams, J. R., (STAR Collaboration). Differential measurements of Λ polarization in Au+Au collisions and a search for the magnetic field by STAR. *Nucl. Phys. A* **1005** (eds Liu, F., Wang, E., Wang, X.-N., Xu, N. & Zhang, B.-W.) 121864 (2021).

60. Adams, J. *et al.,* (STAR Collaboration). *Differential measurements of* Λ *polarization in Au+Au collisions and a search for the magnetic field by STAR* https://indico.cern.ch/event/792436/contributions/3535689/. Quark Matter 2019 - the XXVIIIth International Conference on Ultra-relativistic Nucleus-Nucleus Collisions.

61. Kalman, R. E. A New Approach to Linear Filtering and Prediction Problems. *Journal of Basic Engineering* **82,** 35–45. ISSN: 0021-9223. eprint: https://asmedigitalcollection.asme.org/fluidsengineering/article-pdf/82/1/35/5518977/35_1.pdf. https://doi.org/10.1115/1.3662552 (Mar. 1960).

62. Stepanov, O. A. Kalman filtering: Past and present. An outlook from Russia. (On the occasion of the 80th birthday of Rudolf Emil Kalman). *Gyroscopy and Navigation* **2,** 99–110. ISSN: 2075-1109. https://doi.org/10.1134/S2075108711020076 (Apr. 2011).

63. Stratonovich, R. L. Optimum nonlinear systems which bring about a separation of a signal with constant parameters from noise. *Radiofizika* **2,** 892–901 (1959).

64. Stratonovich, R. L. in *Non-Linear Transformations of Stochastic Processes* 422–426 (Elsevier, 1965).

65. Stratonovich, R. L. Application of the Markov processes theory to optimal filtering. *Radio Engineering and Electronic Physics* **5,** 1–19 (1960).

66. Stratonovich, R. L. in *Non-linear transformations of stochastic processes* 427–453 (Elsevier, 1965).

67. Zyzak, M. *Online selection of short-lived particles on many-core computer architectures in the CBM experiment at FAIR* https://drupal.star.bnl.gov/STAR/system/files/KFParticleTutorial_11.12.2018.pdf. PhD thesis (2016), 165.

68. Gorbunov, S. *On-line reconstruction algorithms for the CBM and ALICE experiments* http://publikationen.ub.uni-frankfurt.de/frontdoor/index/index/docId/29538. PhD thesis (2013), 104, 9.

69. Wikipedia. *Markov chain* https://en.wikipedia.org/wiki/Markov_chain.

70. Zyzak, M., (TFG group). *KFParticle tutorial* https://drupal.star.bnl.gov/STAR/system/files/KFParticleTutorial_11.12.2018.pdf.

71. *STAR EPD* https://drupal.star.bnl.gov/STAR/blog/lisa/using-epd-event-plane-finder.

72. *STAR EPD* https://drupal.star.bnl.gov/STAR/blog/lisa/optimizing-ep1-resolution-au27au-ring-dependent-weights-eta-dependent-weights.

73. Poskanzer, A. M. & Voloshin, S. Methods for analyzing anisotropic flow in relativistic nuclear collisions. *Phys.Rev.* **C58,** 1671–1678. arXiv: nucl-ex/9805001 [nucl-ex] (1998).

74. Alber, T. *et al.,* (NA35 Collaboration). Charged particle production in proton, deuteron, oxygen and sulphur nucleus collisions at 200-GeV per nucleon. *Eur. Phys. J. C* **2,** 643–659. arXiv: hep-ex/9711001 (1998).

75. Appelshauser, H. *et al.,* (NA49 Collaboration). Baryon stopping and charged particle distributions in central Pb + Pb collisions at 158-GeV per nucleon. *Phys. Rev. Lett.* **82,** 2471–2475. arXiv: nucl-ex/9810014 (1999).

76. Busza, W. & Goldhaber, A. S. NUCLEAR STOPPING POWER. *Phys. Lett. B* **139,** 235 (1984).

77. Adams, J. *Lambda polarization at 3 GeV in Au+Au collisions at STAR* https://drupal.star.bnl.gov/STAR/system/files/Adams2020Feb12_LambdaPolarizationAt3GeV-BulkCorrOnlinePwg.pdf.

78. Upsal, I., (STAR Collaboration). *Global polarization of the* $\Lambda/\bar{\Lambda}$ *system in the STAR BES* https://drupal.star.bnl.gov/STAR/files/UpsalThesisV4.pdf.

79. Feng, Y., Zhao, J. & Wang, F. Responses of the chiral-magnetic-effect–sensitive sine observable to resonance backgrounds in heavy-ion collisions. *Phys. Rev. C* **98,** 034904. arXiv: 1803.02860 `[nucl-th]` (2018).

80. Feng, Y., Wang, F. & Zhao, J. Comment on "A sensitivity study of the primary correlators used to characterize chiral-magnetically-driven charge separation" by Magdy, Nie, Ma, and Lacey. arXiv: 2009.10057 `[nucl-ex]` (Sept. 2020).

81. Feng, Y., Zhao, J., Xu, H.-j. & Wang, F. Deciphering the $R\Psi_m$ correlator in search for the chiral magnetic effect in relativistic heavy ion collisions. *Phys. Rev. C* **103,** 034912. arXiv: 2011.01123 `[nucl-th]` (2021).

82. Feng, Y., Zhao, J. & Wang, F. Back-to-back relative-excess observable to identify the chiral magnetic effect. *Phys. Rev. C* **101,** 014915. arXiv: 1908.10210 `[nucl-th]` (2020).

83. Zhao, J., Feng, Y., Li, H. & Wang, F. HIJING can describe the anisotropy-scaled charge-dependent correlations at the BNL Relativistic Heavy Ion Collider. *Phys. Rev. C* **101,** 034912. arXiv: 1912.00299 `[nucl-th]` (2020).

84. Abdallah, M. *et al.,* (STAR Collaboration). Search for the Chiral Magnetic Effect via Charge-Dependent Azimuthal Correlations Relative to Spectator and Participant Planes in Au+Au Collisions at $\sqrt{s_{NN}} = 200\,\mathrm{GeV}$. *Phys. Rev. Lett.* **128,** 092301. arXiv: 2106.09243 `[nucl-ex]` (2022).

85. Feng, Y., Lin, Y., Zhao, J. & Wang, F. Revisit the chiral magnetic effect expectation in isobaric collisions at the relativistic heavy ion collider. *Phys. Lett. B* **820,** 136549. arXiv: 2103.10378 `[nucl-ex]` (2021).

86. Choudhury, S. *et al.* Investigation of experimental observables in search of the chiral magnetic effect in heavy-ion collisions in the STAR experiment. *Chin. Phys. C* **46,** 014101. arXiv: 2105.06044 [nucl-ex] (2022).

87. Abdallah, M. *et al.,* (STAR Collaboration). Search for the chiral magnetic effect with isobar collisions at $\sqrt{s_{NN}}$=200 GeV by the STAR Collaboration at the BNL Relativistic Heavy Ion Collider. *Phys. Rev. C* **105,** 014901. arXiv: 2109.00131 [nucl-ex] (2022).

88. Feng, Y., (STAR Collaboration). *Study of nonflow baseline for the CME signal via two-particle* $(\Delta\eta, \Delta\phi)$ *correlations in isobar collisions at STAR* https://indico.cern.ch/event/895086/contributions/4721260/. XXIXth International Conference on Ultra-relativistic Nucleus-Nucleus Collisions, Quark Matter 2022.

89. Feng, Y., (STAR Collaboration). *Estimate of a new baseline for the chiral magnetic effect in isobar collisions at RHIC* https://indico.cern.ch/event/1037821/. The 20$^{\text{th}}$ International Conference on Strangeness in Quark Matter.

90. Ajitanand, N. N., Lacey, R. A., Taranenko, A. & Alexander, J. M. A New method for the experimental study of topological effects in the quark-gluon plasma. *Phys. Rev. C* **83,** 011901. arXiv: 1009.5624 [nucl-ex] (2011).

91. Magdy, N., Shi, S., Liao, J., Ajitanand, N. & Lacey, R. A. New correlator to detect and characterize the chiral magnetic effect. *Phys. Rev. C* **97,** 061901. arXiv: 1710.01717 [physics.data-an] (2018).

92. Zhang, B., Ko, C., Li, B.-A. & Lin, Z.-W. A multiphase transport model for nuclear collisions at RHIC. *Phys.Rev.* **C61,** 067901. arXiv: nucl-th/9907017 [nucl-th] (2000).

93. Lin, Z.-W., Ko, C. M., Li, B.-A., Zhang, B. & Pal, S. A Multi-phase transport model for relativistic heavy ion collisions. *Phys.Rev.* **C72,** 064901. arXiv: nucl-th/0411110 [nucl-th] (2005).

94. Magdy, N., Nie, M.-W., Ma, G.-L. & Lacey, R. A. A sensitivity study of the primary correlators used to characterize chiral-magnetically-driven charge separation. *Phys. Lett. B* **809,** 135771. arXiv: 2002.07934 [nucl-ex] (2020).

95. Adam, J. *et al.,* (STAR Collaboration). Charge separation measurements in $p(d)$+Au and Au+Au collisions; implications for the chiral magnetic effect. arXiv: 2006.04251 [nucl-ex] (June 2020).

96. Wang, X.-N. & Gyulassy, M. HIJING: A Monte Carlo model for multiple jet production in p p, p A and A A collisions. *Phys.Rev.* **D44,** 3501–3516 (1991).

97. Gyulassy, M. & Wang, X.-N. HIJING 1.0: A Monte Carlo program for parton and particle production in high-energy hadronic and nuclear collisions. *Comput.Phys.Commun.* **83,** 307. arXiv: nucl-th/9502021 [nucl-th] (1994).

98. Xu, H.-j. *et al.* Importance of Isobar Density Distributions on the Chiral Magnetic Effect Search. *Phys. Rev. Lett.* **121,** 022301. https://link.aps.org/doi/10.1103/PhysRevLett.121.022301 (2 July 2018).

99. Wang, F. *CME–Experimental Results and Interpretation* https://indico.cern.ch/event/895086/contributions/4615143/. XXIXth International Conference on Ultra-relativistic Nucleus-Nucleus Collisions, Quark Matter 2022.

100. Zhao, J., (STAR Collaboration). Measurements of the chiral magnetic effect with background isolation in 200 GeV Au+Au collisions at STAR. *Nucl. Phys.* **A982,** 535–538. arXiv: 1807.09925 [nucl-ex] (2019).

101. Zhao, J., (STAR Collaboration). Search for CME in U+U and Au+Au collisions in STAR with different approaches of handling backgrounds. *Nucl. Phys. A* **1005** (eds Liu, F., Wang, E., Wang, X.-N., Xu, N. & Zhang, B.-W.) 121766. arXiv: 2002.09410 [nucl-ex] (2021).

102. Abdelwahab, N. M. *et al.,* (STAR Collaboration). Isolation of Flow and Nonflow Correlations by Two- and Four-Particle Cumulant Measurements of Azimuthal Harmonics in $\sqrt{s_{\rm NN}}$ = 200 GeV Au+Au Collisions. *Phys. Lett. B* **745,** 40–47. arXiv: 1409.2043 [nucl-ex] (2015).

103. Voloshin, S. A. Testing the Chiral Magnetic Effect with Central U+U collisions. *Phys. Rev. Lett.* **105,** 172301. arXiv: 1006.1020 [nucl-th] (2010).

104. Kharzeev, D. E., Liao, J., Voloshin, S. A. & Wang, G. Chiral magnetic and vortical effects in high-energy nuclear collisions—A status report. *Prog. Part. Nucl. Phys.* **88,** 1–28. arXiv: 1511.04050 [hep-ph] (2016).

105. Koch, V. *et al.* Status of the chiral magnetic effect and collisions of isobars. *Chin. Phys. C* **41,** 072001. arXiv: 1608.00982 [nucl-th] (2017).

106. Li, H. *et al.* Probing the neutron skin with ultrarelativistic isobaric collisions. *Phys. Rev. Lett.* **125,** 222301. arXiv: 1910.06170 [nucl-th] (2020).

107. Xu, H.-j., Li, H., Wang, X., Shen, C. & Wang, F. Determine the neutron skin type by relativistic isobaric collisions. *Phys. Lett. B* **819,** 136453. arXiv: 2103.05595 [nucl-th] (2021).

108. Xu, H.-j. *et al.* Measuring neutron skin by grazing isobaric collisions. *Phys. Rev. C* **105,** L011901. arXiv: 2105.04052 [nucl-th] (2022).

109. Xu, H.-j. *et al.* Probing nuclear structure with mean transverse momentum in relativistic isobar collisions. arXiv: 2111.14812 [nucl-th] (Nov. 2021).

VITA

BASIC INFORMATION

Name: Yicheng Feng

Address: 2450 Sycamore Lane, West Lafayette, IN 47906

Phone: 765-775-8942

Email: feng216@purdue.edu, fengyich@outlook.com

EDUCATION

Purdue University *August 2017 - May 2022*

Location: 610 Purdue Mall, West Lafayette, IN, 47907, United States

Department: Department of Physics and Astronomy

Degree: PhD degree in Physics, May 2022

University of Science and Technology of China *August 2013 - August 2017*

Location: 96 Jinzhai Road, Hefei City, Anhui Province, 230027, China

Department: Physics Department

Degree: Bachelor of Science, May 2017

EXPERIENCE

Purdue University *January 2019 - May 2022*

Position Title: Research Assistant

Supervisor: Prof. Fuqiang Wang

STAR Collaboration *December 7, 2021 - December 21, 2021*

Location: Brookhaven National Laboratory

Position Title: STAR Shift Leader

Description: Taking STAR shifts

STAR Collaboration *December 10, 2019 - December 31, 2019*

Position Title: STAR Detector Operator

STAR Collaboration *May 13, 2019 - May 27, 2019*

Position Title: STAR Detector Operator

Purdue University *August 2017 - January 2019*

Position Title: Teaching Assistant

STAR Collaboration *May 12, 2018 - May 30, 2018*

Position Title: STAR Detector Operator

RESEARCH INTEREST

High Energy Nuclear Physics

I am interested in the high energy nuclear physics, and working on the data analysis from the STAR (Soleniod Tracker At Relativistic Heavy Ion Collider) experiment in Brookhaven National Lab.

The specific topic for me is to search for the Chiral Magnetic Effect (CME) in STAR experiment, which could be the evidence for the $\mathcal{P}/\mathcal{CP}$-violation in strong interaction.

PRESENTATION

[talk] The $20^{\mathbf{th}}$ International Conference on Strangeness in Quark Matter *June, 2022*

Title: Estimate of a new baseline for the chiral magnetic effect in isobar collisions at RHIC

Link: https://indico.cern.ch/event/1037821/

[poster] XXIXth International Conference on Ultra-relativistic Nucleus-Nucleus Collisions, Quark Matter 2022 *April, 2022*

Title: Study of nonflow baseline for the CME signal via two-particle $(\Delta\eta, \Delta\phi)$ correlations in isobar collisions at STAR

Link: https://indico.cern.ch/event/895086/contributions/4721260/

[talk] 2020 Fall Meeting of the APS Division of Nuclear Physics *October, 2020*

Title: Event-by-event correlations between $\Lambda/\bar{\Lambda}$ polarization and CME observables in Au+Au collisions at $\sqrt{s_{NN}} = 27$ GeV from STAR

Link: http://meetings.aps.org/Meeting/DNP20/Session/RB.3

[talk] APS April Meeting 2018 *April, 2018*

Title: Response studies of the CME-sensitive sine observable to heavy ion backgrounds

Link: http://meetings.aps.org/Meeting/APR18/Session/C12.2

AWARD

George W. Tautfest Award *March, 2021*

From: Department of Physics and Astronomy, Purdue University

Bilsland Dissertation Fellowship *March, 2021*

From: Department of Physics and Astronomy, Purdue University

Rolf Scharenberg Graduate Research Fellowship *August, 2018*

From: Department of Physics and Astronomy, Purdue University

USTC Undergraduate Student Honorary Rank of top 5% *December, 2016*

From: University of Science and Technology of China (USTC)

PUBLICATIONS

Few-author papers

1. **Y. Feng**, J. Zhao, H. Li, H. j. Xu and F. Wang, *Two- and three-particle nonflow contributions to the chiral magnetic effect measurement by spectator and participant planes in relativistic heavy ion collisions*, Phys. Rev. C **105**, no.2, 024913 (2022), doi:10.1103/PhysRevC.105.024913, arXiv:2106.15595 [nucl-ex]

2. **Yicheng Feng**, Jie Zhao, Hao-jie Xu, and Fuqiang Wang, *Decipher the R_{Ψ_m} correlator in search for the chiral magnetic effect in relativistic heavy ion collisions*, Phys. Rev. C **103**, 034912 (2021), doi:10.1103/PhysRevC.103.034912, arXiv:2011.01123 [nucl-th].

3. **Yicheng Feng**, Yufu Lin, Jie Zhao and Fuqiang Wang, *Revisit the chiral magnetic effect expectation in isobaric collisions at the relativistic heavy ion collider*, Phys. Lett. B **820**, 136549 (2021), doi:10.1016/j.physletb.2021.136549, arXiv:2103.10378 [nucl-ex].

4. S. Choudhury, X. Dong, J. Drachenberg, J. Dunlop, S. Esumi, Y. Feng, E. Finch, Y. Hu, J. Jia and J. Lauret, *et al. Investigation of experimental observables in search of the chiral magnetic effect in heavy-ion collisions in the STAR experiment*, Chin. Phys. C **46**, no.4, 014101 (2022), doi:10.1088/1674-1137/ac2a1f, arXiv:2105.06044 [nucl-ex].

5. Hao-jie Xu, Jie Zhao, **Yicheng Feng**, and Fuqiang Wang, *Importance of non-flow background on the chiral magnetic wave search*, Nucl. Phys. A **1005**, 121770 (2021), doi:10.1016/j.nuclphysa.2020.121770, arXiv:2002.05220 [nucl-th].

6. **Yicheng Feng**, Fuqiang Wang, and Jie Zhao, *Comment on "A sensitivity study of the primary correlators used to characterize chiral-magnetically-driven charge separation" by Magdy, Nie, Ma, and Lacey*, arXiv:2009.10057 [nucl-ex] (2020).

7. Jie Zhao, **Yicheng Feng**, Hanlin Li and Fuqiang Wang, *HIJING can describe the anisotropy-scaled charge-dependent correlations at the BNL Relativistic Heavy Ion Collider*, Phys. Rev. C **101**, 034912 (2020), doi:10.1103/PhysRevC.101.034912, arXiv:1912.00299 [nucl-th].

8. **Yicheng Feng**, Jie Zhao, and Fuqiang Wang, *Back-to-back relative-excess observable to identify the chiral magnetic effect*, Phys. Rev. C **101**, 014915 (2020), doi:10.1103/PhysRevC.101.014915,
arXiv:1908.10210 [nucl-th].

9. Hao-jie Xu, Jie Zhao, **Yicheng Feng**, and Fuqiang Wang, *Complications in the interpretation of the charge asymmetry dependent π flow for the chiral magnetic wave*, Phys. Rev. C **101**, 014913 (2020), doi:10.1103/PhysRevC.101.014913, arXiv:1910.02896 [nucl-th].

10. **Yicheng Feng**, Jie Zhao, and Fuqiang Wang, *Responses of the chiral-magnetic-effect–sensitive sine observable to resonance backgrounds in heavy-ion collisions*, Phys. Rev. C **98**, 034904 (2018), doi:10.1103/PhysRevC.98.034904, arXiv:1803.02860 [nucl-th].

STAR collaboration papers as one of the principal authors

1. M. Abdallah *et al.* [STAR], *Search for the chiral magnetic effect with isobar collisions at $\sqrt{s_{NN}}$=200 GeV by the STAR Collaboration at the BNL Relativistic Heavy Ion Collider*, Phys. Rev. C **105**, no.1, 014901 (2022), doi:10.1103/PhysRevC.105.014901, arXiv:2109.00131 [nucl-ex].

2. M. Abdallah *et al.* [STAR], *"Search for the Chiral Magnetic Effect via Charge-Dependent Azimuthal Correlations Relative to Spectator and Participant Planes in Au+Au Collisions at $\sqrt{s_{NN}}$ = 200 GeV,"* Phys. Rev. Lett. **128**, no.9, 092301 (2022), doi:10.1103/PhysRevLett.128.092301, arXiv:2106.09243 [nucl-ex].